Title
Correlation of electrical defects and device performance for wide bandgap metal-oxide semiconductors

Author
Park, Jin hee

Publication Date
2017

UNIVERSITY OF CALIFORNIA

Los Angeles

Correlation of electrical defects and device performance for wide bandgap metal-oxide semiconductors

A dissertation submitted in partial satisfaction of the
requirements for the degree Doctor of Philosophy
in Materials Science and Engineering

by

Jin Hee Park

2017

ABSTRACT OF THE DISSERTATION

Correlation of electrical defects and device performance for wide bandgap metal-oxide semiconductors

by

Jin Hee Park
Doctor of Philosophy in Materials Science and Engineering
University of California, Los Angeles, 2017
Professor Dwight Christopher Streit, Chair

In this dissertation, the effects of electrical defect states on the device performance and stability were examined and characterized for wide bandgap metal-oxide semiconductors. While previous research on metal-oxides in electronic device has mostly focused on the effect of light and/or bias stress on the device performance and stability, research presented here demonstrates and focuses on how electrical defect states within bandgap or at the interfacial layer between the channel and dielectric layer can affect the device performance and stability under light or/and bias stress. These results can help improvements to material sputtering growth which in turn can help improve overall device performance.

The first part of the dissertation characterizes the shallow-level defect state distribution under the conduction band minimum in Pd/ZnO Schottky barrier diode by a deep level transient spectroscopy. The second part details the deep-level defect states in sputtered ZnO thin-film transistors as a function of oxygen ratio during sputtering growth. Photo-induced threshold voltage-shift measurements under monochromatic illumination were used to characterize the deep-level defect distribution. As a result, the deep-level defect states of ZnO films were formed at the range of 1.8 – 2.1 eV below the conduction band minimum and were gradually decreased with increasing oxygen ratios.

The last part examines and characterizes sputtered a-ITZO TFTs under light and/or bias stress as a function of oxygen ratios. We confirmed that the photo stability and persistent photocurrent in a-IZTO TFTs were improved due to the reduced concentration of deep-level defects associated with oxygen vacancies at high oxygen ratios during sputtering growth. However, the device stability significantly degraded under bias stress with or without light at high oxygen ratios due to increased defect states at the interfacial layer between the channel and dielectric layer. The increased interfacial defects were characterized by XRR measurements and a hysteresis curve for various oxygen ratios. We have shown that good photo-bias device stability of sputtered a-ITZO TFTs can have a strong trade-off relation between photo and bias stress depending on oxygen ratios during growth by sputtering. In order to take advantage of the improved ITZO material growth at a high oxygen ratio, the interface-related problems must be solved.

The dissertation of Jin Hee Park is approved.

Mark S. Goorsky

Kuo-Nan Liou

Dwight Christopher Streit, Committee Chair

University of California, Los Angeles

2017

To my parents,

my wife, Yoon hee Lee and

my daughters, Soyeon, Jiyeon, Sequoia Dayeon Park and

my brother, Sehee Park

Table of Contents

List of Figures

List of Tables

Acknowledgements

I would like to thank my advisor, Professor Dwight C. Streit, for his support and mentorship over the past 6 years. Materials engineering and electronic device were quite foreign to me when I came to University of California, Los Angeles, but with his continuous guidance and support I have developed my own passion for this field. I would not have made it this far without his help. I would also like to thank my dissertation committee: Prof. Mark S. Goorsky, Prof. Qibing Pei, and Prof. Kuo-Nan Liou. Thank you for your time and assistance in evaluating my dissertation. I gratefully acknowledge financial support from the UCLA School of Engineering and Samsung. I want to acknowledge the use of the Nanoelectronics Research Facility (NRF) and Integrated Systems Nanofabrication Cleanroom (ISNC) at the California NanoSystems Institute (CNSI) in UCLA for making the fabrication of this device possible. I was very fortunate to have this opportunity to work and study in UCLA.

Through Prof. Streit I have had the chance to collaborate with other members at UCLA. I would like to thank my collaborators at the Diana lab who helped make this research possible, especially: Dr. Pradeep Senanayake, Dr. Ramesh B. Laghumavarapu, Dr. Wook-Jae Lee, and Alan Farrell. None of these researches would have been possible without their lab support of Prof. Diana L. Huffaker. I thank them for allowing me to use their low temperature chamber and monochromator. Although the ultimate goal was always independence, I have found that the most important part of learning has been the support of others. Many spectacular people can be found around us at almost any time, and they deserve all of the credit that I can offer. Everyone who worked alongside me made all of this possible.

I thank my lab mates in the Streit Lab, especially: Dr. Jiechen Wu, and Dr. Shenglin Ye. Dr. Jiechen Wu introduced me about electronic device processes to make a simple device, such as thin-film transistors. Dr. Shenglin Ye taught me about how to use the X-ray photoelectron spectroscopy (XPS) to measure the electronic state of metal oxides and I learn much from their great examples. Special thanks to Chao Li in Prof. Goorsky lab for his X-ray reflectivity (XRR) measurements. I would also like to thank Dr. Ignacio Martini, Dr. Sergey Prikhodko, Tony Wright, and Hoc Ngo for their help during my time at UCLA.

I would like to thank my Family and Friends for being there for me during the course of my graduate studies, especially Yoon hee Lee, Dr. You Seung Rim, Dr. Choong-Heui Chung, and Dr. Hyung-Seok Kim. My wife, Yoon hee Lee, devoted herself to my family. Dr. Choong-Heui Chung, and Dr. Hyung-Seok Kim helped me a lot for the preliminary exam during the first year at UCLA. Dr. You Seung Rim continually advised me on research. My growth as a researcher is due to the technical discussion and guidance by Dr. Rim. I cannot thank him enough for doing all this while working hard on completing my Ph.D. At last, I thank my parents for always believing in me.

Vita

1996-2001	*B.S. in Mechanical Engineering* Andong National University, Andong, Republic of Korea
2002-2004	*M.S. in Mechanical Engineering* Louisiana State University, Baton Rouge, USA
2004-2011	*Senior Engineer*, Advanced Optics Development Team SAMSUNG, Asan, Republic of Korea
Since 2011	*Graduate Student Researcher, in Materials Science and Engineering* University of California Los Angeles, Los Angeles, USA

Publications

1. Jinhee Park, You Seung Rim, Pradeep Senanayake, and Dwight Streit, “Observation of the electrical defect states distribution in ZnO Schottky diodes”, manuscript is being prepared, to be submitted soon
2. Jinhee Park, You Seung Rim, Chao Li, Jiechen Wu, Mark Goorsky, and Dwight Streit, “Defect-induced instability mechanisms of sputtered a-ITZO thin-film transistors”, submitted to the *Journal of Applied Physics*, 2017, under review
3. Jinhee Park*, You Seung Rim*, Chao Li, Hyung-Seok Kim, Mark Goorsky, Dwight Streit, “Deep-level defect distribution as a function of oxygen partial pressure in sputtered ZnO thin-film transistors”, *Current Applied Physics*, 2016, 16 (10), 1369-1373 (*Equal contribution)
4. Jiechen Wu, Xiaoxing Lu, Shenglin Ye, Jinhee Park and Dwight Streit, “Electrical

Characterization and Reliability Analysis of Al_2O_3/AlGaN/GaN MISH structure", *IEEE International Reliability Physics Symposium*, 2014, CD. 6.1-CD. 6.5

5. M.A. Wahab, J.H. Park, M.S. Alam, S.S. Pang, "Effect of corrosion prevention compounds on fatigue life in 2024-T3 aluminum alloy", *Journal of Materials Processing Technology,* 2006, 174 (1), 211-217
6. M.A. Wahab, G.R. Rohrsheim, J.H. Park, "Experimental study on the influence of overload induced residual stress field on fatigue crack growth in aluminium alloy", *Journal of Materials Processing Technology*, 2004, 153, 945-951

Chapter 1. Introduction

1.1 History of Metal Oxide-based Semiconductors

The hydrogenated amorphous silicon (a-Si:H) has been widely used in large-area electronics, especially for the driving switch thin-film transistors (TFTs) used in display back plane. These days, a high resolution, and high frame rate are required for next generation displays. For example, the charging time is about 7 μs for display with a resolution of 1920×1080, and frame rate of 120 Hz. [1] Nevertheless, a much smaller time of 1.2 μs is needed to drive the same-sized panel with a resolution of 3840×2160, and frame rate of 240 Hz. Therefore, the speed of TFTs needs to be increased practically from ~0.5 cm^2 V^{-1} s^{-1} to >5 cm^2 V^{-1} s^{-1}. However, the critical obstacles to realize a-Si:H for future high-end applications are low mobility (~0.5–1.0 cm^2 V^{-1} s^{-1}), optical opacity and mechanical flexibility. It is difficult to use a-Si TFTs as a backplane for active-matrix organic light-emitting-diode (AMOLED) displays.

To overcome these limitations, researchers have begun to study the use of metal oxides (MOs), which have relatively high carrier mobility (1.0–100 cm^2 V^{-1} s^{-1}) even in the amorphous state, high optical transparency due to its wide bandgap of 3.3 eV, some extra tolerance in mechanical flexibility, and ease of processing even at room temperature. [2-4] In addition, ZnO is thermally and chemically stable during wet processing compared to nitride semiconductors. Therefore, metal oxide-based materials have been extensively used in various applications, such as sensors, flexible TFTs on plastic substrates, and ultraviolet light-emitting diodes (LED). [5, 6] In late 2004 [7], Hosono Group at Tokyo Institute of technology reported that an amorphous oxide semiconductor (AOS) with the composition amorphous-$InGaZnO_4$ (a-IGZO) could be applied in the fabrication of flexible, transparent TFTs. They have much improved performance compared to conventional a-Si TFTs. They can be deposited as a uniform amorphous phase while retaining the high carrier mobility. It seems like that the reason is due to the large metal ns-orbital. So, their carrier path is independent of direction. Also, large area deposition is possible even at room temperature by sputtering. IGZO TFTs have been already commercialized in organic light-emitting-diode (OLED) displays. The summary of a-Si vs. metal oxide TFTs are shown in Table 1.1.

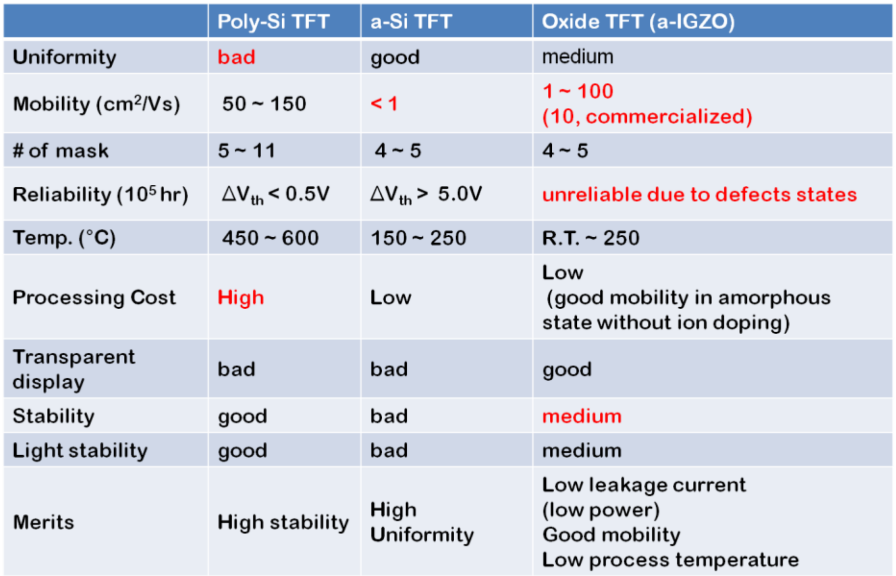

	Poly-Si TFT	a-Si TFT	Oxide TFT (a-IGZO)
Uniformity	bad	good	medium
Mobility (cm^2/Vs)	50 ~ 150	< 1	1 ~ 100 (10, commercialized)
# of mask	5 ~ 11	4 ~ 5	4 ~ 5
Reliability (10^5 hr)	$\Delta V_{th} < 0.5V$	$\Delta V_{th} > 5.0V$	unreliable due to defects states
Temp. (°C)	450 ~ 600	150 ~ 250	R.T. ~ 250
Processing Cost	High	Low	Low (good mobility in amorphous state without ion doping)
Transparent display	bad	bad	good
Stability	good	bad	medium
Light stability	good	bad	medium
Merits	High stability	High Uniformity	Low leakage current (low power) Good mobility Low process temperature

Table 1.1. A comparison of common TFTs technologies

In fact, back in 1964, first MOs TFTs were reported with an evaporated SnO_2 semiconductor on glass, with aluminum source-drain and Al_2O_3 gate dielectric. [8] MO TFTs based on polycrystalline oxide materials such as zinc oxide (ZnO) [9], indium oxide (In_2O_3) [10], and tin oxide (SnO_2) [11] were previously reported, but good performing metal oxide TFTs started to appear by Hoffman et al. [12], and Carcia et al. [13], in 2003 with the ZnO

TFTs. The work from Hoffman et al. reported transparent TFT devices with carrier mobility of 2.5 $cm^2\ V^{-1}\ s^{-1}$, and optical transmission of ~75 % in the visible range. In this work, a 220 nm thick aluminum-titanium oxide (ATO) by atomic layer deposition (ALD) was used as a gate insulator, ion beam sputtered indium-tin oxide (ITO) was used as a source/drain electrode, and finally ZnO channel layer was deposited by ion beam sputtering in 10^{-4} Torr of Ar/O_2 (80 % : 20 %); the substrate is unheated during deposition. However, the post-processing temperatures for obtaining good devices are too high, about 600℃.

While most researchers were working on binary oxides, such as SnO_2, ZnO, and In_2O_3, Nomura et al. reported transparent and flexible TFTs with a pulsed laser deposition (PLD) deposited a-IGZO, just using near-room temperature processing in 2004 [7]. They achieved the saturation mobility of 8.3 $cm^2\ V^{-1}\ s^{-1}$, threshold voltage of 1.6 V, and on/off current ratio of 10^3, which is comparable to the performance of a-Si:H TFTs, mostly in terms of carrier mobility. From this work, they showed the potential of metal oxide semiconductor (multi-component oxides) for active-matrix display switching TFT applications. Their work has attracted worldwide attention to this amorphous multi-component metal oxide TFTs as channel layers in high-end liquid-crystal-display (LCD) and AMOLED technology.

These days combinations of several cations have been used for this technology, such as indium-zinc oxide (IZO) [14, 15], amorphous-indium-gallium-zinc oxide (a-IGZO) [16-19], and amorphous-indium-zinc-tin oxide (a-IZTO) [20-24]. It has became common to obtain outstanding electrical properties, superior to a-Si:H, such as mobilities above 10 $cm^2\ V^{-1}\ s^{-1}$, on/off ratio of 10^6 and subthreshold swing of 0.2 V dec^{-1}. The origin for the high mobility is attributed to the unique carrier transport path in AOS, which is mainly composed of spatially overlapping metal *ns* orbital. [7] This spherical symmetry of ns orbital is insensitive to the directional order. This carrier transport properties are in contrast to silicon semiconductors, in which the carrier mobility decreases substantially when it is in amorphous state. Based on this information, metal oxide semiconductors could provide an effective alternative method for the future switching TFTs in displays, which will allow for transparency, low cost, low temperature processing, and high performance devices. The schematic history of metal oxide TFTs with conventional TFTs are shown in Figure 1.1.

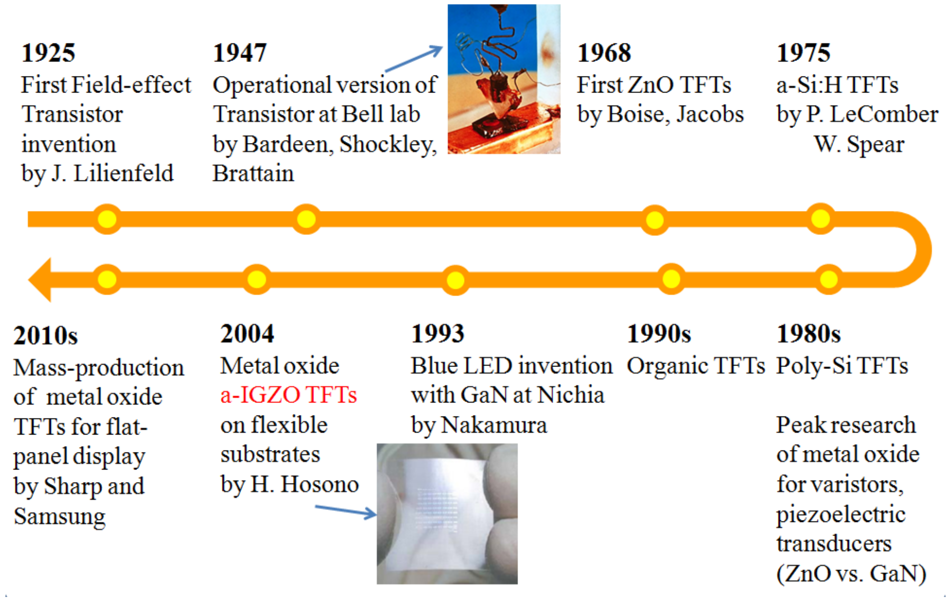

Figure 1.1. Main landmarks achieved with field effect transistors.

1.2 Motivation of Research

The main disadvantage of metal oxide semiconductor (for example, ZnO-based material) is the native intrinsic defects (e.g., oxygen vacancy (V_o), Zn interstitial (Zn_i) or Zn vacancy (V_{Zn})) that present in the material itself. [5, 25, 26] Since, they could extensively affect the electrical and optical properties of ZnO or the performance of the ZnO-related electronic devices. One of the most dominant defect states in ZnO is known as oxygen vacancy due to the low formation energy of 3.5 eV. [27] In addition, oxygen vacancies in ZnO-based material create problems, including persistent photoconductivity (PPC), and illumination stress instability for electronic devices, especially in switching TFTs. [28-30] It is also known that the existence of defects at the interface (especially at the channel/dielectric in TFTs) limits the device's static and dynamic performance and stability, for example threshold voltage (V_{th}). [3, 4, 31]

The photo-reliability of oxide TFTs is mostly deteriorated by negative rather than by positive bias stress, which is called the negative bias illumination stress (NBIS). [32-34] Several degradation models have been also proposed, including the carrier trapping model, the creation of ionized oxygen vacancies under bias stress, illumination, or NBIS conditions. [35-37] Due to both the high density of weak bonding and the under-coordinated atoms in amorphous state, the density of state (DOS) of subgap states in amorphous metal oxide is high. The schematic subgap defect states in a-IGZO are shown in Figure 1.2. [38] Due to the high DOS of subgap states and of subgap traps defects, the reliability of IGZO TFTs under positive bias stress (PBS) and especially negative bias and illumination stress (NBIS) remain critical issues. Therefore, characterization of electrical defect states in metal oxide TFTs is an essential part for fully understanding the device performance and stability.

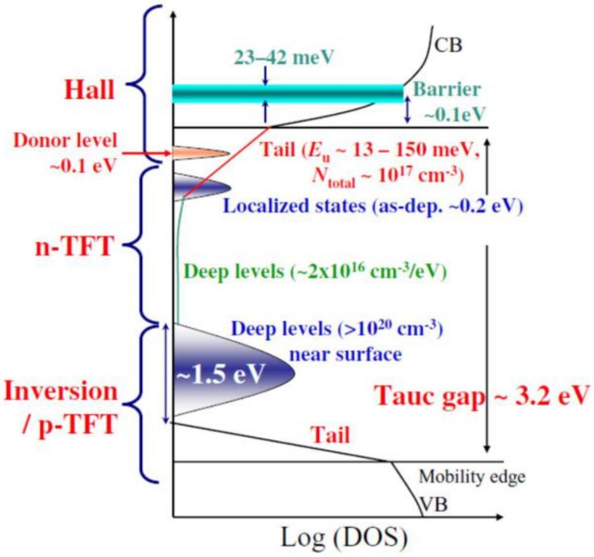

Figure 1.2. The schematic subgap defect states in a-IGZO. Reproduced with Ref. [38].

1.3 Experimental Defect Analysis Methods

It is difficult to understand the defect-induced degradation mechanism and to characterize complex defect states distribution in wide bandgap MOs semiconductor. Over the last few decades, photoluminescence (PL, optical measurement), [39-44] capacitance-voltage (CV, electrical measurement) measurement, [45-47] and deep level transient spectroscopy (DLTS, electrical measurement) [48-50] were widely used in order to characterize the electrical defect states in ZnO-based semiconductors.

The PL can directly characterize deep-level defect states but this technique cannot be employed on a working device with interfaces. The CV measurement is widely used to determine defect states especially at silicon-silicon dioxide interfaces in working metal-oxide-semiconductor transistors (MOSTFTs). However, CV method is not adequate for wide bandgap semiconductors, since energy depth level is usually limited up to 0.8–1.0 eV under the conduction band (E_c).

Regarding the DLTS, it has a high sensitivity and is more accurate for the analysis of discrete defect states and impurities using Schottky diodes and p-n junction devices. However, the limitation of DLTS is the temperature. Due to the thermal energy based analysis of wide bandgap semiconductors, DLTS can be limited in their ability to detect deep-level defect states (< 2.0 eV) under the conduction band minimum (CBM). So, only Si-based devices are widely used for DLTS measurement in the industry. One of the other ways is the photo-excited charge collection spectroscopy (PECCS). [51] The direct measure of density of charge traps is possible at the channel/dielectric interface or near the interface of a working TFT device by using threshold voltage shift under the monochromatic light illumination.

The PL can directly characterize deep-level defect states but this technique cannot be employed on a working device with interfaces. For instance the room temperature PL spectra of ZnO typically exhibits three emission peaks in the ultraviolet (UV), green, yellow and orange-red which are associated with different defects in the materials. The origins of each different defect emissions are not fully understood yet, and different hypotheses [5] have been proposed in order to explain exact mechanisms for the visible emissions (green, yellow and orange).

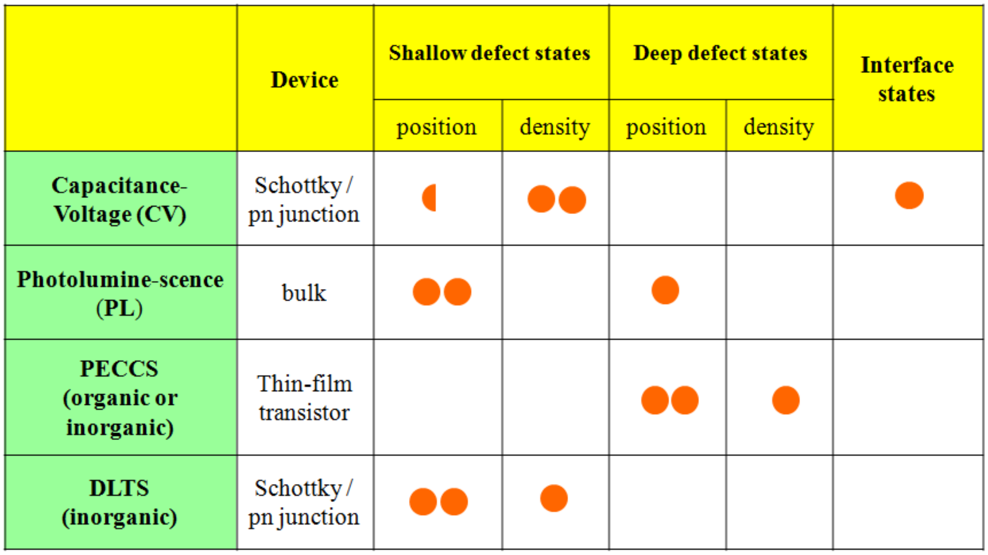

	Device	Shallow defect states		Deep defect states		Interface states
		position	density	position	density	
Capacitance-Voltage (CV)	Schottky / pn junction	◖	●●			●
Photolumine-scence (PL)	bulk	●●		●		
PECCS (organic or inorganic)	Thin-film transistor			●●	●	
DLTS (inorganic)	Schottky / pn junction	●●	●			

Table 1.2. The comparison of representative defect analysis methods in wide bandgap metal-oxide semiconductors

The UV emission should be related with the free-excitonic optical transition. It is suggested that the most commonly observed green emission (495 – 570 nm) is attributed to the V_o typically under the oxygen deficiency condition. [43, 52] However, proposed explanations for the same visible emissions (green) in ZnO are often contradictory, with different defect types. For example different explanations of this green emission have been proposed such as a singly ionized oxygen vacancy [41], or a deeply trapped hole at V_o^{++}. [53] The origin of the green emission is still controversial. On the other hand, the yellow (570 – 590 nm) and orange (590 – 620 nm) emissions are supposed to be associated with interstitial oxygen (O_i) under the excess oxygen. [42, 54] The electrical defect analysis techniques are briefly compared in Table 1.2.

1.4 Scope of Research & Overview of Research Results

In the first part of the dissertation, the Pd/ZnO Schottky barrier diode was characterized by DLTS for electrical shallow-level defect states distribution under the conduction band minimum (CBM) within ZnO bandgap. The second part of the dissertation, sputtered ZnO TFTs were characterized by PECCS method for understanding deep-level defect distribution and their effect on the device photo stability as a function of oxygen ratio [O_2/(O_2+Ar)] during sputtering growth. Finally, NBIS test of multi-component a-IZTO TFTs was also carried out with PCC measurement. Our goal is how to characterize electrical defect states in MOs semiconductor and investigating their effects on the device performance and instability under light and/or bias stress. These results can help guide improvements to material growth which in turn can help improve overall devices performance and stability under light and/or bias stress.

First of all, DLTS measurement was employed to investigate the shallow-level defect states distribution in the Pd/ZnO Schottky Barrier Diode (SBD). The electrical defect states of the single crystal ZnO have been intensively investigated to find the evidence of electrical conduction and major defect states by DLTS. However, the explicit explanation of an exact role of the defect behavior has not been fully understood. We obtained the defect states distribution under the conduction band minimum (CBM) in the ZnO bandgap.

Second, we attempt to analyze the deep-level oxygen-related defect states distribution in sputtered ZnO TFTs at different oxygen pressure during ZnO growth by measuring the shift of threshold voltage under the monochromatic light illumination, like PECCS technique. Very few papers have addressed the direct measurement of the oxygen-related defect states distribution in the working sputtered ZnO TFTs depending on the oxygen ratio and their effect on the electrical performance and stability at the same time. Since, the electrical and optical properties of metal oxide semiconductor intensely depend on their oxygen content and also annealing conditions. Characterization of the oxygen-related electrical defect states is an essential part for understanding metal oxide materials. Actually, Ar/O_2 ratio during the ZnO growth by radio-frequency (RF) magnetron sputtering doesn't guarantee the change of oxygen vacancy. However, we might say whether it is O-rich or Zn-rich states. These electrical defect states, depending on whether they are close to conduction band or valance band, or in where they are located, have distinct negative impacts on TFT's performance and stability, for example the shift of the threshold voltage, reduction of the mobility.

The effect of oxygen-related defect states on sputtered ZnO TFT's performance and stability for various O_2 partial pressure (or O_2 ratio = $O_2/(O_2+Ar)$) was investigated by comparing the electrical properties, like mobility (μ), threshold voltage (V_{th}), On/off ratio ($I_{on/off}$), and sub-threshold voltage swing (SS). Generally speaking, there was a trade-off relation between high mobility and other parameters, such as SS, V_{th} at different oxygen contents. We found out that the photo instability of devices, such as shifts of threshold voltage, occurred under visible light due to photo-ionization of the deep-level trapped charges associated with oxygen vacancies.

Third, based on the understanding of NBIS instability, the origin of this instability is attributed to subgap defect states in metal-oxide bandgaps and interfacial defects between the channel and dielectric layer. Therefore, device stability of metal-oxide TFTs mainly depends on defect states within metal-oxide thin-film itself or at the interface. This work focuses on investigating instability mechanisms of sputtered a-ITZO TFT as a function of oxygen ratio during sputtering growth under the illumination stress (IS), negative bias stress (NBS), and negative bias illumination stress (NBIS).

With increased oxygen ratio, deep-level defects associated with oxygen vacancies were partially suppressed and photo stability was improved. The oxygen vacancies were related to the persistent photocurrent (PPC) behavior under light. PPC refers to a photocurrent persisting for a long time within materials even after the light source is terminated. The ionized oxygen vacancy sites are believed to cause PPC behavior for hours. The PPC at higher oxygen ratios was also gradually reduced. As a result, we confirmed that the incorporation of oxygen during sputtering growth resulted in the reduction of deep-level defects concentration in a-ITZO TFTs. This improved the device stability under light. On the other hand, the device stability under bias stress with or without light significantly degraded at higher oxygen ratios due to the increased defect states at the interfacial layer between the channel and dielectric layer.

Chapter 2. Background

2.1 Basic Properties of ZnO

2.1.1 Structural, Electrical and Optical Properties

Most of II-VI compound semiconductors crystal structures are either cubic zinc-blend or hexagonal wurtzite. For ZnO, the stable phase at room temperature conditions is wurtzite structure, where each anion is enclosed by four cations at the edge of a tetrahedron. It has a hexagonal unit cell with the lattice constants mostly range from 3.2475 to 3.2501Å for the a-parameter and from 5.2042 to 5.2075Å for the c-parameter. [55] A schematic wurtzite ZnO structure is shown in Figure 2.1. These parameters can be measured by using X-ray diffraction (XRD) at room temperature or also reflection high energy electron diffraction (RHEED).

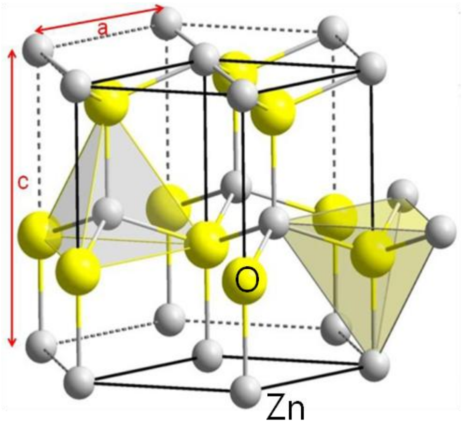

Figure 2.1. The wide bandgap ZnO crystal structure

The lattice parameter deviation from the ideal wurtzite structure is due to the lattice stability and ionicity. The intrinsic native point defects in ZnO, such as zinc antisites, oxygen vacancies, extended defects, and threading dislocations can also increase the lattice constant. As a direct wide bandgap semiconductor, ZnO-based devices have been extensively studied in various electronic and optoelectronic applications. To measure the electrical properties, Hall measurement is widely used, which provide us with carrier concentration, its type, and carrier mobility. In this work, a commercial n-type bulk single crystal ZnO was used to investigate the shallow-level defect states. It was obtained from University wafer Inc. grown by hydrothermal method. The sample was the size of 10×10×5 mm^3 with the (0001) Zn face up. The room temperature carrier concentration, carrier mobility, and resistivity were 0.86×1017 cm^{-3}, 91.9 cm^2 V^{-1} s^{-1}, and 0.85 Ωcm from Hall measurement using the van der Pauw geometry. This value is quite close to the previous mobility value. [5]

The highest room temperature mobility reported to be about 205 cm^2 V^{-1} s^{-1} for a bulk ZnO single crystal grown by vapor-phase transport method. [56] However, by various growth techniques on different substrates, room temperature mobility values of ZnO epilayers are comparable to the reported value of bulk ZnO. For instance, room temperature electron mobility up to 155 cm^2 V^{-1} s^{-1} was obtained by Kaidashev et al. [57] for ZnO thin films of thickness of 1–2 μm grown on c-plane sapphire by a multistep PLD technique. ZnO/MgO double-buffer layers grown on *c*-plane sapphire by molecular-beam epitaxy (MBE) was used by Iwata et al.. [58] They reported the highest electron mobility of 145 cm^2 V^{-1} s^{-1} at room temperature.

The optical band gap for ZnO is reported to be between 3.1 and 3.3 eV at 300 K with large exciton binding energy of 60 meV, and efficient radiative recombination. [1] Therefore, intense near-band-edge excitonic emissions can be obtained even at room temperature for the laser application. Actually, intrinsic and extrinsic optical transitions are related with the optical properties of ZnO. Intrinsic effects occur between the electrons in the conduction and the holes in the valence band. Extrinsic effects take place due to dopants or defects, which create discrete defect energy states within the bandgap. These could influence optical properties including absorption and emission processes. Defect-related optical transitions could be observed in optical signal, such as free to bound (electron-acceptor), bound to bound (donor-acceptor), and the yellow or green luminescence by using the photoluminescence (PL) at low temperature. [39, 44] Low-temperature PL has been widely used experimentally for defect-induced optical transition. [59] In undoped ZnO, most defect-related PL spectrum is dominated by the well-known green luminescence (GL) peak at around 2.5 eV in Figure 2.2. [60]

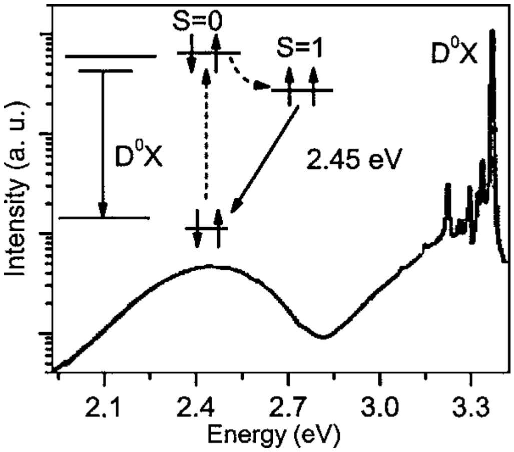

Figure 2.2. Defect-related Photoluminescence spectrum in undoped ZnO. Reproduced with Ref. [60].

2.1.2 Native Point Defects

The optical or electrical properties of undoped ZnO are closely related to its intrinsic native defects. There are very few studies of point defects in ZnO up to now. First of all, it is highly appropriate to say that intrinsic n-type conductivity in undoped ZnO is still unknown, maybe due to presence of intrinsic point defects, such as Zinc interstitial, and Oxygen vacancy, or any other impurity atoms. [25] Oxygen vacancies were considered as the origin of the shallow donors in ZnO without doping. Recently, hydrogen is regarded as the source of the n-type conductivity of ZnO instead of oxygen vacancy. [25, 61] There is not a consensus regarding which intrinsic defect (Oxygen vacancy or Zn interstitial) is responsible for intrinsic n-type conductivity without doping.

Generally speaking, native point defect concentrations are difficult to be controlled, maybe could be modified during the growth by appropriate working parameters or post-deposition anneal process under different ambient environment. The demerits of native intrinsic defects as the origin of the source of conductivity are the possibility of film re-oxidation and lower conductivity compared to the doped film. Intentional donor doping (Al, In, Ga, B, F) in ZnO can be made for a high conductivity. Most dominant native defects in ZnO are believed to be zinc interstitials (Zn_i), oxygen vacancies (V_O), and Zinc vacancies (V_{Zn}) for Zn-rich conditions due to the lower formation energies as shown in Figure 2.3. [25]

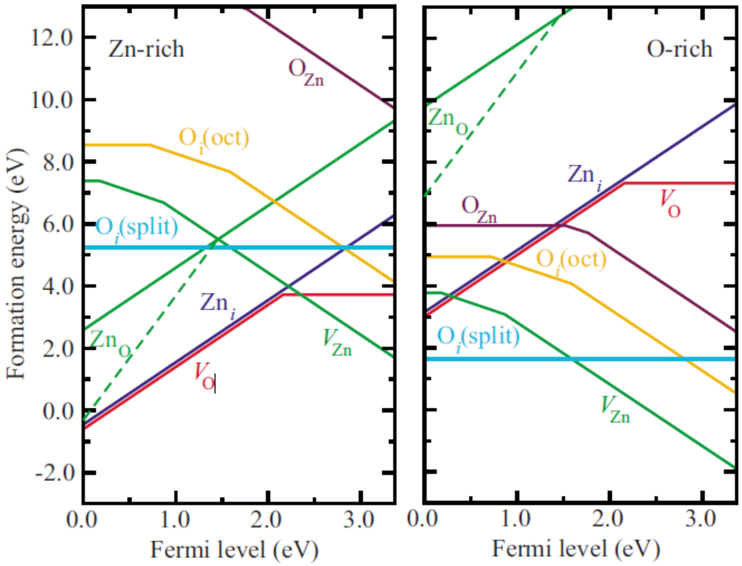

Figure 2.3. The formation energy of point defects in ZnO. Reproduced with Ref. [25].

Regarding the Zn_i, it has a high formation energy for Fermi-level near the conduction band under n-type condition as shown in Figure 2.3. The value is about 6 eV. Due to this high formation energy, Zn_i may not be the source of unintentional n-type conductivity of ZnO single crystal, since its concentrations are very low in n-type ZnO. [25] All of these formation energies are obtained by first-principles calculations under thermodynamic equilibrium and may not be described as conditions during real growth environment. [62] The migration barrier energy of the Zn_i turned out to be low about 0.57 eV. This low migration barrier energy makes Zn_i unstable at room temperature and they will be very likely to diffuse out of the sample or to get along with other defects or impurities. This also makes the Zn_i difficult to contribute to unintentional n-type conductivity in ZnO. [25]

One of the most common intrinsic defects in n-type ZnO is the oxygen vacancy. Recently, the oxygen vacancy is turned to be a deep rather than a shallow donor with its 1+

charge state (V_O^{+1}) thermodynamically unstable by the first-principles calculations. [27] Therefore, it is believed that the V_O is not the source of intrinsic n-type conductivity in undoped ZnO. On the other hand, there are several experimental reports that the formation of the shallow donor states is attributed to hydrogen. [26, 61, 63] And, when the Fermi-level is near the conduction band, the V_O usually presents in a neutral state as shown in Figure 2.4. [27]

The defect transition level ε(2+/0) is defined as the Fermi-level position for which the formation energies of the two charge states 2+ and 0 are equal. From Figure 2.4, the V_O will be changed to V_O^{2+} when the Fermi-level position is below the transition level ε(2+/0) by the calculation under the local density approximation (LDA). This means that the V_O and V_O^{2+} states are stable, while the V_O^{+} state is thermodynamically unstable state which could be observed under the optical excitation. Actually, the V_O^{+} state is unstable at any Fermi-level position within the band gap. So, this unstable state with unpaired electron (only the positive charge state) is detectable under light by magnetic resonance method, such as the electron paramagnetic resonance (EPR). [41, 43] Interestingly, this excited V_O^{+} state does not immediately return back to the V_O and V_O^{2+} states, even at room temperature. This causes the persistent photoconductivity (PCC) in metal oxide materials. The reason for this situation is related with the existence of energy barriers associated with the large lattice relaxations that occur around the oxygen vacancy. The position of the ε(1+/0) transition level in the band gap is located at 2.0 eV. [27]

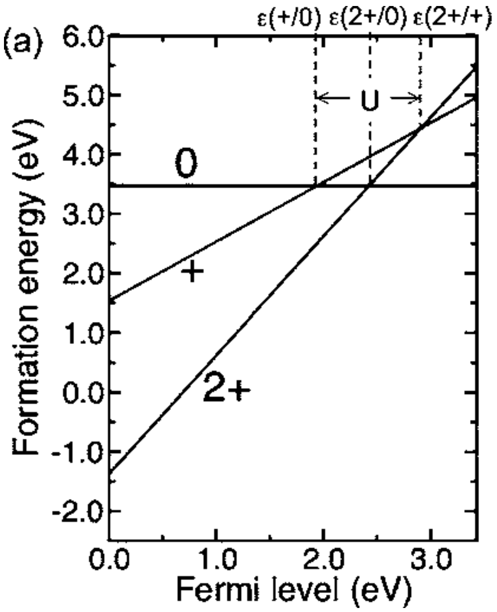

Figure 2.4. Formation energy depending on the oxygen charge state in ZnO. Reproduced with Ref. [27].

The zinc vacancies can be formed in ZnO by removing of a Zn atom, which results in nearest four oxygen dangling bonds. These dangling bonds introduce partially occupied defect states in the band gap. These defect states lie close to the valance band maximum (VBM) and can accept up to two more electrons, indicating a deep-level acceptor behavior of V_{Zn} in ZnO and this V_{Zn} can easily form in n-type materials due to the lowest formation energy as shown in Figure 2.3. Therefore, it can be regarded as a compensating center in n-type ZnO. [26] In fact, it was identified as the dominant compensating center by positron annihilation measurements. [64, 65]

2.1.3 Growth of Bulk ZnO & Epitaxial Growth of ZnO Thin Films

Zinc oxide bulk can be grown by several methods, such as chemical vapor transport, [66] hydrothermal method, [67] and pressurized melt-growth technique. [68] Each method involves different growth mechanisms, with different impurity concentration, resulting in different electrical and optical properties. [55] Among these methods, the hydrothermally grown single crystal ZnO (Figure 2.5) has been used to characterize the shallow-level defect states in Pd/ZnO schottky diode by using the DLTS.

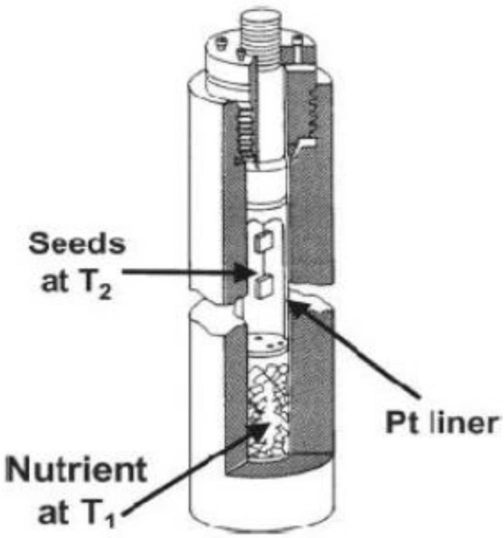

Figure 2.5. Hydrothermal growth of ZnO single crystals.

Hydrothermal method uses ZnO seeds (suspended by Pt wire) and nutrient, including a KOH, LiOH aqueous solutions with sintered ZnO pellets. These are all placed in a Pt crucible, which is placed in an autoclave. This clave is divided into a two-zone vertical furnace. ZnO is transferred from T1 zone (higher temperature for the nutrient) to T2 zone (lower temperature for the seeds) as shown in Figure 2.5. About 10 mm bulk ingots in size after 2 weeks can be grown by using this hydrothermal method. The advantages of this growth is that this growth method can provide a truly bulk freestanding wafers up to 3 inch size. Furthermore, high quality crystal structure can be available due to the negligible thermal stress during growth.

However, the incorporation of impurities is unavoidable, which is coming from the solvent, such as Li and K. These may affect the electrical properties of this type of sample.

Although high quality single crystal ZnO substrates are available from the hydrothermal method, most ZnO epitaxial layers have been grown on sapphire, GaAs, and GaN. ZnO thin films have been deposited using a number of methods, including DC or RF magnetron sputtering, [69, 70] chemical spray pyrolysis, [71] metal-organic chemical vapor deposition (MOCVD), [72] and pulsed-laser deposition (PLD). [73] More recently zinc oxide thin films have been often fabricated from solution-based precursors. Most of these polycrystalline films have been used for current applications of ZnO, such as transparent channel layer for switching TFTs, conductive electrodes for solar cells, [74] piezoelectric devices, [75] and gas sensors. [76, 77]

One of the most popular methods was sputtering for a long time (DC sputtering, RF magnetron sputtering, and reactive sputtering) due to the simplicity, low cost, and low operating temperature, as well as the possibility of large area deposition. [6] The schematic diagram of a typical RF magnetron sputtering is shown in Figure 2.6. Atoms are ejected from a target by energetic particles (Ar^+) and transported to the substrate in an ambient of mixing O_2 and Ar with ratios ranging from 0 to 1 in plasma at a pressure of 10^{-3}–10^{-2} Torr. O_2 is regarded as the surface reactive gas and ionized Ar^+ is supposed to act as the sputtering enhancement gas. In our work, ZnO or Indium-Tin-Zinc-Oxide (ITZO) was deposited as a transparent channel layer in switching TFTs as a function of oxygen partial pressure during RF magnetron sputtering growth to characterize the deep-level defect states, which may be associated with oxygen vacancies.

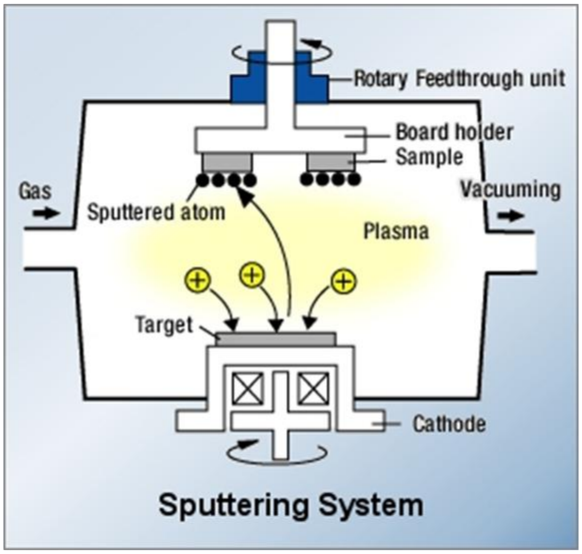

Figure 2.6. Typical RF magnetron sputtering system

There are a lot of working parameters that can affect on films characteristics during sputtering growth. In an instance, films can be influenced by the substrate temperature, target composition, oxygen ratio ($O_2/(O_2+Ar)$), gas pressure, target power, and so on. Among these parameters, oxygen ratio plays an important role during the film deposition in RF sputtering, because it may be related with deep-level defects associated with oxygen vacancies during growth at different oxygen ratios. An oxygen-rich condition can lead to increased oxygen incorporation, resulting in a reduction of deep-level oxygen-related defects. Control of this parameter is essential to modify the electrical/structural properties of metal-oxide films, and stoichiometry associated with oxygen vacancies. At the same time, the growing film could be damaged by an intense ion bombardment under the dense plasma during sputtering. For example, the high-energetic oxygen ions could be accelerated and bombard the substrate during the RF discharge. These ions are generated near the target, and move with a high energy from the target to the substrate surface. The Ar^+ and O^- bombardment is the main part in RF discharges, so it is very important in a growing film. Ion bombardment could be also determined by other working parameters such the working gas pressure, target-substrate distance, and substrate bias voltage. It is very difficult to accurately analyze the effects of variables on the surface morphology. It was shown that the surface morphology of the films strongly depends on the substrate temperature during growth. Generally speaking, higher energy flux arriving at the surface is needed at room temperature to form a coating with higher crystallinity.

2.2 Metal Oxide Semiconductors

2.2.1 Conduction Mechanism and Conductivity Control

Single metal oxides, which are usually in the polycrystalline state, such as ZnO, In_2O_3 have been investigated as transparent conductive oxides for decades. These have been also studied as semiconductors for transparent TFTs for the last decade. The measured Hall mobility for different carrier concentrations is shown in Figure 2.7 for doped and undoped ZnO. [78] The carrier transport mechanisms are controlled by two mechanisms; grain-boundary-limited transport and ionized impurity scattering. The grain boundaries can trap charges, and interrupt the electron transport, indicating potential barriers between boundaries reference to the conduction band minimum. This barrier height decreased with increasing carrier concentration, at the same time ionized impurity scattering dominates the carrier transport. In this process, there is a maximum mobility transition point, which is about 10^{20} cm^{-3} in ZnO as shown in Figure 2.7. As a matter of fact, it is difficult to achieve both a high mobility and a high carrier concentration for TFTs.

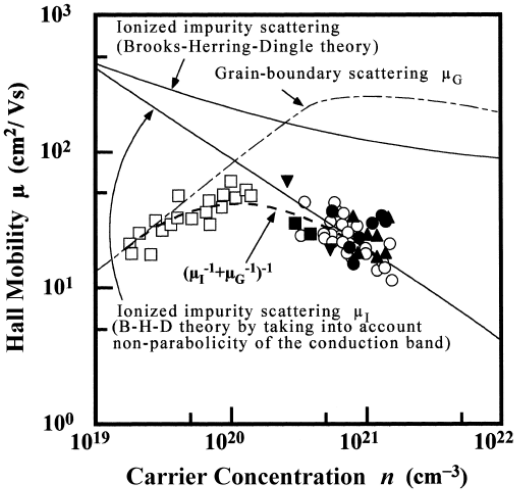

Figure 2.7. Hall mobility for different carrier concentrations. Reproduced with Ref. [78].

Instead of single-metal oxides, multi-component metals can be involved in forming the crystalline or amorphous structure of oxides semiconductor, for example the amorphous In-Ga-Zn-O system (a-IGZO), with a composition of about 1:1:1:4, is a good example in this multiple metal oxides category. [2, 7, 79] It is expected that the barrier from the grain boundary scattering can be eliminated due to the amorphous state. However, it is observed that electron transport is still limited by a potential barrier due to random distribution of multi-metal cations, which is called the percolation conduction model. [80] This barrier is suppressed when carrier concentration is over 3×10^{18} cm^{-3}, showing an increase in mobility with an increase in carrier concentration in Figure 2.8. [7] This relationship remains the same even for single-crystalline IGZO. By changing the composition of a multi-metal oxide, *i.e.*, making an IGZO with a different ratio, a higher mobility can be obtained. [69] On the other hand, oxide semiconductors such as a-ITO, which have high-density carriers, are difficult to make into devices with controlled characteristics. So, it is critical to choose a material in which carrier concentration can be controlled at a low level, for example, 10^{14} cm^{-3}, in order to achieve a low off current. [16]

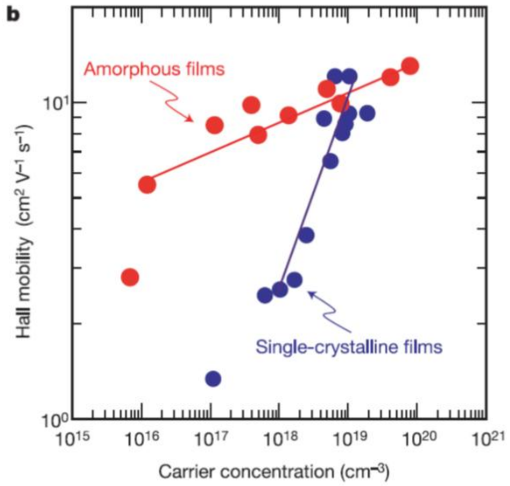

Figure 2.8. Relationship between hall mobility and carrier concentration for a-IGZO films. Data on single-crystalline $InGaO_3(ZnO)_5$ films are shown for comparison. Reproduced with Ref. [7].

It is still interesting about the conduction mechanism of amorphous semiconductors. How could they still remain the high mobility (10–100 cm^2 V^{-1} s^{-1}) even in the amorphous state? As already mentioned in chapter 1, they have much improved performance compared to conventional a-Si:H TFTs. They can be deposited as a uniform amorphous phase while retaining the high mobility. It seems like that the reason is due to the large neighboring metal ns-orbital overlap. So, their carrier transport path is independent of metal-oxygen-metal chemical bonding direction as illustrated in Figure 2.9. [7] These properties are completely different from those of the covalent semiconductors, such as silicon. Therefore, amorphous oxide semiconductors have mobilities similar to those of the corresponding crystalline phase. These carrier transport properties are unique to oxide semiconductors.

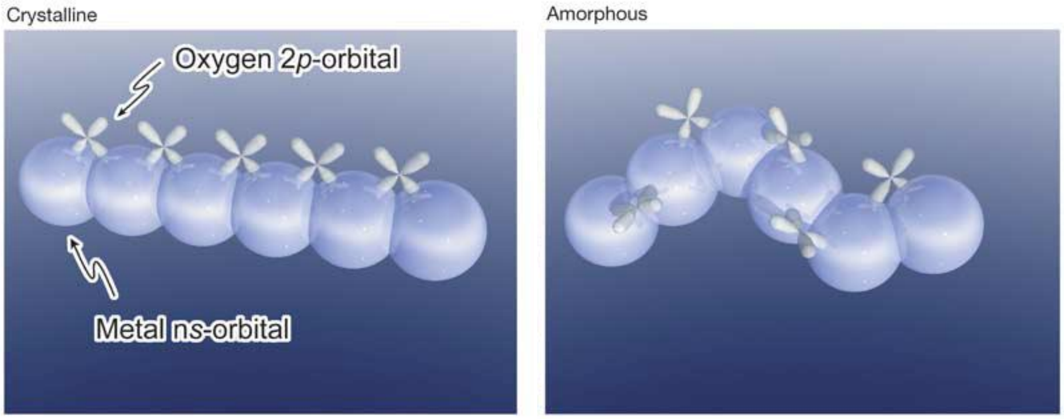

Figure 2.9. Spheres denote metal s orbitals. The contribution of oxygen 2p orbitals is small. Direct overlap between neighbouring metal s orbitals is rather large, and is not significantly affected even in an amorphous structure. Reproduced with Ref. [7].

It is noted that most as-grown ZnO by several growth techniques is native n-type without doping. For semiconductor device applications it is highly desirable to have better control over the conductivity. The controlling the n-type conductivity is related with difficulties in understanding the actual cause of intrinsic conductivity due to the defects or impurities. Since, it is difficult to measure the impurity concentrations and measurements of stoichiometry are even more difficult than that. Impurity concentrations down to the ppm range are not available to be measured quantitatively until the 1990s and only the use of secondary-ion mass spectroscopy (SIMS) has made a big impact on this technique. In addition to this difficulty in the n-type conductivity control, the biggest challenge in research on metal oxide semiconductor is how to achieve the p-type doing. [5] There were several reports on this in the literature. [81, 82] However, no reliable and reproducible devices have been reported until now.

2.2.2 Metal Contacts on Wide Band gap Semiconductor

If a metal is deposited on one side of a semiconductor in an ideal way, an ohmic contact or a rectifying contact (Schottky barrier contact) is formed, depending on the difference between the work function of metal and semiconductor. [83] An ohmic contact has a linear current-voltage relationship at positive and negative voltages, allowing current to flow into and out of the semiconductor. It is essential to achieve an ohmic contact with low contact resistance and make it thermally stable for electrical devices. A minimum specific contact resistivity of 6×10^{-4} Ωcm^2 for Ti/Al/Pt/Au contacts was obtained on undoped $n=10^{17}$ cm^{-3} bulk ZnO by Ip et al. [84]. This minimum ohmic contact resistivity was reached after 250 ℃ annealing. Higher annealing temperature degraded the contact resistivity by intermixing of the metal layers and reaction of Ti with ZnO.

In particular, formation of high quality Schottky contacts on n-type ZnO is necessary for ZnO device applications, and also many different high work function metals such as Au, Ag, Pt and Pd have been applied to the ZnO surface. [5, 85] Surface treatment prior to metal deposition is essentially important. As a matter of fact, the formation of high quality Schottky contact on wide band gap semiconductor (e.g. ZnO) is not directly related to the metal work function due to the surface states, the contaminants, the defects in the interfacial surface, the diffusion of metal into the semiconductor and so on. [5, 86] Some metals like Ag, Au, Pt and Pd form relatively high Schottky barriers of 0.6 ~ 0.85 eV to n-type ZnO.

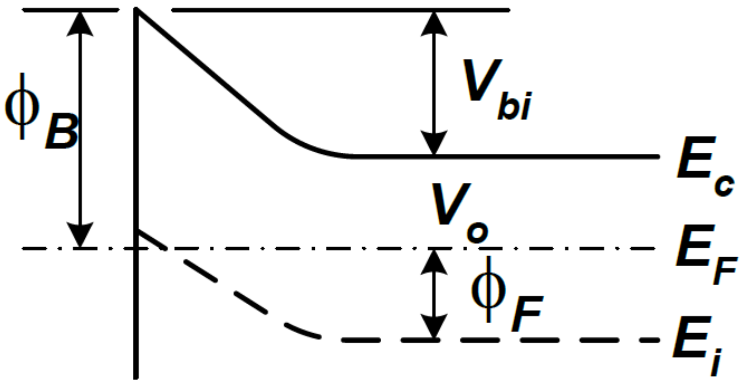

Figure 2.10. Schematic illustration of Schottky barrier potential band diagram

The thermal stability of the Schottky diodes and the effect of surface treatments have not been extensively studied. Au has been widely applied to n-type ZnO surface to form Schottky barriers, although Au has some serious problems, such as thermal degradation due to the thermal cycling. The thermal stability of Ag Schottky contacts was better than that of Au Schottky contacts. [87] It was observed that both Au and Ag Schottky diodes have shown to degrade easily with thermal cycling even as low as 365 K. [85] This has been explained by different mechanisms such as the tunneling, the presence of an interface layer, and surface defect states. Schottky barrier heights of 0.65–0.69 eV and diode ideality factors of 1.3–2.0 have been usually reported by capacitance-voltage and current-voltage measurements, respectively. [5] The band diagram of Schottky barrier diode on an n-type ZnO is shown in Figure 2.10. V_{bi} is the built-in potential and V_O is the potential of the semiconductor Fermi level with respect to the conduction band.

2.3 Multi-Component Metal Oxide Properties

Single metal oxides such as ZnO, In_2O_3, and SnO_2 have a crystalline structure, hexagonal (wurtzite), cubic (bixbite), and tetragonal (rutile), respectively. Over the past few decades, they have been explored as channel layers for TFT fabrications. However, SnO_2 channel layer is not suitable binary oxide for TFTs due to the high deposition temperature. [88] The device performance exhibited mobility of 2.0 cm^2 V^{-1} s^{-1} and $I_{on/off}$ of 10^5. The In_2O_3 TFTs can achieve a high mobility of 30 cm^2 V^{-1} s^{-1} [89] due to the overlap of In 5s orbital. [90] On the other hand, it is hard to control the high density of defect sites in In_2O_3, which results in very poor TFT stability. In addition, binary oxide semiconductors are polycrystalline in nature with poor uniformity, which are not suitable for the active channel in TFTs.

However, when one of these is mixed with a certain ratio, an amorphous ternary, or multi-component metal oxide materials can be obtained to enhance the device performance, for example including a-InZnO, a-InGaZnO, a-ZnSnO, a-InSnO, and a-InZnSnO TFTs with higher electron mobility (~40 cm^2 V^{-1} s^{-1}). [2] All of these materials show n-type conductivity due to the existence of intrinsic donors. Most of these multi-component oxide materials are also amorphous, which can be beneficial for high uniformity. When the In to Zn ratio increases, both the mobility and carrier concentration increase. For example, in 2007, InZnO TFTs, with composition of In2O3:ZnO (9:1), achieved a mobility of 107.2 cm^2 V^{-1} s^{-1}. [91] Among these materials, a-InGaZnO) has been the most dominant material for AM-OLED applications due to the high mobility (~20 cm^2 V^{-1} s^{-1}) and low off current (~10^{-12} A) after Nomura’s proposal in 2004. [7] Here, Ga has been used to suppress the carrier concentration due to its high ionic potential and small ionic radius of Ga^{3+}. This Ga could attract oxygen ions tightly, and thereby suppress oxygen vacancies in the film. [16]

Recently, the ternary metal oxide systems, which consist of In_2O_3, SnO_2 and ZnO, have shown advanced electrical performance for TFTs active layer with a high mobility, and on/off ratio. The a-ITZO TFT can exhibit the mobility of 30 $cm^2\ V^{-1}\ s^{-1}$ [92, 93] with more than twice times mobility of a-IGZO TFT. The 56" a-ITZO OLED TV was demonstrated by AUO which showed a good image quality. [94] The previous researches on multi-component oxide TFTs are shown in Table 2.1.

Table 2.1. The previous researches on multi-component metal oxide TFTs

Year	**Significance**	**Growth Method**	**Mobility ($cm^2\ V^{-1}\ s^{-1}$)**	**Ref.**
2004	First transparent flexible amorphous-IGZO TFT	PLD	8.3	Nature 2004, 432, pp 488 [7]
2005	Transparent ZTO TFT	Sputtering	20 – 50	APL 2005, 86, 013503 [95]
2007	Amorphous IZTO structure up to 600℃	Co-sputtering	19.0	J. Phy. D. 2007,40, 1335 [96]
2010	Nanocrystalline ZnO TFT	PLD	100.0	Device Research conference 2010 [97]
2011	Low-temperature combustion synthesis with solution process	Combustion-based solution process	13.0 (In_2O_3 TFT)	Nature Mater. 2011, 10, pp382 [98]
2014	High mobility of a-IZTO TFT	Sputtering	52.0	IEEE EDL 35, 8, 853 [93]
2016	Wet pulse annealing for low temperature process	Sputtering	13.3	Scientific reports 2016 [19]

2.4 Schottky Diode and Deep Level Transient Spectroscopy (DLTS)

2.4.1 Schockley-Read-Hall (SRH) Recombination

All semiconductors have defects, such as impurities or intrinsic native defects. These foreign atoms or crystalline native defects can be introduced as dopant atoms (usually shallow-level) or recombination centers (deep-level), respectively. Various types of crystal defects could be present as interstitial, substitutional, vacancy, stacking fault or precipitate within semiconductors. In this chapter 2.5.1, we will discuss several generation-recombination processes, and the electrical measurement of defect (or impurity) density and energy level. Impurities (foreign atoms) or crystal defects can introduce the discrete energy levels into the band gap, as shown in Figure 2.11. [83]

These are generally called generation-recombination (G-R) centers, which commonly lie deep in the band gap, or simply deep-level impurities. Definitely, deep-level defects can capture electrons and holes, also they can emit electrons and holes. They behave like recombination centers when there is a surplus of carriers in the semiconductor. In this case, the rate of recombination becomes greater than the rate of generation. Likewise, they act as generation centers when there is a deficit of carriers in the semiconductor, the generation rate becomes greater, driving the system towards equilibrium. Whereas, those defect with energies near the band edges act as traps. It depends on defect energy level, the location of Fermi level, and temperature, whether they act as a G-R center or a trap center. For example, the defect center in Figure 2.11 (a) first capture an electron from the conduction band, represented by the capture coefficient c_n. After this process, this defect center can either emit the electron to the conduction band by the emission rate e_n (Figure 2.11 (b)), or it can capture a hole from the valence band, shown in Figure 2.11 (c) as c_p. After this event, again it has two choices. It can emit the hole back to the valence band in Figure 2.11 (d) as e_p or captures an electron again (Figure 2.11 (a)). Both (a) and followed by (b) process is related with a recombination process. On the other hand, a generation process is involved with (b) and followed by (d). [83]

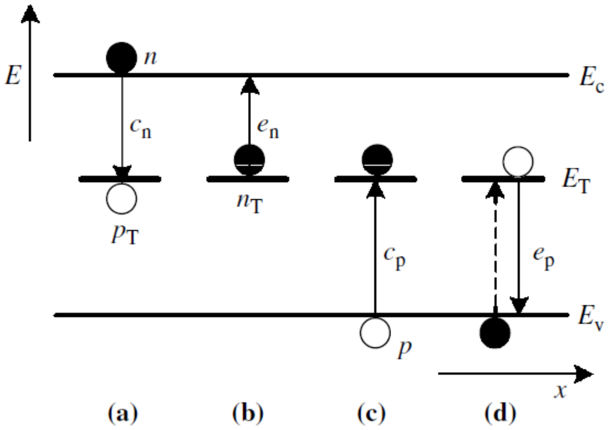

Figure 2.11. The capture and emission processes with deep-level impurities. Reproduced with Ref. [83].

Recombination occurs when an electron in the conduction band moved into a lower energy state in the valence band. There are typically three types of recombination: band-to-band recombination, auger recombination, and Shockley-Read-Hall (SRH) recombination, shown in Figure 2.12. [99] Band-to-band recombination involves the direct recombination between conduction band electrons and valence band holes by emitting the energy as a photon, so this process dominates in direct band gap semiconductors. Auger recombination is associated with three particles, two in the conduction band and one in the valence band. When the first electron in the conduction band combines with the hole in the valence band, the released photon energy during this process could be absorbed into the second electron in the conduction band, pushing it high into the conduction band. Finally, in SRH recombination, the recombination occurs via a recombination center (intermediate defect level) between the conduction and valence band, as mentioned above. Therefore, SRH recombination is also called as trap-assisted recombination.

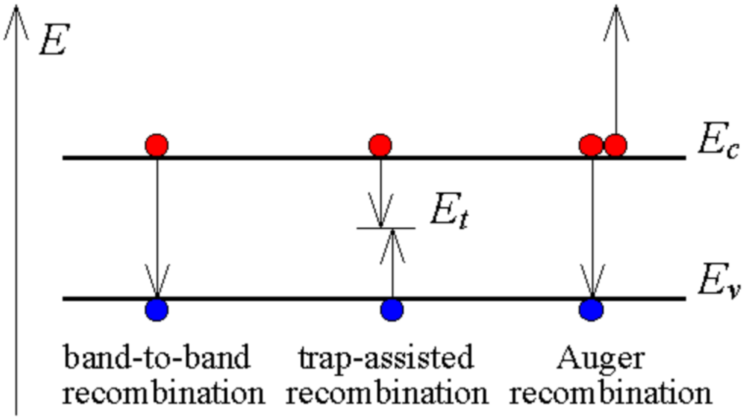

Figure 2.12. Carrier recombination mechanisms in semiconductors. Reproduced with Ref. [99].

Among these, SRH recombination can decrease the radiative efficiency and also carrier lifetime. [99] In the SRH recombination process, an electron and a hole are only considered with a recombination center (often called traps). This SRH recombination process depends on the capability of a trap (G-R center) to capture or emit an electron. These abilities are represented by emission and capture rates. The emission rate e_n [1/s] means the electrons ejected into the conduction band from a trap per second, and the capture rate $c_n N_t$ [1/s] is proportional to the capture coefficient c_n (= $\sigma_n \nu_{th}$) and the concentration of trap N_t for indirect transitions. [83] Here, σ_n is the electron capture cross-section of a trap, and ν_{th} is the electron thermal velocity. So, the capture rate means the electrons captured per second from the conduction band. In equilibrium conditions, capture process and its inverse must balance inside the material. This is called the principle of detailed balance. This means the process (a) in Figure 2.11 should be balanced with its inverse process (b), therefore this represents the relationship between capture and emission rate, which is $c_n N_t = e_n$ under equilibrium conditions. The carrier life time (also called the emission time constant, τ_e [s]) is inversely proportional to the emission rate (e_n), which is shown in Equation (2.1). Consequently, the carrier life time is related with capture cross section, thermal velocity, and defect density, which are dependent on temperature, in the well-known way: [83]

$$\tau_e = \frac{1}{e_n} = \frac{1}{C_n N_t} = \frac{1}{\sigma_n \nu_{th} N_t} = \frac{\exp\{(E_c - E_t) / KT\}}{\sigma_n \nu_{th} N_c} \qquad (2.1)$$

where N_c, E_c, and E_t is the effective conduction band density of state, conduction band minimum, and trap energy level below the conduction band minimum, respectively. To eject electron from the trap to the conduction band, an energy difference $\Delta E = (E_c - E_t)$ is required, which is actually Gibbs free energy. So, the emission time constant or carrier life time, τ_e depends on the energy E_t and the capture cross-section σ_n. The other parameters, such as ν_{th}, and N_c depend on the temperature. The detailed discussion about this will be mentioned in the next section with the deep level transient spectroscopy (DLTS).

2.4.2 DLTS Principles with Schottky Diode

DLTS was invented by Lang in 1974 [100] and this technique can measure the electrically active defect energy level, concentration of defect and capture cross section. Capture and emission process in Figure 2.13 had been used to characterize them. The emission of trapped carriers can change the depletion capacitance of *p-n* junction or Schottky diode. By measuring the transient cap during this process, it provides information on the defect within the band gap. It is commonly used for characterizing point defects in silicon semiconductors.

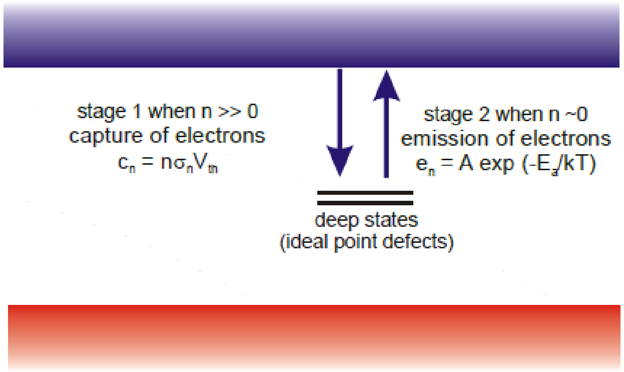

Figure 2.13. Deep level defect state with capture and emission process

Basically it is based on changing the occupancy of defect levels by changing the bias of the diode. Bias applied from reverse to zero (or positive) enough to fill the trap levels during a designated time. And then trapped carriers are emitted by reverse bias. When carriers are emitted, the transient capacitance of diode changes at the same time. The transient capacitance increases following majority carrier emission in p-n junction diode, in case of minority carrier emission, the transient capacitance decreases as shown in Figure 2.14.

The mechanism behind this behavior is that majority electrons are emitted from the traps or defects into the conduction band, the charges in the depletion width change from neutral to positive. Therefore, total ionized density increases, the depletion width decreases. Finally, the transient capacitance increases with time. This situation is opposite to minority carrier emission, which is also shown in Figure 2. 14.

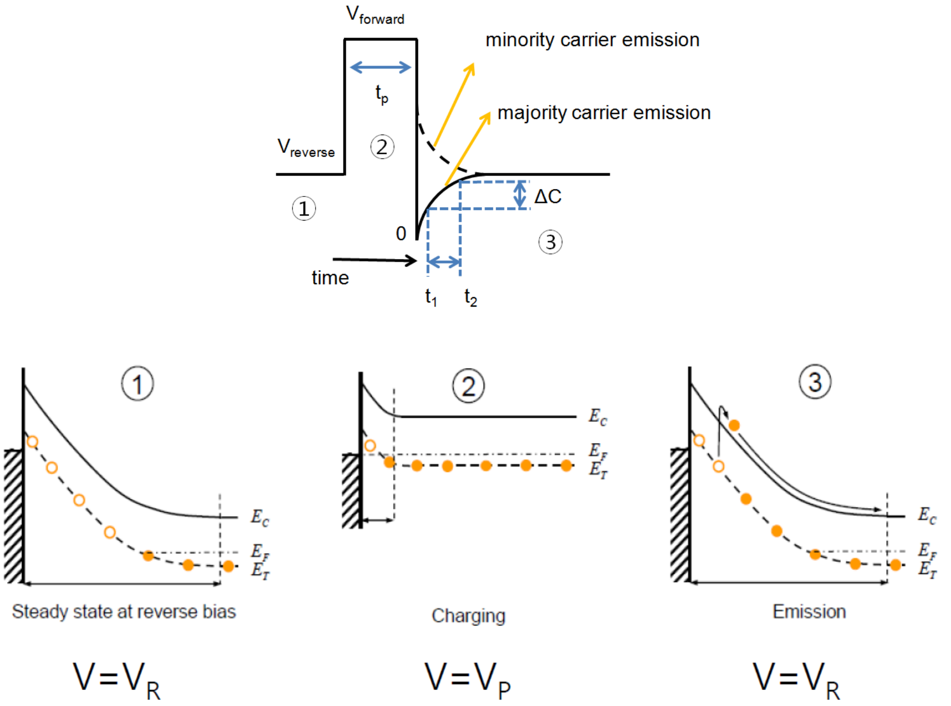

Figure 2.14. Applied voltage and resultant transient capacitance in a Schottky diode for reverse bias, forward bias during the pulsing time (t_p), and again for reverse bias as t → ∞.

Emission rate depends on the temperature, trap energy level from the conduction band, and also capture cross-section from Equation (2.1). If we know a set of the emission rates at specific temperatures, we can find the trap energy level and capture cross-section from Equation (2.1) or (2.2), since the other parameters, such as the electron thermal velocity ($\nu_{th} = (3kT/m_n)^{1/2}$), and effective density of states in the conduction band ($N_c = 2(2\pi m_n kT/h^2)^{3/2}$) are all temperature-dependent. The emission time constant (carrier lifetime) can be also written as: [83]

$$\tau_e T^2 = \frac{\exp\{(E_c - E_t)/KT\}}{\gamma_n \sigma_n} \quad \text{or} \quad \frac{e_n}{T^2} = \gamma_n \sigma_n \exp\left(-\frac{E_c - E_t}{KT}\right) \qquad (2.2)$$

with $\gamma_n = (\nu_{th}/T^{1/2})(N_c/T^{3/2}) = 3.25\times10^{21}(m_n/m_O)$ $cm^{-2}s^{-1}K^{-2}$, where m_n is the electron density-of-states effective mass and m_O is the electron rest mass. To calculate this, the rate window concept is used as the basis of DLTS technique. The change of transient capacitance in a fixed rate window is monitored as temperature is varied as shown in Figure 2.15. DLTS signal produces a maximum peak at certain temperature when the emission time constant is determined by t_1 and t_2 ($\tau_e = (t_2 - t_1) / \ln(t_2/t_1)$). This kind of DLTS system is known as double BOXCAR DLTS. [100] At different settings of t_1 and t_2, the DLTS signal gives out a different set of emission time constant (τ_e) and certain temperature and trap emits carriers at that emission rate ($e_n = 1/ \tau_e$). By using an Arrhenius plot of $\ln (e_n/T^2)$ vs. $1/T$, the trap energy level (E_t) and capture cross-section (σ_n) can be obtained by Equation (2.1) or (2.2). [83] Therefore, the temperature dependent emission time constant at different rate window informs us about the trap energy level and capture cross section area by DLTS system.

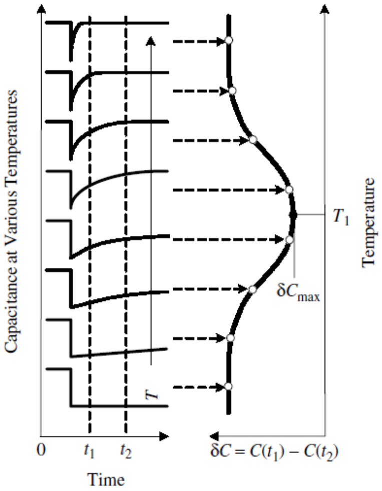

Figure 2.15. Illustration of how to define the rate window (time t_1 and t_2) as a double boxcar DLTS system. The left-hand side shows the transient capacitance at various temperatures at time t_1 and t_2, with the right-hand plot corresponding DLTS signal. Reproduced with Ref. [83].

In addition, DLTS signal is actually the distribution of signal originated from each trap level. So, the DLTS signal is simply proportional to the trap concentration by the given equation (2.3): [83]

$$N_t = 2N_d \frac{\Delta C_{max}}{C_o} \quad (2.3)$$

where N_d is the carrier concentration, ΔC_{max} is the maximum transient capacitance amplitude at t = 0 in Figure 2.14 and C_O is the capacitance of the Schottky diode under reverse-biased conditions. For the DLTS measurement, the most important thing is the rectifying behavior of schottky diode or junction diode. To measure the DLTS, the reverse leakage current should be at least less than 10^{-5} A. Otherwise, the leakage current will interfere with the emission process carriers. Finally, trap concentration should be less than 15% of carrier concentration. Above 15 % level, DLTS signal starts to be distorted.

2.5 Metal-Oxide Thin-Film-Transistors (TFTs) and Instability Mechanism

Thin-film transistors (TFTs) serves as a switching or driving device to turn on/off each pixel in liquid crystal display (LCD) or active matrix organic light-emitting-diode (AMOLED) backplane. Recently, instead of the amorphous Silicon (a-Si) semiconductor, metal oxide semiconductor materials have been attracted a lot of attentions as a channel layer. The metal oxide semiconductors, such as ZnO, ZnSnO (ZTO), InZnO (IZO), InGaZnO (IGZO), and InSnZnO (ITZO), have been widely investigated due to high device performance, which is already mentioned in the introduction. These novel TFT was compared based on their device parameters, like field-effect mobility (μ_{fet}), on/off ratio (I_{on}/I_{off}), threshold voltage (V_{th}), and sub-threshold voltage swing (SS). The brief description of metal oxide TFT structure, basic operation, and performance assessment will be given in the following sections.

2.5.1 Basic Operation and Device Performance Assessment

TFTs' basic working principle is how to control the current flowing in a semiconductor between source and drain. The insulation layer (also called dielectric layer) is placed between the semiconductor and a gate electrode, as shown in Figure 2.16. The conductance modulation of the semiconductor channel layer can be achieved by controlling the capacitive injection of carriers at the dielectric/semiconductor interface, using the gate voltage. Basically, TFTs are three terminal field-effect devices, which are source, drain, and gate electrodes. Depending on the position of the gate electrode and the source/drain electrodes, the structures are classified as top- /bottom-gate or staggered/ coplanar. [2] Most conventional bottom-gate TFT structures are shown in Figure 2.16. In our research, the staggered bottom-gate TFT structure is applied as a reference. Highly doped Si substrate coated with 100 nm or 300 nm of thermally grown SiO_2 was used as a gate electrode.

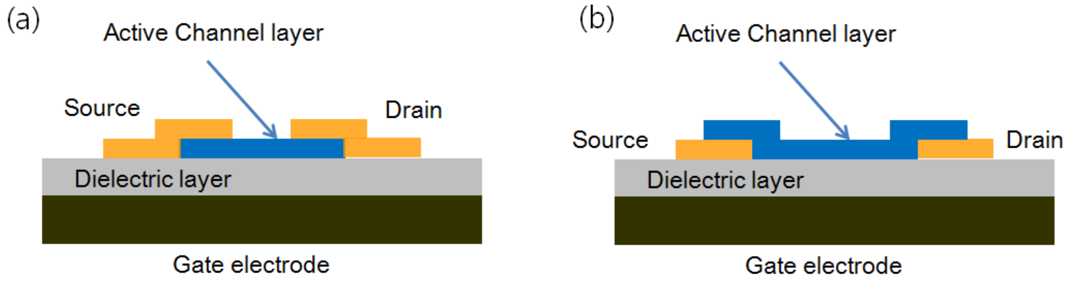

Figure 2.16. TFT structures; (a) staggered bottom-gate (b) coplanar bottom-gate structure

The operation of n-channel TFT is schematically shown in Figure 2.17. In order to attract electrons from the source to the drain, a small positive voltage is applied to the drain electrode. If the gate voltage, V_g is less than the threshold voltage, V_{th}, no drain current flows, since the electron accumulation layer does not exist between the source and the drain. This region is represented in Figure 2.17 (a).

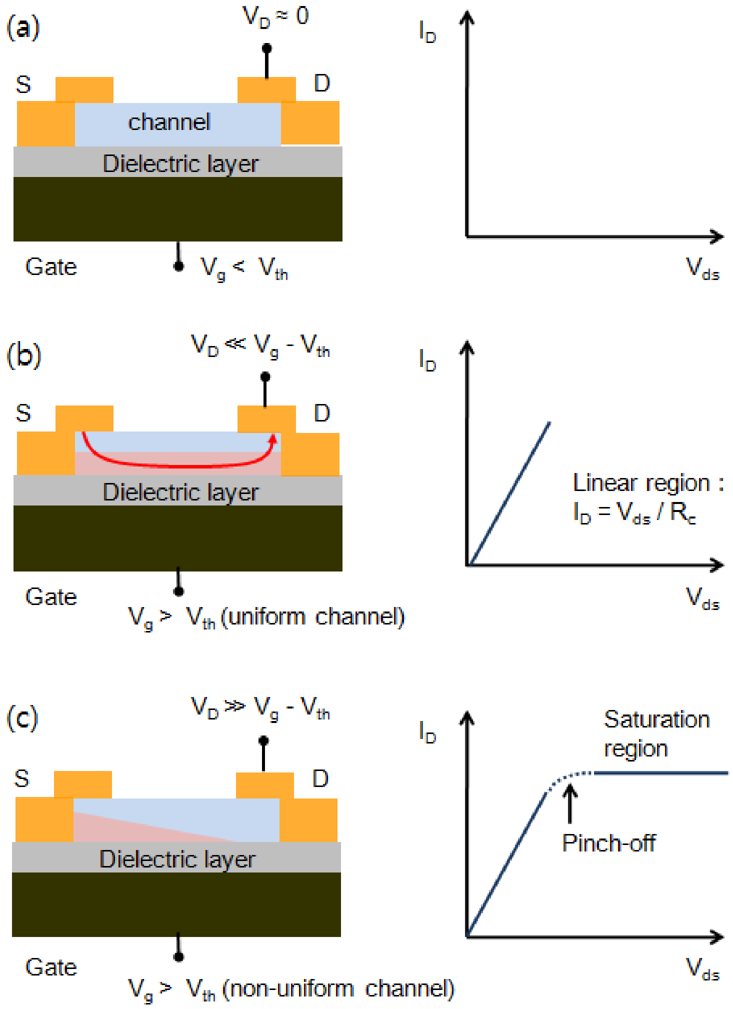

Figure 2.17. Ideal operation of an n-channel thin-film transistor (TFT) (a) Cur-off region. Drain current is zero, and corresponds to the no electron accumulation layer occurs at the channel/dielectric interface. (b) Linear region. Drain current can be represented by the Ohm's law at low V_{ds}, and corresponds to the formation of a uniform electron accumulation layer at the channel/dielectric interface. (c) Saturation (post-pinch-off) region. I_D becomes saturated with respect to V_{ds} due to the depletion or 'pinch-off' of the electron accumulation layer at the interface, and the channel layer became non-uniform.

On the other hand, if the V_g becomes greater than V_{th} while a small positive voltage is still applied to drain electrode, drain current starts to flow, as shown in Figure 2.17 (b). The electron accumulation layer is formed between the channel and dielectric interface by the gate-voltage-induced field effect. This gate voltage determines the charge density in the accumulation layer. For small V_D (i.e., for $V_d << V_g – V_{th}$), drain current in the channel layer can be described using Ohm's laws. R_c is the resistance of the channel in Figure 2.17 (b).

As the magnitude of this drain voltage becomes increasing, V_D can be comparable to the overvoltage ($V_g – V_{th}$), then drain current is no longer linear with respect to the V_D. The drain current finally becomes saturated when pinch-off occurs at $V_D = V_g – V_{th}$. In this situation, the charge density at the edge of the drain electrode is equal to zero, and the channel is therefore depleted. This pinch-off and saturation (post-pinch-off) region is sketched in Figure 2.17 (c). Increasing the drain voltage beyond this point causes the channel edge to move more and more close to the source end. Eventually, the drain current is said to be in the saturation region because the drain current does not increase with the drain voltage.

Now, it is time to talk about the device parameters. The carrier mobility influences the device performance through its frequency or time response in several ways. The ability for carrier transport is related with this carrier mobility. There are three types of mobility in TFTs, which are the effective, field effect, and saturation mobility. First, we need to define the drain conductance (g_d) and transconductance (g_m) as follow: [2]

$$g_d = \frac{dI_d}{dV_{ds}} \mid V_g = \text{constant}, \; g_m = \frac{dI_d}{dV_g} \mid V_{ds} = \text{constant} \qquad (2.4)$$

Using this derivative Equation (2.4), the effective mobility (μ_{eff}) at low V_{ds}, field-effect mobility (μ_{fet} or μ_{lin}) at low V_{ds}, and saturation mobility (μ_{sat}) at high V_{ds} can be calculated as: [2]

$$\mu_{eff} = \frac{g_d}{C_{ox}\frac{W}{L}(V_g - V_{th})}$$

$$\mu_{fet} \text{ or } \mu_{lin} = \frac{dI/dV_g}{C_{ox}\frac{W}{L}V_{ds}} \tag{2.5}$$

$$\mu_{sat} = \frac{\left(\frac{d\sqrt{I_D}}{dV_g}\right)^2}{\frac{W}{2L}C_{ox}}$$

where L, W, and C_{ox} is the gate length, gate width, and gate oxide capacitance per unit area, respectively. Each one has its own advantages and disadvantages. For example, the value of V_{th} needs to be calculated for μ_{eff}, and this effective mobility is more susceptible to contact resistance due to low V_d. On the other hand, μ_{fet}, and μ_{sat} can be easily determined by the derivative of transfer curves without V_{th}. So, these are widely used for the device mobility. Usually, the saturation mobility is lower than μ_{eff}, because the dependence of the gate voltage is not considered when calculating the saturation mobility in Equation (2.5).

On/off current ratio is simply defined as the ratio of maximum to minimum I_D. The minimum drain current is sometimes taken by the gate leakage current. The turn-on voltage (V_{on}) corresponds to the V_G at which the drain current starts to increase as shown in a log I_D-V_G plot (Figure 2.18).

The threshold voltage (V_{th}) corresponds to the V_G at which an electron accumulation layer occurred at the semiconductor/dielectric interface. V_{th} can be obtained by a linear extrapolation of the I_D-V_G plot for low V_D or of the $I_D^{1/2}$-V_G plot for high V_D. Subthreshold voltage swing (SS) is defined as the inverse of the maximum slope in the transfer curve of a log ID-Vg plot. It means the necessary V_G to increase I_D by one decade: [2]

$$SS = \left(\frac{\mathrm{dlog}\,(I_D)}{\mathrm{d}V_g}\Big|_{\max}\right)^{-1} \tag{2.6}$$

Sometimes, the concept of hysteresis is used to determine the TFT stability, especially at the channel-insulator interface. This can be measured by positive and negative sweep at the same V_D (also called double sweep). If there is a shift of V_{on}, it corresponds to the evidence for electron trapping at or near the channel-insulator interface as an instability mechanism. Most of these device parameters are summarized in Figure 2.18.

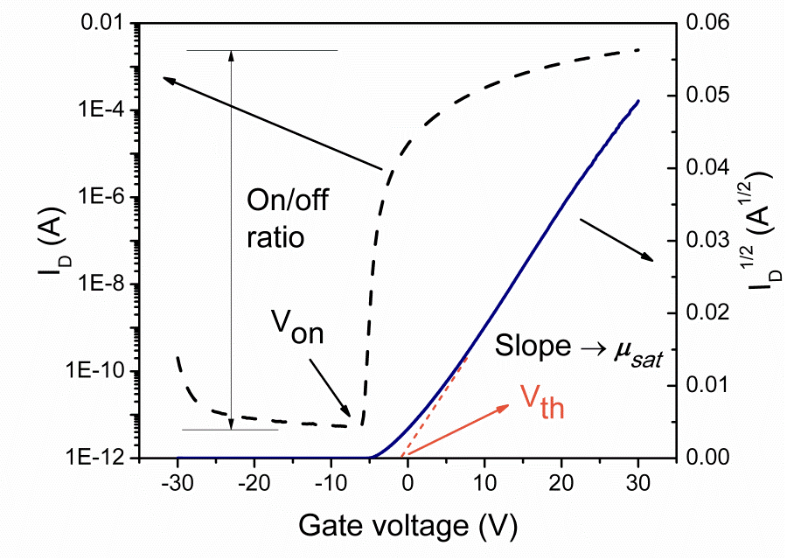

Figure 2.18. Typical transfer characteristics of a n-channel type TFT

2.6 Photo-Excited Charge Collection Spectroscopy (PECCS)

As mentioned in the introduction part, the defect states at or near the channel/dielectric interface can severely influence the performance of metal oxide TFT device under light and/or bias stresses. Hence, the analysis of electrical defect density-of-states (DOS) for a working metal oxide TFT device is very important. The photo-excited charge collection spectroscopy (PECCS) is a non-destructive method to measure the deep-level defects in wide band-gap semiconductors. [51] The direct measurement of deep-level density of defect states is possible at or near the channel/dielectric interface of a working TFT by measuring the threshold voltage shift (ΔV_{th}) under the monochromatic light. This magnitude of the photo-induced ΔV_{th} by scanning over the photon energy (ε), can be translated to the DOS distribution of defects in metal oxide materials by Equation (2.7). The interface charges trapped in certain energy level are excited into the conduction band by photon energy and collected at source/drain electrodes. During this process, the threshold voltage is shifted due to the photo-excited charges as shown in Figure 2.19. This change of photo-induced threshold voltage provides us with a direct measure of sub-gap defect DOS profile in the channel/dielectric interface.

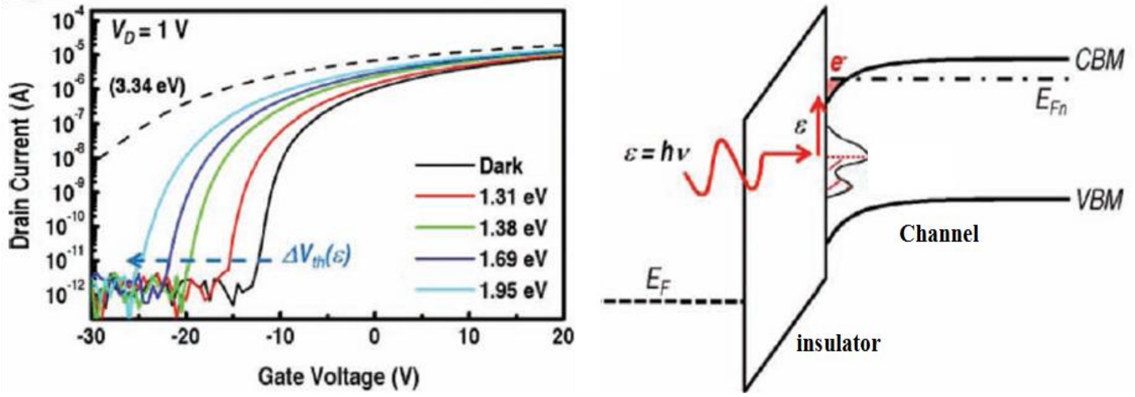

Figure 2.19. Photo-induced transfer curves in a n-channel TFT, and energy band diagram for the photo-excitation of trap charges in a certain energy level. The remaining trap electron charges at the interface are represented by the red shade. Reproduced with Ref. [51].

When photons shine with a specific energy (ε), most of trap charges within sub-gap states between (CBM– ε) and CBM would be excited into the conduction band minimum, since the photon flux of at least 0.2 mW cm^{-2} (6.0×10^{14} cm^{-2}s^{-1}) is enough to excite trap states, which is at most about order of 10^{12} –10^{13} cm^{-2}. The defect DOS can be determined by Equation (2.7). Therefore, the defect DOS is directly extracted from the shift of photo-induced V_{th}:

$$\mathrm{DOS}\ (\mathrm{CBM} - \varepsilon) = \frac{C_{ox}}{q}\frac{dV_{th}\ (\varepsilon)}{d\varepsilon} \tag{2.7}$$

where C_{ox}, q, V_{th}, and ε represent the dielectric capacitance per unit area (F·cm^{-2}), the electronic charge ($q < 0$), the photo-induced threshold voltage (V), and the photon energy (eV), respectively. The unit of defect DOS is cm^{-2} eV^{-1} with respect to CBM for n-channel. One of the most challenges in this PECCS technique is how to differentiate the interface defect from the bulk defects within the channel layer. If our TFT devices with 50 nm-thick channels show quite a density of bulk traps, their SS, and I_{off} values should also change significantly because an effective channel layer thickness is at most 5 nm (Debye length) from the interface. However, little change was observed and this confirms that our interfacial DOS estimation is valid.

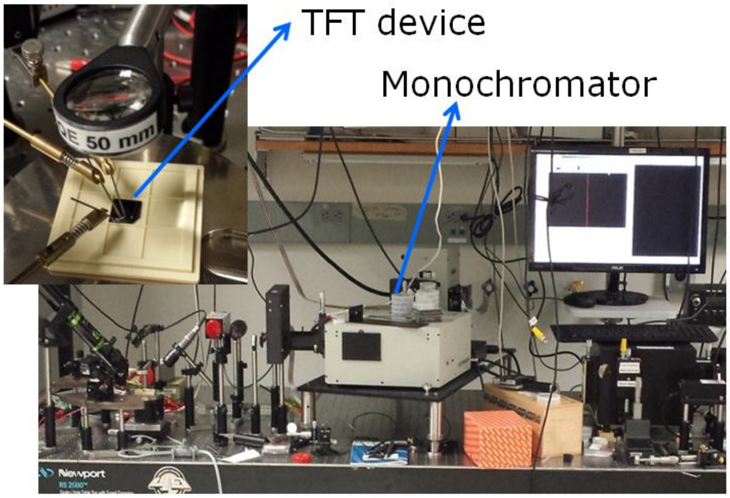

Figure 2.20. The schematic of PECCS measurement system

The schematic full measurement system of PECCS is shown in Figure 2.20: a 200 W quartz-tungsten-halogen light source, a grating monochromator covering from 800 to 300 nm, and a focusing lens which guide photons onto the TFT device, and the electrical measurement system (Agilent 4155C semiconductor parameter analyzer) in a dark. The optical power intensity of the monochromatic light can be measured by a power meter.

The most important part is how to produce monochromatic light with even optical power onto the TFT channel layer. This means that the key optical system is the grating system (Figure 2.21). The photo-induced transfer curve needs to be measured with a very low drain voltage (V_D) of 0.1 V, to minimize the measurement error due to the large drain electric field. We first applied sufficient positive gate bias to fill the defect states prior to the photon excitation process, where the wavelength was varied from 800 to 300 nm in 50 nm steps. Gate bias sweep started from the channel accumulation state ($+V_g$), because we should initially fill up all the interface trap states with charge carriers prior to the photo-excitation process. The full details of experimental method will be mentioned in the following experimental part.

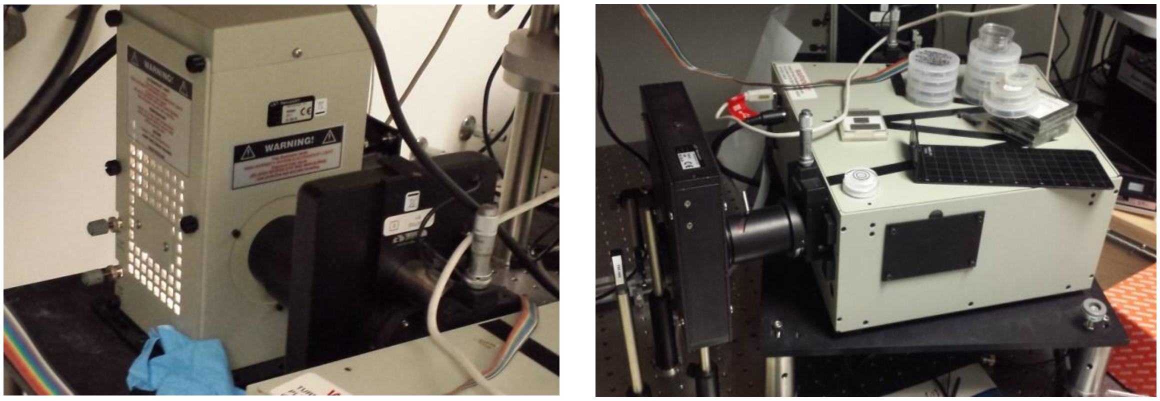

Figure 2.21. The key optical system in PECCS measurement: quartz-tungsten-halogen light source (left-side), and a grating monochromator (right-side)

2.7 Instability with Defect States & Persistent Photo-Current (PPC)

This part will mention the effect of defect states on the device performance and stability of metal-oxide TFTs. The defect states are the key factor for the high mobility and bias/photo-stress instability of the TFTs. In general, the performance of metal-oxide TFTs depends on the sputter growth conditions, such as RF power, oxygen or nitrogen flow pressure, chamber working pressure, growth temperature and so on. [101]

On the other hand, the bias/photo-stress instability of metal-oxide TFTs has to be also understood since the practical driving condition of TFTs are under gate bias, or light stress. Among these stresses, negative gate bias illumination stress (NBIS) is the most severe one. [102] In this part, the light stress instability mechanism will be first mentioned. Then, we will go into details about the bias stress and NBIS instability, following the persistent photo-current (PPC) mechanism, which severely degrades the response time of metal-oxide TFTs. Finally, the stability of metal-oxide TFTs was found to be affected by the defect states within metal-oxide semiconductor bandgap or at the interface between channel and dielectric layer.

First, it is well known that the threshold voltage (V_{th}) shift after the positive or negative bias stress is directly proportional to the trapping states in the bulk channel region or at the channel/dielectric interface region of the TFTs. [103-105] Trapped electrons at the interface or within the channel layer have been accepted as a possible reason for the positive V_{th} shift (less conductive) under the positive bias stress (PBS). On the contrary, explanation is possible for the negative bias stress (NBS), resulting in the negative V_{th} shift of transfer curve, as shown in Figure 2.22. The initial state can be recovered (or detrapped) after some hours without any annealing procedure. This means that the trapped charges at or near the interface is the reason of device instability under bias stress, rather than defect creation or ion drift. However, it is difficult to distinguish the effect of trapped and created defects under PBS or NBS conditions, since their degradation behavior is the same in the transfer curves.

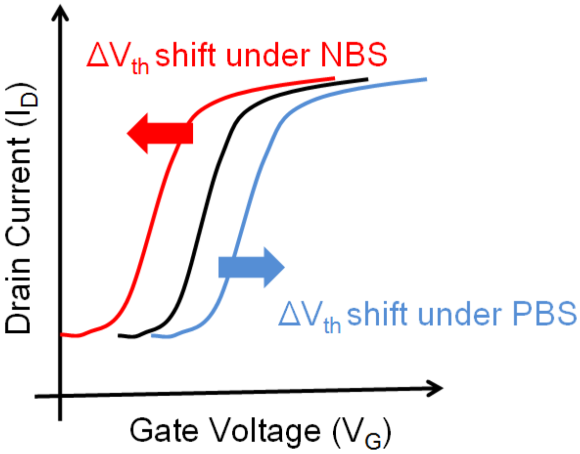

Figure 2.22. Instability of metal-oxide TFTs under PBS and NBS.

Now, the V_{th} instability under the illumination stress will be discussed in detail. The stability of metal-oxide TFTs against light exposure should be guaranteed for the application of transparent electronics. However, experimental data of metal-oxide TFTs are affected intensively under the illumination of light. The instability mechanism under light can be explained by the photo excitation/generation of trapped charges within the band gap of metal-oxide materials. The presence of some sub-gap defect states within the band gap must have induced the photo-excited charges into the conduction band under light. These increased photo-excited carrier generation from the sub-gap states to the conduction band contributed to the negative shift of V_{th}, although the photon energy was smaller than the band-gap energy. [30, 106, 107] This photo excitation/generation processes cause the negative shift of V_{th} and increase the photo-leakage current under the visible light (Figure 2.23). It is believed that the most sub-gap defect states are related with oxygen vacancy or oxygen deficiency. They become a shallow singly or doubly-ionized donor states from deep-level neutral states under light stress, as shown in Figure 2.23. On other words, the light-induced charge state transition from V_o to V_o^+, or V_o^{2+} is occurred under illumination stress within the band gap of metal-oxide materials. [27, 29, 36]

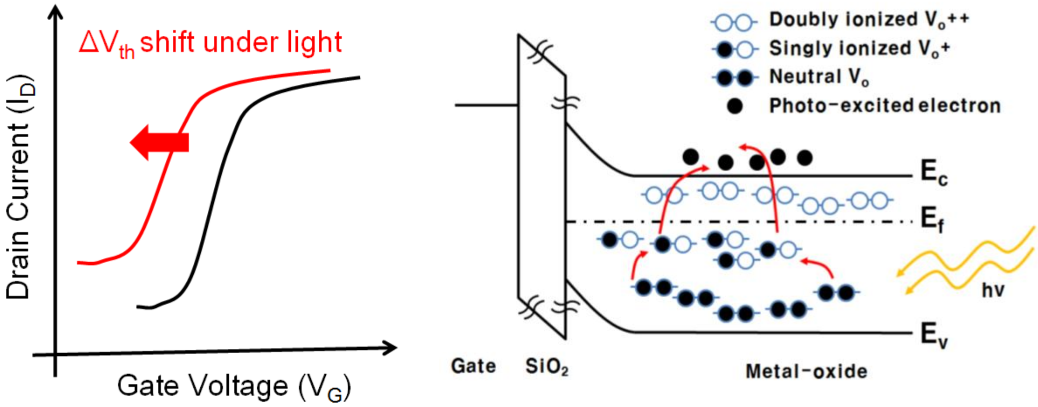

Figure 2.23. Instability of metal-oxide TFTs under illumination stress. (left: transfer curve under light, right: band diagram of sputtered ZnO TFT under light)

The photo-bias reliability of metal-oxide TFTs, especially under negative bias illumination stress (NBIS) remains a critical issue. Most time of the driving gate voltage of TFTs in display is the turn-off time at negative gate voltage (e.g. -5 V) under illumination from a back light unit or light-emitting diode. [1] Therefore, the negative shift of V_{th} under NBIS is much more stringent than other conditions. Actually, the defect states in the forbidden band gap play an important role on the instability of metal-oxide TFTs under NBIS condition. This defect can be an oxygen vacancy, zinc interstitial, or any other complex. The physical origin of NBIS instability is still unclear, and the following mechanism can be discussed in detail, as shown in Figure 2.24. One possibility is the generation of trapped charges at/near the interface or hole trapping into a gate dielectric under the negative bias voltage, which is shown at the left side of Figure 2.24. [103, 105, 108]

Another possibility is the creation of photo-excited charges or the donor-like defects (e.g. ionized oxygen vacancy) under light from the sub-gap defect states within the active channel thin-film, as shown at the right side of Figure 2.24. [106, 109, 110] Both mechanisms are believed to contribute to the significant change of V_{th} shift under NBIS condition. This means that the donor-like defect generation under NBIS induced the significant negative V_{th} shift together with positive charge (hole) trapping at/near the interface. [1, 23, 36, 111-113] However, no direct evidence has been provided for NBIS degradation mechanism.

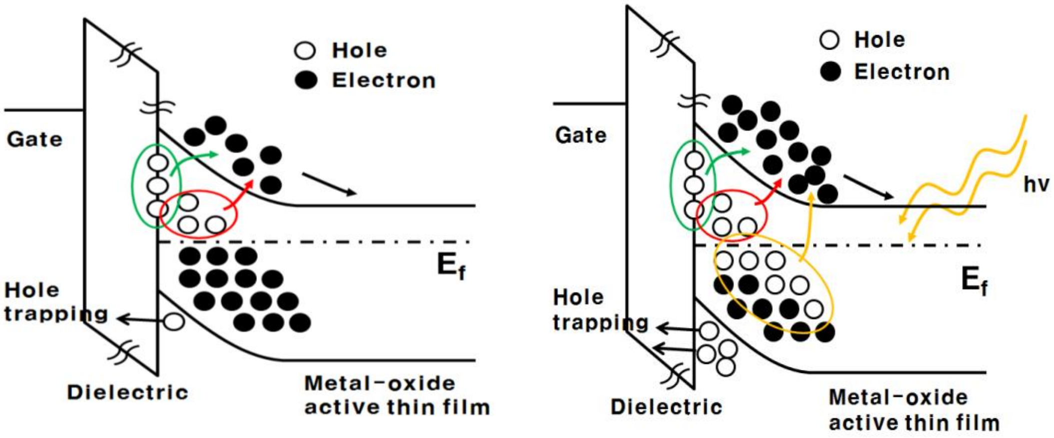

Figure 2.24. Energy band diagram illustrating (left) the NBS- and (right) the NBIS-induced instability of metal-oxide TFTs.

As mentioned in this section, trapped charges at/near the interface, hole trapping into a dielectric, and the generation of photo-excited charges are generally accepted as the origins for the NBIS instability. Recently, researchers are trying to improve the stability of metal-oxide TFTs under NBIS condition. Several methods have been examined to suppress this instability. The first approach is by using Al_2O_3 films as a gate layer for hole carrier blocking layer to effectively minimize the NBIS instability. [114] Similar superior reliability was also investigated with thermal-oxidized TiO_2-gated ZTO TFTs. [34] However, generally speaking, the V_{th} shift caused by the hole trapping or trapped charges at the interface is believed to be relatively small compared to that by the photo-excited charges from the sub-gap defects.

Another way to improve the NBIS stability without the degradation of device performance is the use of double layer structure TFT for the channel. The VZTO/ZTO bilayer channel structure exhibited much better stability than the single ZTO layer TFT. [115] In this paper, it was found that the improved stability was observed due to the reduction of donor-like states that can be ionized by visible light. Therefore, reduction of defect density within the metal-oxide film is substantially important for the improvement of NBIS stability. It is known that the most defect states are related with oxygen deficiency, so the degree of photo-ionization is proportional to the concentration of pre-existing oxygen vacancy in the channel layer itself. For example, high pressure post-annealing [116], high oxygen pressure during sputtering growth [117], oxygen-containing plasma treatment [118], and an ozone treatment [119] can be applied to supply enough oxygen species, which resulting in the reduction of oxygen-related defect centers, and leading to the improvement of NBIS stability. Unfortunately, reducing the oxygen vacancy in multi-component metal-oxide remains a challenge because of the high density-of-states (DOS) of defects without a degradation of the device performance.

One of the challenge problems of metal-oxide semiconductor materials is the persistent photoconductivity (PPC) after illumination has been removed. [27, 109, 110] This PPC behavior degrades the response time and frame rate of oxide-based sensor or TFT arrays. This PPC behavior in ZnO-based materials can be explained by the photo-ionization of oxygen vacancy sites within the bandgap. [27, 30] So, increasing photo-generated oxygen vacancy sites can enhance the PPC by liberating more electrons. They suggest that the oxygen vacancy is deep and does not contribute to the intrinsic n-type conductivity in thermal equilibrium. However, metastable shallow donor state of oxygen vacancy (so called, ionized oxygen vacancy, V_O^+, V_O^{2+}) can contribute to the channel conductivity under illumination. [27, 29]

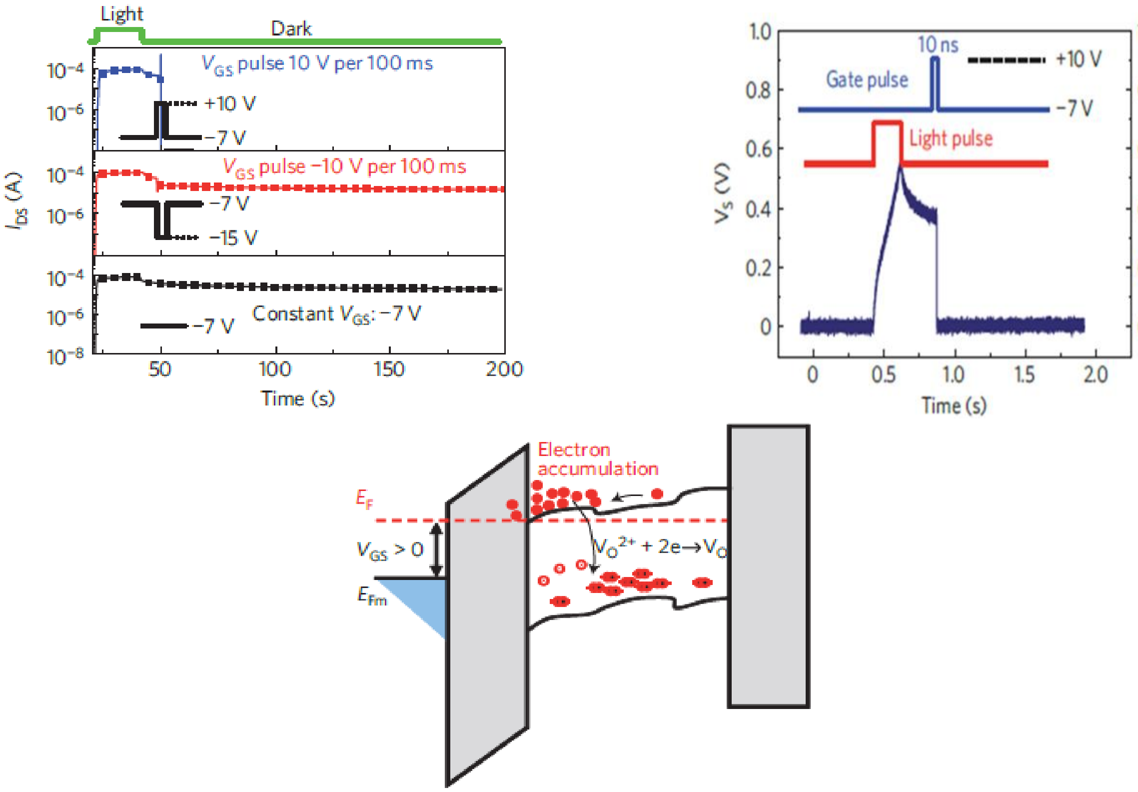

Figure 2.25. Drain-source current under light with gate bias pulses (top). Applying a positive gate voltage is effective to overcome the effects of PPC. Schematic band diagram of the positive-bias-assisted PPC recovery mechanism (bottom). Reproduced with Ref. [28].

The presence of an energy barrier between the neutral and the ionized oxygen vacancy states due to the large lattice relaxation can hinder the recovery process for electrons to be captured back into the defect states, resulting in the PPC behavior. This barrier was estimated by first principle calculations for ZnO crystals to be 0.2 eV and 0.3 eV, respectively. [27, 29] The problem of PPC can be solved and controlled by applying a short-duration (10 ns) positive gate voltage pulse (10 V) to the device. [28] This method can derive electron accumulation within the channel and fill up ionized oxygen vacancy states with electrons, and hence enhance the recovery process from PPC behavior, as shown in Figure 2.25.

2.8 Previous Researches on Metal Oxide TFT Stability and Defect States

Recently, solution-processed ultra-thin (3 nm) zinc-tin oxide (ZTO) TFT was examined under various photo/bias stress conditions by Li-Chih Liu *et. al*.. [120] It is found that the ΔV_{th} is shifted positively under PBS or positive bias illumination stress (PBIS), but the ΔV_{th} is significantly shifted negatively under NBIS. They suggested that the photo-ionized oxygen vacancies generated the extra charges, which interacted with the applied bias and induced the shift of transfer curves under NBIS. Therefore, oxygen vacancies within metal-oxide materials' band gap affected the stability of channel layer under NBIS condition. The transfer curves under various conditions are plotted on Figure 2.26. [120]

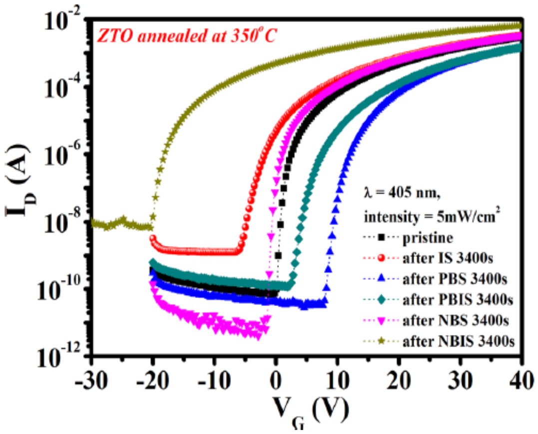

Figure 2.26. Transfer curves for ZTO TFTs under PBS, NBS with and without light illumination at a stress time of 3400 s. Reproduced with Ref. [120].

The NBIS instability of a-ITZO TFTs were also quantitatively examined by the extracted defect DOS and the device simulation by Jaeman Jang *et.al*.. [32] The effect of equivalent oxide thickness (EOT) of gate insulator on the NBIS instability showed that the instability mechanism is contributed to the donor creation, rather than the charge trapping at the interface or into the gate dielectric. In this letter, it was believed that the donor creation is attributed to the ionized oxygen vacancy (V_O^{2+}, V_O^{1+}) or peroxide O_2^{2-} with the increase of EOT, which could be explained by more prominent oxygen deficiency.

It was also found that the oxygen vacancy-related factor accounts for about 90% of the total donor creation taking place in the valence band tail states. In the previous part 2.7, positive-bias-assisted PPC recovery mechanism was mentioned to slow PPC behavior of an oxide TFT. Another way to deactivate the oxygen vacancy sites is by substituting oxygen with nitrogen in ZnO-based oxide materials during a sputtering growth. [121] The a-IGZO:N TFT showed a 44% increase in the mobility and better reliability by reducing the oxygen absorption/desorption reaction to the atmosphere. [122] Nitrogenated metal-oxide TFTs showed the enhanced illumination stability, and improved PPC recovery behavior by reducing the oxygen-deficiency related defect states, as shown in Figure 2.27.

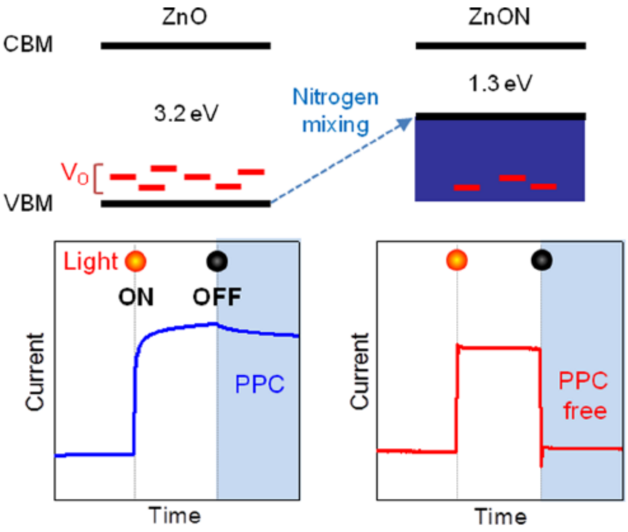

Figure 2.27. Schematic band diagram of ZnO (optical band gap = 3.2 eV) and ZnON (optical band gap = 1.3 eV). The persistent photocurrent (PPC) under negative bias is attributed to the deep donor-like oxygen vacancy under light (left side). On the other hand, nitrogen with higher p orbital energy than the oxygen could reduce the oxygen vacancy, resulting in the increase of valence band maximum (VBM) energy level (right side)

2.9 Characterization of metal-oxide films: X-Ray Diffraction (XRD)

The structural properties were studied by X-Ray diffraction (XRD). XRD is a preferred technique in determining lattice constant, and grain size since the wavelength of x-ray radiation is on the order of the interatomic spacing of crystalline structures. When an x-ray beam is incident on a crystalline structure, diffraction occurs when the following condition is satisfied, known as Bragg’s Law: [123]

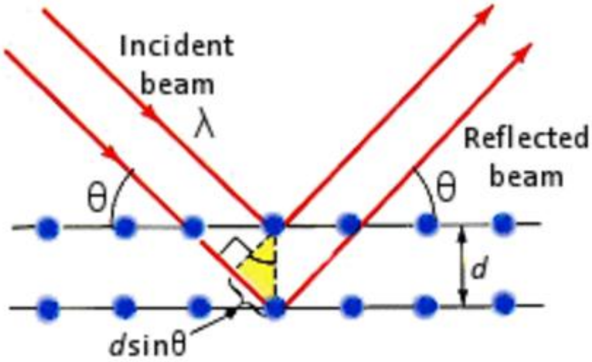

Figure 2.28. Schematic illustration of scattered X-ray beams in the atomic arrangement.

$$n\lambda = 2d\sin\theta \tag{2.8}$$

where n is the order of diffraction (normally taken to be 1), λ is the wavelength of x-ray radiation, θ is the angle between the incident beam and the sample, and d is the interplanar spacing of the material. The scattered or reflected X-rays from the sample interfere with each other either constructively or destructively due to a different optical path length to travel. The magnitude of this path length depends on the distance between the crystal planes (d) and the incident angle of the X-ray beam (θ). Constructive interference occurs only if the path difference is a multiple of the used wavelength of the X-ray beams. Therefore, knowing the wavelength of x-ray radiation as well as θ to high precision, the use of the Bragg equation (2.8) allows determining the distance (d) between the crystal planes, providing insight into the material's lattice parameter.

The average dimensions of crystallites (grain size, D) are also determined by the Scherrer method (Equation 2.9) from the broadening of the diffraction peaks at half the maximum intensity, expressed as a full width at half maximum (FWHM): [123]

$$D = \frac{K\lambda}{\beta \cos \theta} \tag{2.9}$$

where K is a dimensionless shape factor, with a value close to unity, a typical value of about 0.9 for hexagonal unit cell, β is the peak broadening (FWHM, radian), θ is the Bragg angle (angle). FWHM is measured by a rocking curve, which is a plot of X-ray intensity vs. omega (ω, angle between the X-ray source and the sample). Not only the peak position in a ω-2θ scan contains valuable information on the materials, the FWHM of the diffraction peak contains information on the crystalline particle size as well. In case of a perfect crystal, the crystal size in the Scherrer formula will be related to the thickness. The FWHM of the rocking curve is also an important indicator of the material crystalline quality of the preferred orientation. For example, a narrow rocking curve FWHM is an indication of good epitaxial alignment on the substrate.

2.10 Characterization of metal-oxide films: X-Ray Reflectivity (XRR)

XRR measurements were carried out to analyze the density, thickness and roughness of multilayer thin films. [124] This is because most properties of thin films are thickness and density dependent. XRR is a non-contact technique for thickness determination between 2–200 nm with a high precision (1–3 Å). XRR method involves monitoring the intensity of a monochromatic x-ray beam reflected by a sample at grazing angles (0–2°), and the reflected intensity is recorded by a detector. Instead of constructive interference of scattered X-rays from different lattice planes, the scattered beam is characterized by fractional reflection of the beam from the surface and each interface by the differences in the electronic density of the materials, as shown in Figure 2.29.

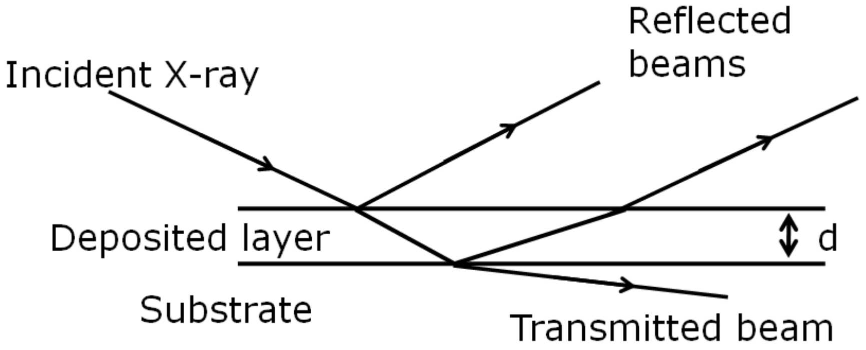

Figure 2.29. Reflection of X-rays under grazing incidence from a single layer on a substrate

The mode of operation is θ /2θ mode which makes sure the incident angle is always half of the angle of diffraction, which is called specular reflection. The specular reflection at the surface and interfaces is due to the different electron densities in the different layers, which corresponds to different reflective indexes in the classical optics. For incident angles θ below a critical angle θ_c, total external reflection occurs. The entire incident beam is totally reflected at the film surface. The critical angle for most materials is less than 0.3°. At X-ray frequencies, the polarizability of the film is directly correlated with the electronic density which is proportional to the mass density, so the critical angle is a function of the mass density. Therefore, the density of the material is determined from the critical angle.

Above θ_c the reflection from the different interfaces interferes and gives rise to interference fringes. The period of the interference fringes and the fall in the intensity are related to the thickness and the roughness of the layers. From the decay of the intensity above θ_c information about the interface roughness can also be deduced. Roughness gives rise to diffuse scattering, resulting to a less intensity in the specularly reflected beam. Roughness decreases the reflected intensity dramatically. The thickness is related to the interference fringe period of the oscillations. The thickness is inversely proportional to the period of oscillations. The reflection can be analyzed using the classical theory (Fresnel equation). If the interface is not sharp and smooth, then the reflected intensity will deviate from that predicted by the law of Fresnel reflectivity. More information could be found in the reference. [124] Most of these parameters are summarized in Figure 2.30 with typical XRR pattern.

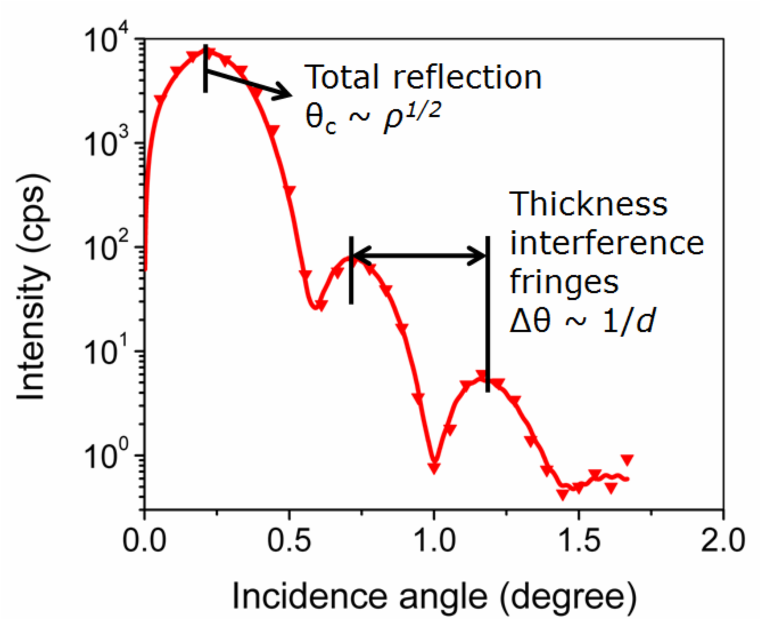

Figure 2.30. Typical X-ray reflectivity pattern. Sputtered ZnO with 9 nm thick on top of a SiO_2/p^{++}-Si wafer. (*ρ*: density, *d*: thickness)

2.11 Characterization of metal-oxide films: X-Ray Photoelectron Spectroscopy (XPS)

X-ray Photoelectron Spectroscopy (XPS) is an analytical method used for analyzes of the chemical composition, electronic state of surfaces, and is based on photon-electron interactions. [125] XPS measurement is based on the absorption of X-ray photon energy and following emission of an electron, which is called the photoelectric effect. The electron emitted in this manner is called photoelectron. The energies of photons are usually in the order of 1 keV or higher. These photons penetrate into the material and interact with electrons situated in the inner shells of atoms, as shown in Figure 2.31. The energy of the electrons emitted from the inner shells is then analyzed by the electron spectrometer. A photoelectron spectrum is obtained as a plot with the number of detected electrons per energy intensity versus their kinetic energy.

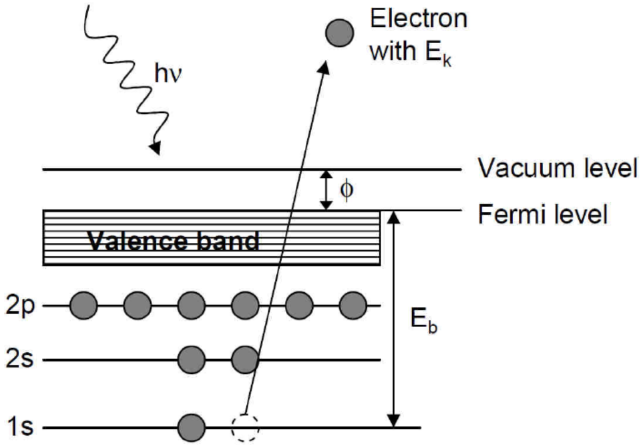

Figure 2.31. Schematic diagram of the photoelectron emission.

To conserve the energy of emitted electrons and to attain sufficient long mean free path in the vacuum chamber, XPS measurements have to be carried out under ultrahigh vacuum conditions. The emitted electrons escape only from the close vicinity of the sample surface (< 5–10 nm). Therefore, information about the chemical composition is obtained only from the depth of a few nanometers. For the incident photon with a particular energy, the interaction equation can be written using the energy conservation principle as:

$$h\nu = \mathrm{E_k} + \mathrm{E_b} + \Phi \tag{2.10}$$

where h denotes Planck constant, ν is the photon frequency, E_k represents photoelectron kinetic energy after emission, E_b is the binding energy, and finally Φ is the work function of the sample. The binding energy is then defined as the energy required to eject an electron from the inner shell to infinity with a zero kinetic energy. Binding energies are relative to a reference level, which is usually the Fermi level. In the practical application, it is inconvenient to use the work function of the sample since for each sample the work function has a specific value. Therefore, the sample is conductively connected to the analyzer, whose work function is fixed, and the kinetic energy is measured according to the vacuum level of the analyzer. Photons with energies of ~1 keV are sufficient to eject inner shell electrons from atoms with a small atomic number. However, for atoms with atomic number $Z > 30$ only electrons from the outer electron shells are emitted. In addition, the XPS peak intensity and shape at the particular energy provide the quantitative density of elements, as well as their chemical states.

The electrons leaving the sample are analyzed by an electron spectrometer according to the distribution of their kinetic energy. The analyzer is usually operated as an energy window (varying with the pass energy), which accepts only those electrons having energy within the range of this window. To maintain a constant energy resolution, the pass energy is fixed. Incoming electrons are adjusted to the pass energy before entering the energy analyzer. Scanning for different energies is accomplished by applying a variable electrostatic field (electronic lenses) before the energy analyzer. Electrons are detected as discrete events, and the number of electrons for a given detection time and a given energy is stored by the software and after a sweep of the electrons with all different energies in a desired energy range, the stored data are displayed as final spectrum.

In our work, XPS was used for chemical composition, stoichiometry, and defect analysis of sputtered ZnO or Indium-Tin-Zinc-Oxide (ITZO) thin films. The chemical analysis was performed by monochromatic Al K alpha x-rays with an energy of 1486.6 eV. The system also includes argon ion gun, which was used for surface cleaning to remove contaminants. XPS spectra were measured at ambient temperature. To minimize the charging effect, a low-energy electron gun was used for charge neutralization. The carbon 1s line (for hydrocarbon, binding energy 284.8 eV) was used to calibrate the binding energy scale of the XPS measurements. For example, the XPS spectrum of sputtered ITZO film is shown in Figure 2.32. The atomic concentration percentage is calculated by dividing the element peak intensity by the relatively sensitivity factor (RSF) and then normalized over all of the elements detected.

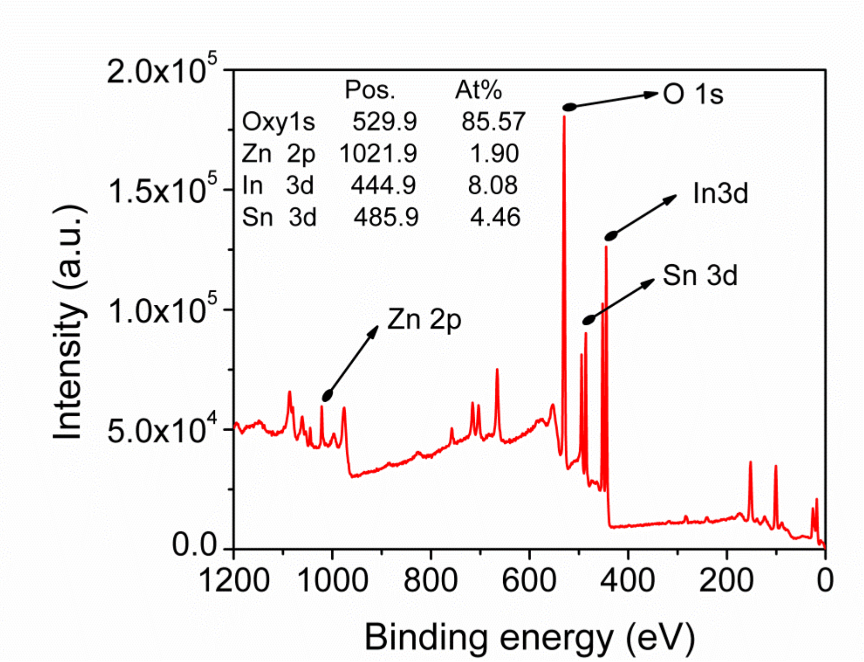

Figure 2.32. XPS spectrum of sputtered Indium-Tin-Zinc-Oxide (ITZO) on top of a SiO_2/p^{++}-Si wafer with quantitative analysis.

2.12 Characterization of metal-oxide films: Scanning Electron Microscopy (SEM)

Scanning electron microscopy (SEM) is a microscopic method, which is based on the interaction of focused electron beam with sample. Primarily electrons are emitted from an electron gun, focused by an electromagnetic lens and directed on the sample. During this interaction process, many types of signals are generated and these signals can be displayed as an image. Secondary electrons (SE), Auger electrons, backscattered electrons (BSE), and X-ray radiation can be detected and used for materials contrast and chemical composition investigations, respectively, as shown in Figure 2.33.

Among these signals, two signals most often used to generate SEM images are SE and BSE. Some electrons are scattered in-elastically due to the loss in kinetic energy upon their interaction. These loosely bound electrons from the surface can be knocked off by incident electrons. These are secondary electrons and widely used for SEM topographical imaging. Electrons captured by the scintillator/photomultiplier are then amplified and used to form an image in the SEM. [126]

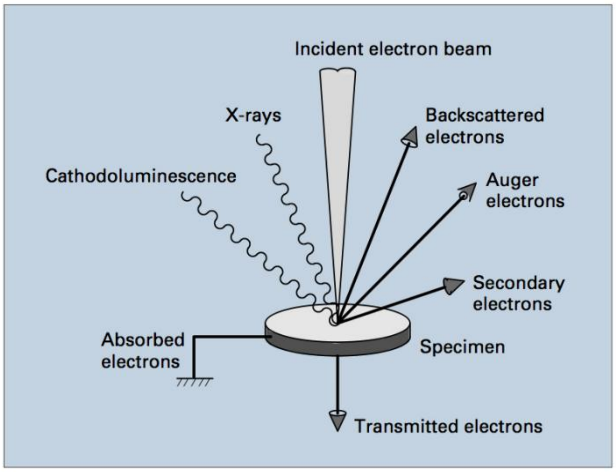

Figure 2.33. Electron beam and specimen interaction in SEM.

While the smallest details that can be distinguished in a light microscope are about 200 nm in size, a modern SEM can have a resolution of 0.2 nm. Since the naked human eye can differentiate features 0.2 mm in size or larger, the optical microscope is therefore useful for magnification of 1000x whereas the SEM can provide up to 1000,000x magnification.

A scanning electron microscope, presented in Figure 2.34 is composed of a gun that generates electrons either through thermionic or field emission from tungsten or Lanthanum hexaboride (LaB_6) thermionic emitters. The beam is then accelerated in an electric field with potentials between 200 V–30 kV. So, the electron gun generates electrons and accelerates them to energy in the range up to 30 keV towards the sample to a depth of approximately 1 µm. A system of magnetic lenses focuses the beam, and scanning coils raster the beam across the specimen surface. Secondary electrons that were in-elastically scattered by the specimen are detected and amplified to produce an image of the sample surface morphology. The FEI Nova 230 Nano SEM tool was used to characterize the samples in this study.

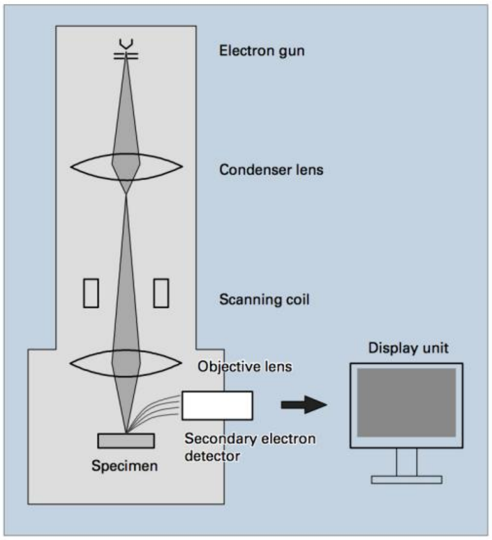

Figure 2.34. Diagram showing the various components of a SEM.

In this work, SEM was used to study the microstructure of sputtered ZnO film on the substrate as a function of oxygen ratio during sputtering growth. As a part of the thesis, the surface morphology and grain size was visualized under SEM to confirm the reduction of grain size with increased oxygen ratio.

Chapter 3. Experiment: Fabrication & Characterization

3.1 ZnO Schottky Diode Fabrication

The sample was a commercial n-type bulk single crystal of ZnO obtained from University wafer Inc. grown by hydrothermal method. The sample was the size of 10×10×5 mm^3 with the (0001) Zn face up. The room temperature carrier concentration, carrier mobility, and resistivity were 0.86×10^{17} cm^{-3}, 91.9 $cm^2V^{-1}s^{-1}$, and 0.85 Ωcm, respectively, from Hall effect measurement using the van der Pauw geometry. The front surface was only polished for the surface roughness about 1~2 nm. The sample was first cleaned in an ultrasonic bath with acetone, Isopropyl Alcohol (IPA) and de-ionized (DI) H_2O. Before the metallization, the sample was put into the boiling 30% H_2O_2 for 3 min to improve the quality of Schottky contact and dried again with N_2 gas.

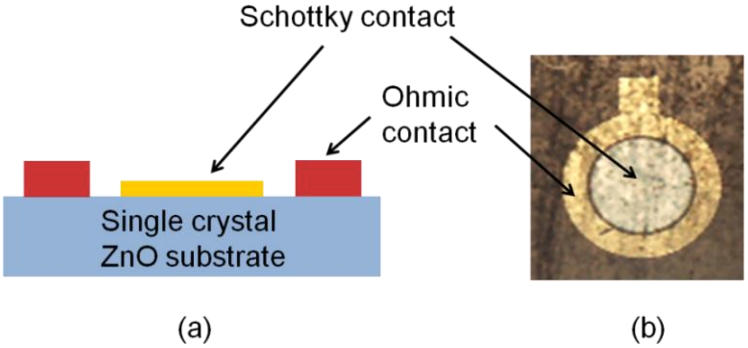

Figure 3.1. Simplified schematic illustration of the Pd/ZnO Schottky Barrier Diode (SBD).

As shown in Figure 3.1, Annular Ohmic contacts (inside diameter = 550 μm, outside diameter = 800 μm) were first prepared on the polished Zn-polar face by using electron-beam evaporation. Ti/Al/Pt/Au (20/80/40/80 nm) was deposited with a base pressure of ~10^{-6} mbar and lift-off photolithography. Then, the sample was annealed at 200℃ for 1 min under N_2

atmosphere. For the Schottky contacts, Pd (60 nm) was deposited inside on the same surface with a diameter 450 nm via electron-beam evaporation and lift-off photolithography. The Schottky contact area was 1.59×10^{-3} cm^2.

3.2 Characterization of ZnO Schottky Diode

3.2.1 Current-Voltage (IV) / Capacitance-Voltage (CV) Measurement

The I-V data was acquired in darkness at room temperature by an Agilent 4156C Precision semiconductor parameter analyzer. The C-V measurement was performed by using an Agilent E4980A LCR meter. During the C-V characterization, a test signal of 50 mV with a probing frequency of 1MHz was used.

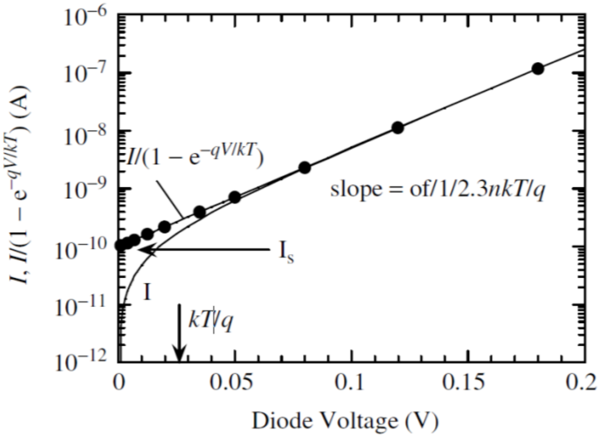

Figure 3.2. Two ways of plotting current-voltage for a Schottky diode. Reproduced from Ref. [83].

Figure 3.2 shows two ways of plotting current-voltage (I-V) for a Schottky diode. A clear rectifying behavior could be found for the Pd/ZnO Schottky barrier diode (SBD). The saturation current I_s of the diode is given by: [83]

$$I_s = AA^* T^2 \exp\left(\frac{-\emptyset_B}{kT}\right) \quad (3.1)$$

where A is the Schottky contact area, A^* the effective Richardson constant (theoretically A^* =32 A cm^{-2} K^{-2} for ZnO using $m^* = 0.27m_0$), and $\emptyset_B$ is the barrier height. The barrier height is most commonly calculated from the saturation current I_s at zero bias from equation (3.1), and I_s is determined by extrapolating the curve of ln[I/(1-exp(-qV/kT))] versus voltage under a forward bias up to V = 0 V in Figure 3.2; therefore, the barrier height is determined at a zero bias. By plotting the ln[I/(1-exp(-qV/kT))] versus V curve, the ideality factor n can be also found from the slope q/nkT of the curve. The data are usually linear all the way to V = 0. The values of n vary from almost n=1.0 under the reverse bias voltage and n starts to deviate significantly from 1 under forward bias condition indicating a rather strong dependence of the barrier height in the applied voltage.

The capacitance-voltage (C-V) characteristics could be measured at 1 MHz to evaluate the built-in potential (V_{bi}) and carrier concentration (N_d) using an Agilent E4980A LCR meter in dark conditions. An approximate evaluation of V_{bi} obtained essentially from the intercept of $1/C^2$ versus V plot on the V-axis as shown in Figure 3.3 and the N_d can be also found from the slope (a). The N_d is calculated by $2/(q\varepsilon\varepsilon_o a)$ where ε, and ε_o represent the static dielectric constant (8.5 for ZnO), and ε_o the vacuum permittivity, respectively. The Schottky barrier height is in turn obtained from the following equation (3.2): [83]

$$\emptyset_b = q\left[V_{bi} + \frac{kT}{q}\ln\left(\frac{N_c}{N_d}\right)\right] \quad (3.2)$$

where N_c is the effective density of states in the conduction band (2.94×10^{18} cm^{-3} using $N_c = 2(2\pi m^*KT/h^2)^{3/2}$).

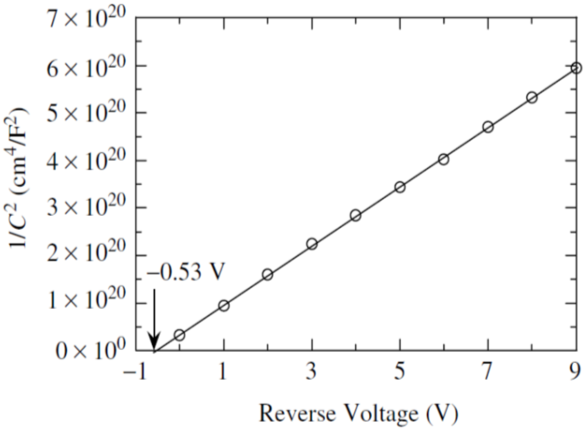

Figure 3.3. Reverse-bias $1/C^2$ versus voltage of the Schottky diode. Reproduced from Ref. [83].

3.2.2 DLTS Measurement

DLTS was measured and operated at a frequency of 1 MHz for the transient capacitance measurement, using a PhysTech FT1030 DLTS system and a liquid Nitrogen flow cryogenic probe station (Lakeshore TTPX) was combined with the DLTS system at temperatures between 77 and 340 K in Figure 3.4. The DLTS measurement was performed with a reverse bias voltage of -2.5 V and a positive pulse voltage of 0 V (filling pulse time = 50 ms).

The transient capacitance was measured within 40 ms at different temperatures. The maximum transient capacitances were extracted by using different emission rates (emission rate = $\ln(t_1/t_2)/(t_2-t_1)$, where t_1 and t_2 are the starting and end of time window), and the emission rate of 0.034, 0.042, 0.093, 0.423, and 0.888 ms^{-1} were selected. Finally, by using the Arrhenius plot, the defect energy level (E_t) and capture cross section (σ_n) could be obtained, as mentioned previously in Chapter 2.

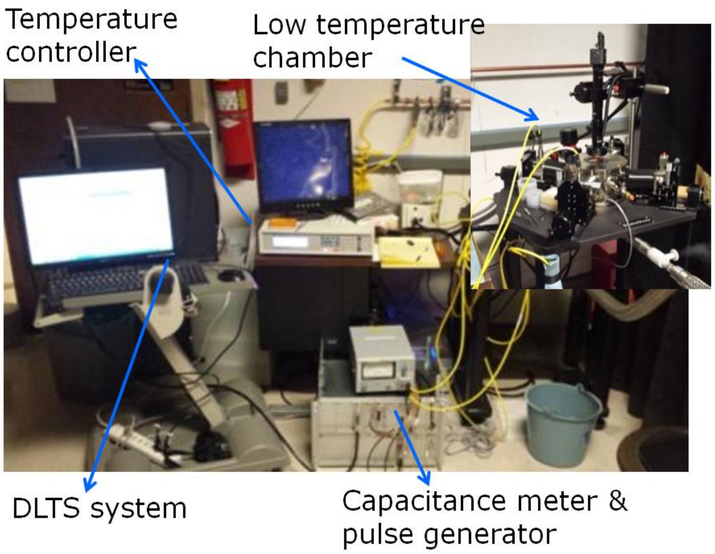

Figure 3.4. DLTS measurement set-up

3.3 ZnO TFT Fabrication

Our sputtered ZnO transistors were fabricated on a thermally grown 300 nm SiO_2 (as a bottom gate insulator) on top of a heavily boron-doped p-type Si substrate (0.001 – 0.005 Ω·cm). The SiO_2/Si substrates were sonicated with aceton, isopropyl alcohol (IPA), and de-ionized (DI) H_2O, sequentially. After cleaning, 70 nm-thin ZnO semiconductor film as an active channel layer was deposited by using RF magnetron sputtering with a metal shadow mask to define a channel area (1000 × 500 μm).

The sputtering power condition of 75 W (1.6 $W \cdot cm^{-2}$) was selected in order to investigate correlations between the oxygen partial pressure and transistor's electrical performance. The ZnO target (3 inch) from Kurt J. Lesker with a purity of 99.9 % was used under the working deposition pressure of 2 mTorr at room temperature. For each deposition, the target surface was cleaned by pre-sputtering for 10 min. Sputtering was carried out in a different oxygen flow rate (0, 2, 5, 10 sccm), while the argon flow rate is fixed at 15 sccm (oxygen ratio, $O_2/(O_2+Ar)$ = 0, 0.12, 0.25, and 0.40).

The ITO source and drain (S/D) electrode (thickness = 100 nm) was also patterned by RF magnetron sputtering through a metal shadow mask with a width of 1000 μm and a length of 150 μm (W/L). Samples (Figure 3.5) were annealed at 350°C for 1 hour under vacuum atmosphere to keep the atomic composition as deposited ZnO depending on the oxygen ratio. Finally, PMMA (495 A4) was spin-coated on top of the device at 4000 rpm for 45 s in air and pre-baked at 90°C for 10 min for the protection layer as a last process.

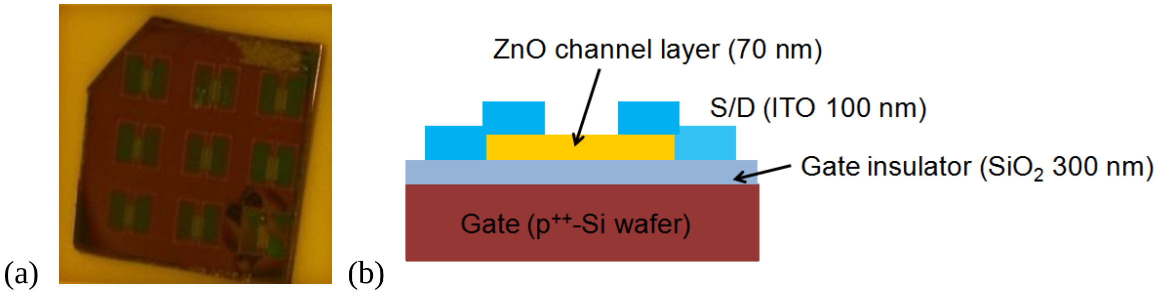

Figure 3.5. ZnO TFTs on top of a SiO_2/p^{++}-Si wafer ((a) top view, (b) cross section view).

3.4 Characterization of ZnO TFT

3.4.1 X-Ray Diffraction (XRD), X-Ray Reflectivity (XRR) & SEM

The sputtered ZnO film was also characterized with a X-ray diffractometer (XRD, Bede D1 diffractometer) with monochromatic Cu Kα (λ = 1.5405 Å) radiation source to investigate the grain size and crystallinity. Detailed peaks and full-width-half-maximum (FWHM) were discussed to examine the sputtered ZnO thin films. The X-ray reflectivity (XRR) was also performed using high intensity Bede D1 diffractometer to obtain the roughness between SiO_2 and ZnO, and density of sputtered ZnO. The XRR data was fitted by Jordan Valley REFS software. Finally, the surface morphology was observed by Nova 230 Nano Scanning Electron Microscopy (SEM). Their images will be shown in the result part at various oxygen ratios in order to reveal that the average surface grain size.

3.4.2 Bias Stress Test

The I_d-V_g measurement with a bias stress was performed by using a semiconductor parameter analyzer (Agilent 4155C) in the dark at room temperature. The positive bias stress test was carried out with gate bias of + 20 V at a fixed drain-source voltage (V_{ds}) of 5 V for time periods up to 5×10^3 s. The forward sweeping of V_g was applied from -30 to 30 V. First, a positive bias stress at a V_{ds} of 5 V was applied to ZnO TFT device in the dark during a specific stress time; eg. 0, 10, 100, 1000, or 5000 s. Immediately afterwards, we removed the bias stress and performed the I_d-V_g measurement.

3.4.3 PECCS Measurement with Sputtered ZnO TFT

The drain current (I_{ds})–gate voltage (V_{gs}) measurements were performed by positive (forward) sweep from -30 to 30 V in the dark at room temperature using an Agilent 4155C semiconductor parameter analyzer. Photo-induced I_{ds}-V_{gs} measurement system was prepared with a light source of 200 W Quartz-tungsten-halogen (QTH) lamp, a grating monochromator (Newport CS 260), and a focusing lens, as shown in Figure 3.6. The optical power intensity of monochromatic light was measured by the power meter (Newport Model 1936-R). We applied the monochromatic light onto the working TFTs to excite the trapped charges from 800 nm up to 300 nm in 50 nm step.

The photo-induced transfer curves were measured by sweeping the gate-source voltage (V_{gs}) from +30 to -30 at the V_{ds} of 0.1 V with monochromatic light. We applied sufficient positive bias to fill the defect states prior to the photon excitation process. From the photo-induced transfer curve, we collected the photo-shifted V_{th} for each monochromatic light to extract the density of states (DOS) within the sub-gap states of the working ZnO TFT as a function of the oxygen ratio.

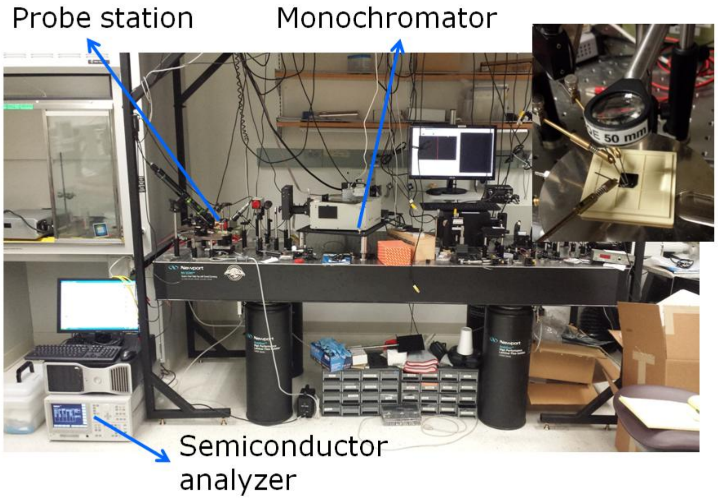

Figure 3.6. PECCS measurement set-up

3.4.4 X-Ray Photoelectron Spectroscopy (XPS)

All XPS spectra were obtained with AXIS Ultra DLD supplied by Kratos Analytical Ltd. The stoichiometry and defect analysis of the sputtered ZnO films were examined by using X-ray photoelectron spectroscopy (XPS) with a monochromatic Al (Kα) radiation source. The XPS spectra were obtained after Ar^+ cleaning. Wide survey scan spectra were obtained at a passing energy of 160 eV. Oxygen 1s, Zinc 2p, Indium 3d, and Tin 3d core level high resolution spectra were collected with a passing energy of 20 eV. CasaXPS software package was used for the curve fitting of core level peak.

3.5 Amorphous-Indium-Tin-Zinc-Oxide (a-ITZO) TFT Fabrication

Sputtered a-ITZO transistors were fabricated on top of a heavily boron-doped p-type Si substrate (0.001 – 0.005 Ω·cm) coated with 100 nm of thermally grown SiO_2 (bottom gate dielectric). The SiO_2/Si substrates were cleaned in an ultrasonic bath with aceton, isopropyl alcohol (IPA), and deionized H_2O each for 10 minutes, sequentially. ITZO films as a channel layer thickness of 7–9 nm were deposited by using RF magnetron sputtering. An active channel area was patterned with a wet-etch (diluted HCl 37 %) process through photolithography. A power of 100 W (power density of 1.2 $W \cdot cm^{-2}$) was fixed.

A 4 inch ITZO target (In_2O_3:ZnO:SnO_2 = 40:35:25 at%, Plasmaterials) was used with a working pressure of 2.0 mTorr at room temperature. The target surface was cleaned by pre-sputtering for 10 min. Sputtering was carried out in a different oxygen flow rate (1, 5, 10, 15 sccm), while the Ar flow rate is fixed at 20 sccm (oxygen ratio, $O_2/(O_2+Ar)$ = 0.05, 0.2, 0.3, and 0.4). Indium tin oxide (ITO) source and drain electrodes, each 100 nm thick, were deposited by RF magnetron sputtering through photolithography with channel width (W) and length (L) of 500 μm and 100 μm, respectively, as shown in Figure 3.7. A channel layer was previously annealed at 350℃ for 1 hour in air before S/D electrode.

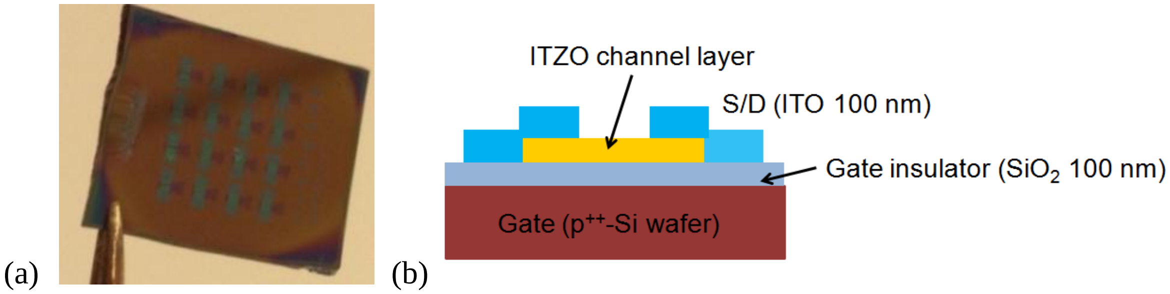

Figure 3.7. a-ITZO TFT on top of a SiO_2/p^{++}-Si wafer ((a) top view, (b) cross section view).

3.6 Characterization of a-ITZO TFT

3.6.1 Negative-Bias-Illumination-Stress (NBIS) Test

The device measurements were performed as a function of oxygen ratio in the dark at room temperature using an Agilent 4155C semiconductor parameter analyzer. NBIS and NBS tests were carried out with a gate bias stress of -20 V at a fixed drain-source voltage (V_{ds}) of 0.1 V during time periods up to 2×10^3 s with or without a green LED.

The transfer curves were measured after stress time periods by sweeping the gate-source voltage (V_{gs}) from -30 to +30 V at a V_{ds} of 0.1 V. The devices were illuminated by a green LED (467 nm) at 1 MHz. The light intensity and frequency of the LED were controlled by a function generator (AFG 3252, Tektronix). The actual light power density of the green LED (1.5 $mW \cdot cm^{-2}$) was measured using a power meter (Newport Model 1936-R).

3.6.2 Persistent Photocurrent (PPC) Measurement

The PPC measurement was also performed with a green LED in the dark at room temperature using a semiconductor parameter analyzer (Agilent 4155C), as shown in Figure 3.8. The PPC test was carried out in a depletion region with a V_{GS} of -20 V (oxygen ratio 0.3, 0.4) or -27 V (oxygen ratio 0.2) at a fixed V_{DS} (0.1 V) for 500 s, with a green LED turned on (200 s) and off (300 s).

The devices were illuminated by a green LED (467 nm) at a frequency of 0.5 Hz. The light intensity and frequency were controlled using a function generator (AFG 3252, Techtronix). The actual light power density (2.2 $mW \cdot cm^{-2}$) was measured using a power meter

(Model 1830-C, Newport). The drain-source current (I_{DS}) variation was monitored as a function of time as the LED was turned on and off.

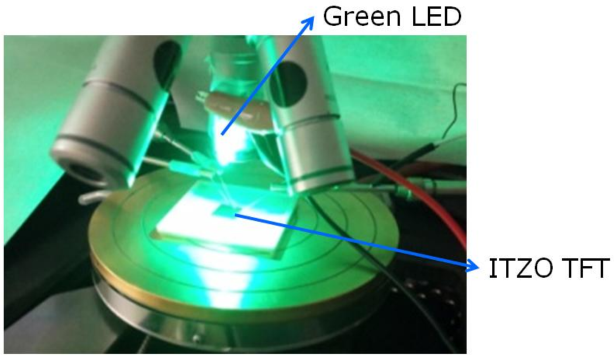

Figure 3.8. Persistent Photocurrent (PPC) measurement set-up

Chapter 4. Result and Discussion

4.1 Hydrothermally-Grown Single Crystal of ZnO Schottky Barrier Diode

4.1.1 Current-Voltage (IV) / Capacitance-Voltage (CV) Measurement

Figure 4.1 shows the typical IV measurements of Pd/ZnO Schottky barrier diodes. Leakage current under a reverse bias of -2 V at room temperature amounts to 2.8×10^{-5} A. It is rectified by more than three orders of magnitude to a value of 4.61×10^{-2} A under a forward bias of +2 V. Therefore, a clear rectifying behavior was found for the Pd/ZnO Schottky Barrier Diode (SBD).

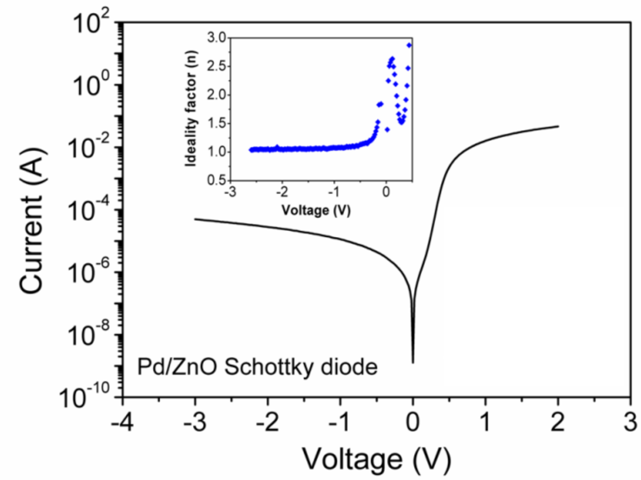

Figure 4.1. I-V characteristics of the Pd/ZnO SBD from -3 to 2 V at room temperature. The ideality factor (n) is shown in the inset.

The values of ideality factor (n) are also plotted in the inset of Figure 4.1. The barrier height is most commonly calculated at zero bias from Equation (3.1), so the barrier height ($\varnothing_B$) is for zero bias. While the values of ideality factor (*n*) is close to 1.0 at the reverse bias from -2.5 to -0.5 V, *n* started to increase from 1.0 after -0.5 V toward the forward direction. It could be attributed to the carrier recombination, tunneling, or interfacial layer between the metal and semiconductor. [5] The saturation current (I_s) and Schottky barrier height ($\emptyset_B$) were obtained respectively to be 1.6×10^{-7} A and 0.85 eV in our device.

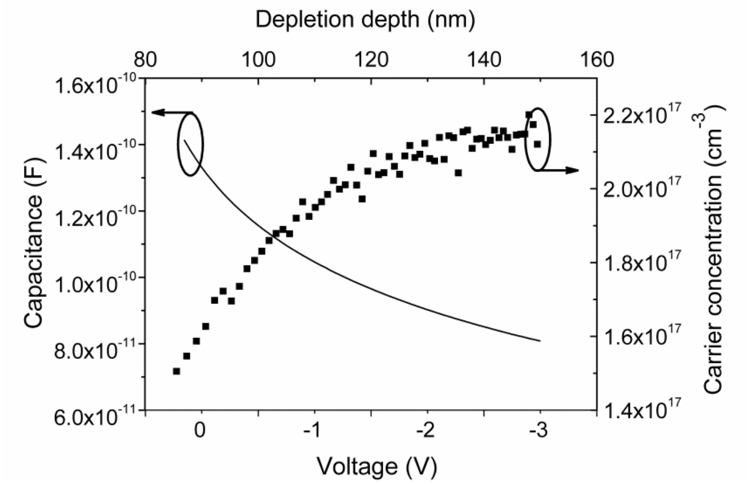

Figure 4.2. CV characteristics of the Pd/ZnO SBD as a function of reverse bias at 1 MHz. The carrier concentration versus depletion width was also plotted.

Schottky metal	n	I_{rev} at -1 V (A)	$\emptyset_{B, I\text{-}V}$ (eV)	$\emptyset_{B, C\text{-}V}$ (eV)	V_{bi} (V)	$N_{d, C\text{-}V}$ (cm^{-3})
Pd	2.08	1.14×10^{-5}	0.85	0.86	0.77	2.0×10^{17}

Table 4.1. The extracted parameters of the Pd/ZnO SBD at room temperature; the ideality factor (n), reverse current (I_{rev}), barrier heights ($\emptyset_B$), built-in voltage (V_{bi}) and the carrier density (N_d).

The CV measurement was also measured in the range between +0.5 V and -3 V at 1 MHz using an Agilent E4980A LCR meter in dark conditions, as shown in Figure 4.2. From the slope ($1/C^2$ vs V), we find $N_d = 2.0\times10^{17}$ cm^{-3}, which is close to the value of 0.86×10^{17} cm^{-3} (by Hall measurement). Additionally, the Schottky barrier height is $\emptyset_B = 0.863$ eV using the intercept voltage $V_{bi} = 0.77$ V (from the intercept of $1/C^2$ versus V plot on the V-axis) at room temperature, when $N_d = 0.86\times10^{17}$ cm^{-3} is used from Hall measurement. The Pd/ZnO SBD properties are summarized in Table 4.1.

4.1.2 Shallow-Level Defect States Distribution by DLTS

DLTS signal produces a maximum temperature and at that maximum temperature, the emission rate (rate window) is only determined by the preselected time (emission rate = $\ln(t_1/t_2)/(t_2-t_1)$, from 0.034 ms^{-1} to 0.888 ms^{-1}). This kind of DLTS system is known as the BOXCAR DLTS. Finally, we obtained the defect energy level (E_t) and capture cross section (σ_n) from the Arrhenius plot (Figure 4.3 (right)).

In Figure 4.3, one main defect energy level appeared, labeled E3 with energy position of E_c - 0.27 eV. This energy level was commonly observed in hydrothermally grown ZnO. The apparent capture cross section was about 1.36×10^{-16} cm^2. The oxygen vacancy (V_o) was tentatively assigned as a source of this defect level, E3. However, the origin of this defect is still under debates. Even though, DLTS stands for the deep-level transient spectroscopy, this technique can detect only a shallow-level defect states near the conduction band in wide bandgap materials. For the deep-level defect states, photo-excited charge collection spectroscopy (PECCS) method has been used with a sputtered ZnO TFT.

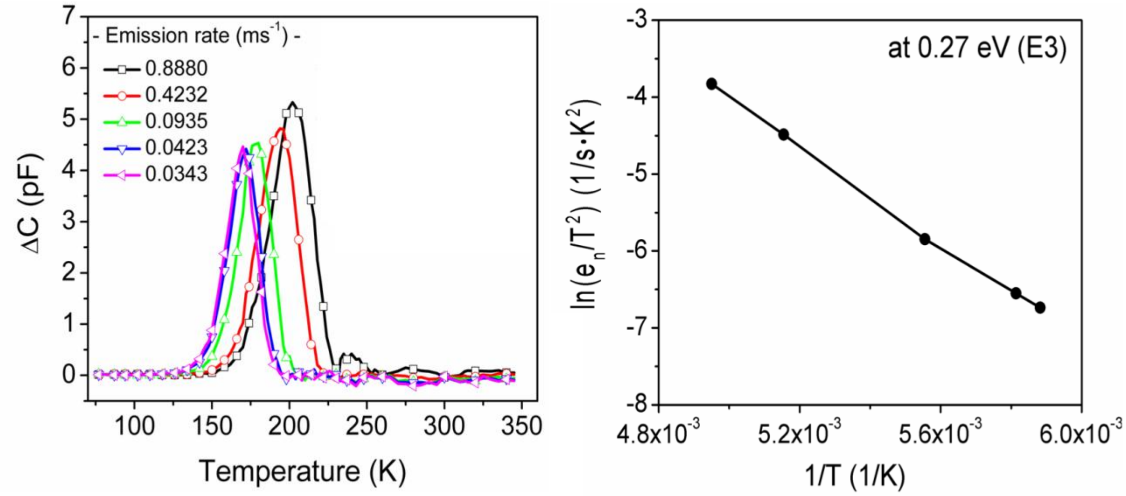

Figure 4.3. DLTS spectra (left) of the Pd/ZnO SBDs sample for the different emission rates from 0.0343 ms^{-1} (t_1 = 20.2 ms, t_2 = 40.4 ms) to 0.8880 ms^{-1} (t_1 = 0.78 ms, t_2 = 1.56 ms). Arrhenius plot of the level E3 (right).

In addition, DLTS signal is actually the distribution of signal originated from each trap levels, hence, the DLTS signal is simply proportional to the trap concentration by the given equation: [83]

$$N_t = 2N_d \frac{\Delta C_{max}}{C_o} \tag{4.1}$$

where N_d is the carrier concentration, ΔC_{max} is the maximum transient capacitance amplitude, and C_0 is the capacitance of the Schottky diode under reverse-biased conditions at -2.5 V (C_0 = 85 pF). Therefore, the defect concentration can be directly related to the respective magnitudes of the DLTS spectrum over the possible energies. The temperature can be also related to the trap energy level, and the defect distribution can be calculated by the electron emission rate equation: [2]

$$E_c - E_t = KT\ln(\sigma_n \nu_{th} N_c \tau_0) \tag{4.2}$$

where KT is the thermal energy, σ_n is the electron capture cross section area of the trap, ν_{th} is the electron thermal velocity, N_c is the effective density of states in the conduction band, and τ_0 is the emission time constant that is approximated to be half of the time width used in this measurements ($\tau_0 = 20$ ms).

In this work, σ_n is assumed to be 10^{-16} cm^2 and independent of the temperature. The available number of states in the conduction band (N_c), which is temperature dependent, is calculated using $m^* = 0.27m_0$. The defect concentration versus defect energy level is calculated by equations (4.1) and (4.2). Finally, Figure 4.4 shows the results of distribution of defect states depending on the defect energy level. The maximum defect concentration is located at 0.277 eV below the conduction band with $N_{t,max} = 3.66\times10^{16}$ cm^{-3}. We observed noisy data due to the thermal instability at the range of 0.4 – 0.57 eV. As mentioned before, the reason for E3 level defects near the conduction band is not clear yet. However, there has been no consensus on these issues concerning the origin of defects in ZnO.

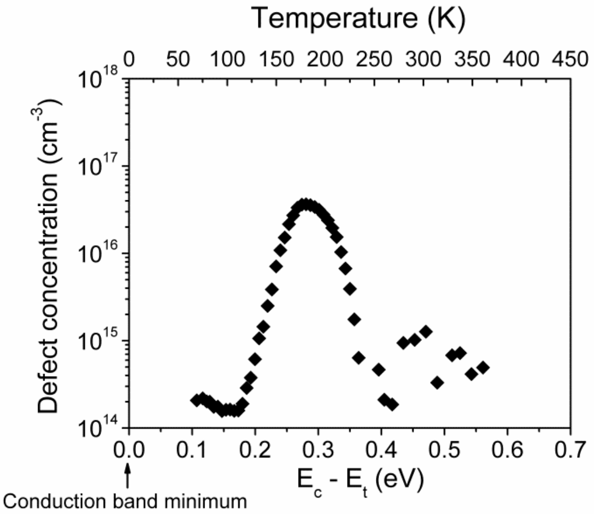

Figure 4.4. The correspondent subgap density of states as a function of defect energy from the conduction band.

Additionally, for the first time, we observed the defect state distribution from acceptor- to donor-like defect states at 0.36 eV under the CBM in the ZnO band gap from the variations of transient capacitance slope. As the temperature increased from 140 to 230 K, the transient capacitance was decreased. At this temperature range, the defect energy level corresponds to 0.2 – 0.36 eV below the CBM, including E3 (0.27 eV). Our results showed acceptor-like defects near the CBM. This behavior could be caused by the neutralization of ionized defects through the thermal emission of carriers in depletion region and increased depletion width due to the reduction of total charge density, since the acceptor-type defect is neutral when it is unoccupied and negatively charged when it is filled with an electron. As a result, the transient capacitance was decreased. This is consistent with an acceptor-like (V_{Zn}, Oxygen interstitial (O_i), O_{Zn} etc.) defect behavior. The origin of an acceptor-like defect is still unclear and complex. It requires further study to find the precise evidence of the defect formation.

However, transient capacitance was gradually increased at the temperature range, 230–340 K (corresponding to 0.36 – 0.57 eV below E_c). Contrary to the acceptor-type defects, this behavior could be caused by the increase of total charge density through the thermal emission of carriers in depletion region and decreased depletion width, which results in the increase of the transient capacitance, since the donor-type defect is positively ionized when it is unoccupied and neutral when it is filled with an electron. This transition of defect identity is still unclear and more studies are needed, so I don’t want to claim this behavior. This behavior is difficult to interpret due to measurement artifacts and equipments.

4.2 Sputtered ZnO TFT

4.2.1 Result of Sputtered ZnO Thin-Film Characterization

For the x-ray diffraction (XRD) patterns of sputtered ZnO films, the orientation of (002) peaks were observed as shown in Figure 4.5, indicating c-axis oriented growth of the hexagonal structure, depending on oxygen ratios. Parameters are summarized in Table 4.2.

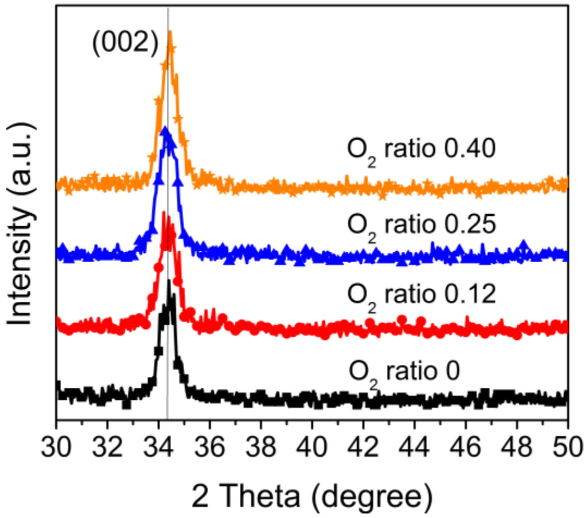

Figure 4.5. The XRD spectra of sputtered ZnO films as a function of the oxygen ratios.

The full-width at half-maximum (FWHM) of (002) diffraction peak has been increased from 0.65° to 0.88° and grain size reduced from 128 Å to 94 Å with increasing oxygen ratios up to 25 % (0.25). The reduced kinetic energy of sputtered particles could reduce the surface diffusion energy. This represents that ZnO crystallinity degraded accordingly. On the other hand, FWHM and grain size at an oxygen ratio of 40 % (0.40) has been recovered back to their initial level measured at an oxygen ratio of 0 % (0.0). The reason for this result is not clearly understood yet.

$O_2/(O_2+Ar)$	FWHM (deg.)	Grain size (Å)	C-axis lattice constant (Å)
0 % (0.0)	0.65	128	5.21
12 % (0.12)	0.69	120	5.24
25 % (0.25)	0.88	94	5.23
40 % (0.40)	0.65	128	5.20

Table 4.2. The extracted parameters of sputtered ZnO film from XRD at different oxygen ratios.

Furthermore, the X-ray reflectivity (XRR) analysis (Figure 4.6) and bias stress instability test (Figure 4.7) were performed to understand the interfacial states at the channel/dielectric of sputtered ZnO TFT. We observed the increased interfacial roughness up to an oxygen ratio of 25 % (0.25) from the XRR data, as summarized in Table 4.3, and also the positive bias stress instability test showed the same trend. The positive bias stress instability of sputtered ZnO TFTs was examined under a gate bias of + 20 V at a V_{ds} of 5 V for 0, 1, 10, 100, 1000, and 5000 s, as shown in Figure 4.7. It is well known that the threshold voltage (V_{th}) shift after bias stress is directly proportional to the trapping states near or at the interface ZnO/SiO_2 of sputtered ZnO TFT. [1]

From XRR and bias stress test, we observed the roughness at the interface of ZnO/SiO_2 increased up to oxygen ratio of 25 % (0.25), and then decreased again at oxygen ratio of 40 % (0.40). The reason of this is not yet understood. On the other hand, it is hard to characterize interfacial trap density (D_{it}) quantitatively in a working TFT. To determine D_{it}, quasi-static capacitance-voltage (CV) technique, [127] conductance method, or Terman method [83] have been widely used. The detectable defect energy range of these methods is usually limited up to 1.0 eV under the conduction band, so these can detect shallow-level defects for wide band gap materials.

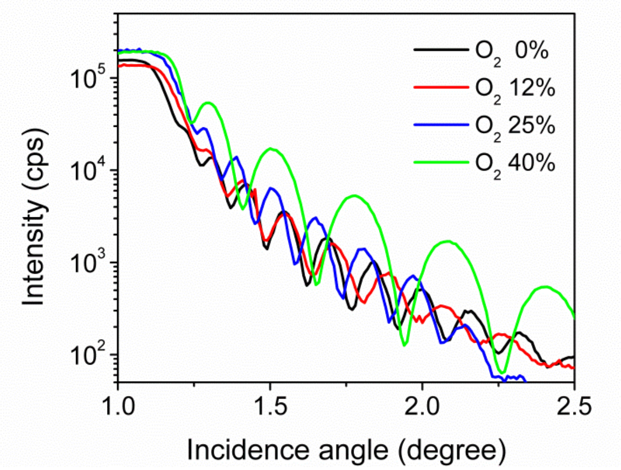

Figure 4.6. The XRR analysis depending on oxygen ratios. (sputtered ZnO on top of a SiO_2/p^{++}-Si wafer)

$O_2/(O_2+Ar)$	Roughness (Å)	Density (%)	Thickness (Å)
0 % (0.0)	14	90.8	809
12 % (0.12)	16	97.3	694
25 % (0.25)	28	98.1	744
40 % (0.40)	13	99.1	759

Table 4.3. The extracted parameters of simulation fitting for the sputtered ZnO film depending on the oxygen ratios. (100 % density of ZnO = 5.61 ($g\cdot cm^{-3}$)).

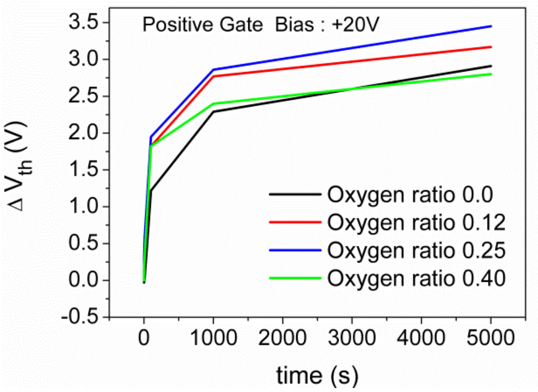

Figure 4.7. Threshold voltage shift after positive gate bias stress as a function of oxygen ratio.

The surface morphology was also observed by Nova 230 Nano Scanning Electron Microscopy (SEM). Images are shown in Figure 4.8 at various oxygen ratios in order to reveal that the average surface grain size decreased with increasing oxygen ratios up to 25 % (0.25).

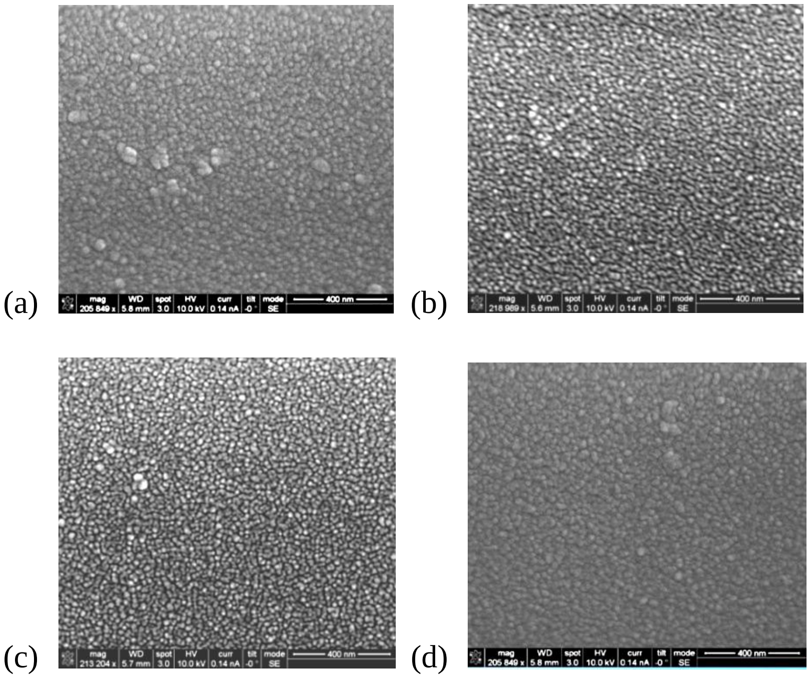

Figure 4.8. SEM images of sputtered ZnO films at different oxygen ratios; (a) 0 %, (b) 12 %, (c) 25 %, and (d) 40 %.

4.2.2 Deep-Level Defect States Distribution of Sputtered ZnO TFT from PECCS

To examine the electronic states of deep-level defect near or at the interface, Kimoon Lee *et al.*, introduced the Photo-excited charge collection spectroscopy (PECCS) in the working TFTs. [51] The trapped charges in certain energy level are ejected by photon energy and collected at Source/Drain electrodes. During this process, V_{th} is shifted. This change of the photo-induced V_{th} by sweeping over the photon energy provides us with the density-of-state of traps in that photon energy under the conduction band. We measured the photo-shifted V_{th} of sputtered ZnO TFTs under the monochromatic light. Figure 4.9 shows the transfer characteristics of the sputtered ZnO TFTs deposited at different oxygen ratios, which is measured in the dark and detailed device parameters in the linear region are also summarized in Table 4.4.

Both the V_{th} and V_{on} increased as a function of the increase in oxygen ratios during growth. This means the reduction of free carriers in the ZnO films due to the suppressed shallow-level donors at higher oxygen ratio. Therefore, the positive V_{th} shift at higher oxygen ratio is reasonable. It seems like that higher oxygen ratio during sputtering growth suppressed the complex oxygen-related defects. The reduced on-state current (I_{on}) at higher oxygen ratio tells us the decrease of free carriers, contributed from the suppression of donor-like trap centers. In the previous literatures, Mamoru Furuta *et al.*, also showed the positive shift of V_{on} with increasing the oxygen ratio when the ZnO film was changed from Zn- to O_2-rich condition by changing the O_2 pressure, and proposed that the origin of this shift would be the Zn-related donor-like native defects near the E_c. [128] Hong Woo Lee *et al.*, showed that the on-state I_d and μ_{fe} values of the ZTO TFTs at the oxygen ratio of 0 % are higher than those at the oxygen ratio of 0.3 %. [23]

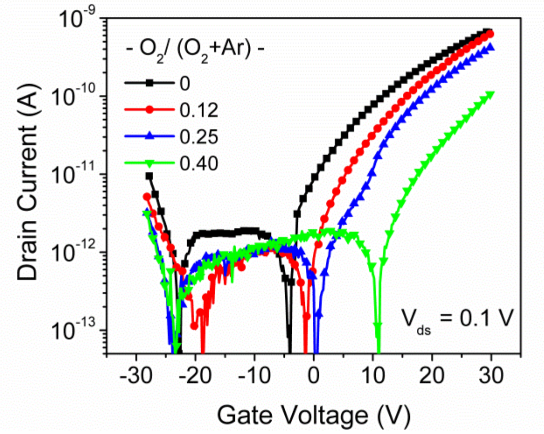

Figure 4.9. The representative transfer curves of sputtered ZnO TFTs depending on oxygen ratios (in the linear region) in the dark, by sweeping V_g from -30 to +30 V. Reproduced with Ref. [117]

O_2/(O_2+Ar)	V_{th} (V)	V_{on} (V)	μ_{fet} (cm^2 V^{-1} s^{-1})	SS (V dec^{-1})	$I_{on/off}$
0 % (0.0)	16.56	-4.0	0.007	0.88	3.04×10^4
12 % (0.12)	19.45	-1.4	0.008	1.09	3.30×10^4
25 % (0.25)	19.47	0.4	0.005	1.26	2.03×10^4
40 % (0.40)	22.55	11.0	0.002	2.72	1.47×10^4

Table 4.4. The extracted device parameters of sputtered ZnO TFTs with different oxygen ratios in the linear region (V_{ds} = 0.1 V). Reproduced with Ref. [117]

The photo-induced transfer curves of the ZnO TFTs under λ = 600, 500, 400, and 300 nm illumination (with dark transfer curve) were shown depending on the oxygen ratios in

Figure 4.10 (a), (b), (c), and (d) at V_{ds} = 0.1 V (in the linear regime) to minimize the error due to the large drain electric field. The maximum drain leakage current (at V_g = - 20V) under UV illumination (300 nm) increased up to about 9.46×10^{-9} A in Figure 4.10 (a), which is much higher than the dark leakage current. Similar photo-response transfer curve was obtained when the photon energy was at the range of 1.8 – 2.0 eV.

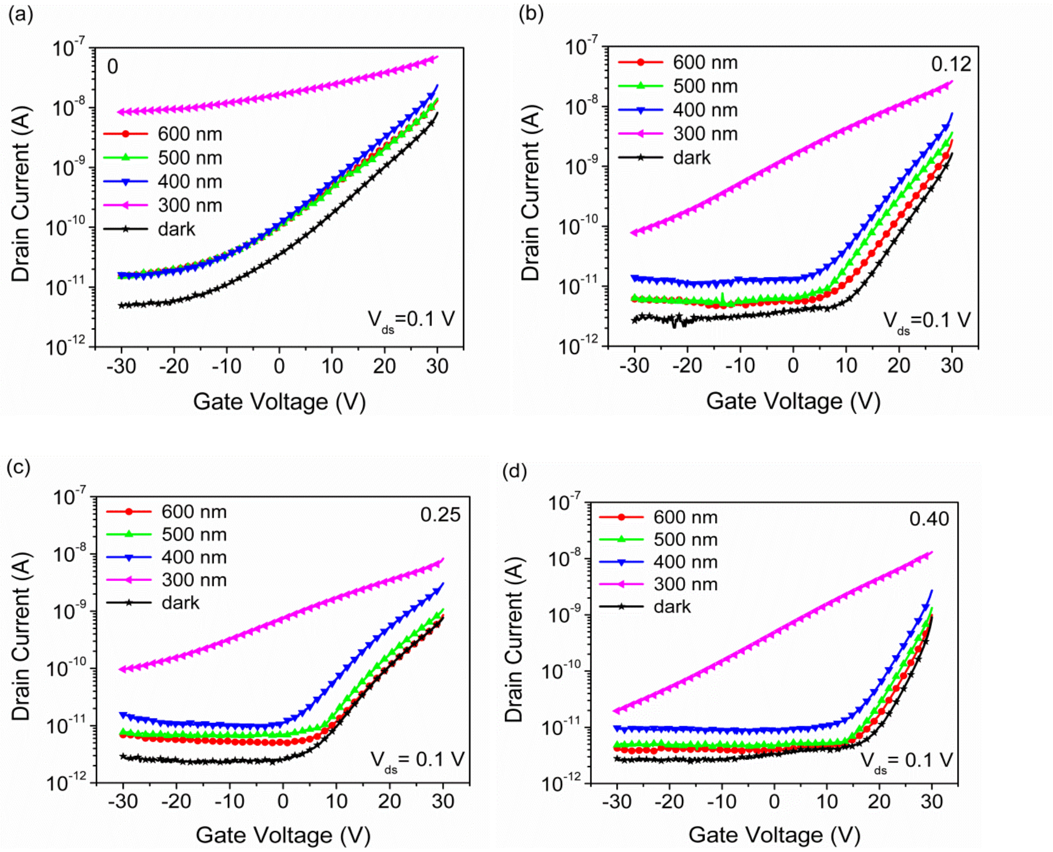

Figure 4.10. The change in photo-induced transfer curves at dark, 600, 500, 400, and 300 nm illumination on the sputtered ZnO TFTs with different oxygen ratios of (a) 0, (b) 0.12, (c) 0.25, and (d) 0.40 by sweeping V_g from +30 to -30 V. Reproduced with Ref. [117]

The presence of some sub-gap defect states near 1.8 – 2.0 eV under the conduction band minimum must have induced the photo-leakage current under the 600 nm illumination. These increased photo-induced leakage currents are contributed to the photo-excited carrier generation from the sub-gap states to the conduction band, although the photon energy was smaller than the band-gap energy. The average optical power density was measured about 0.2 mW·cm^{-2}. Therefore the photon flux of at least 6.0×10^{14} cm^{-2}·s^{-1} (at 600 nm) can be obtained based on this information. This photon flux should be absorbed near or at the channel/dielectric interface by inducing the photo-leakage current. To characterize the deep-level defect density-of-state (DOS) distribution in the sub-gap states of the ZnO TFTs, the shift of photo-induced V_{th} of ZnO TFTs under the monochromatic light was measured at the range of 350 – 800 nm. The shift of V_{th} under illumination was shown in Figure 4.11 (a) depending on oxygen ratio, by comparing with the value of V_{th} in the dark.

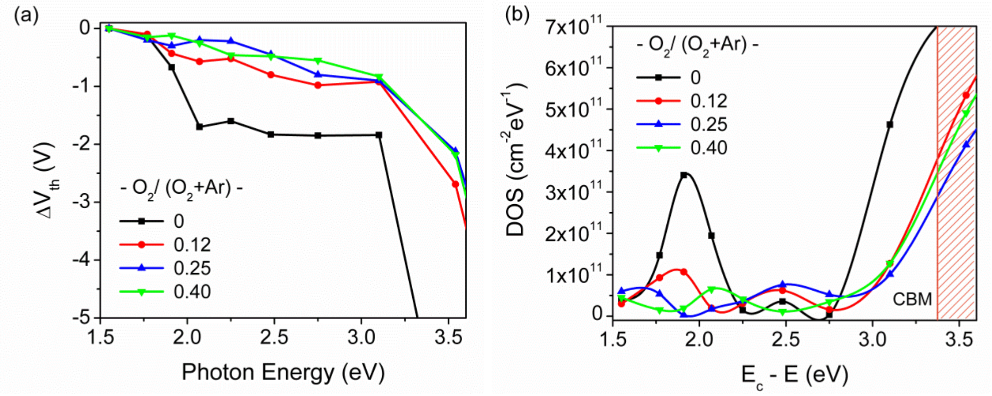

Figure 4.11. (a) The shift of photo-induced threshold voltage of as-sputtered ZnO TFTs depending on oxygen ratios as a function of the photon energy. (b) The extracted defect density of states (DOS) distribution from the shift of photo-induced threshold voltage. Reproduced with Ref. [117]

The deep-level defect DOS near or at the channel/dielectric interface in the working ZnO TFT was directly extracted, as shown in Figure 4.11 (b) from the shift of photo-induced

V_{th} by using the following equation (4.3): [3]

$$\mathrm{DOS}\ (\mathrm{CBM} - \varepsilon) = \frac{C_{ox}}{q}\frac{dV_{th}\ (\varepsilon)}{d\varepsilon} \qquad (4.3)$$

where C_{ox}, q, V_{th}, and ε represent the dielectric capacitance per unit area ($F \cdot cm^{-2}$), the electronic charge ($q < 0$), the photo-induced V_{th} (V), and the photon energy (eV), respectively.

We observed that the DOS of traps in the range of 1.8 – 2.0 eV under the conduction band was suppressed in the linear region as increasing the oxygen ratio in Figure 4.11 (b). It is also noted that the monochromatic light excited the oxygen-related defect states (V_o) and they became the shallow singly (V_o^{+}) or doubly-ionized donor states (V_o^{2+}) from deep-level neutral states (V_o), [28] as shown in Figure 4.12. This photo excitation/generation process due to the presence of sub-gap defect states near 1.8 – 2.1 eV caused the negative shift of V_{th} and increased photo-leakage current under the visible light. In such process, the photo-excited free electrons from the neutral V_o are rejected into the conduction band. This result is consistent with the previous studies of the defect distribution of the ZnO-based materials. [28, 129]

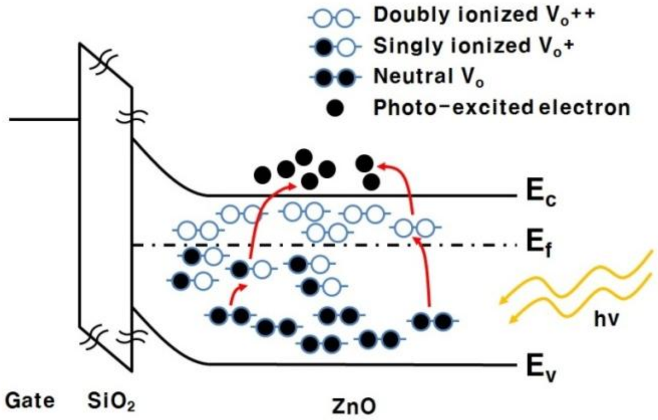

Figure 4.12. The proposed band diagram of sputtered ZnO TFT with monochromatic light at a negative gate voltage. Reproduced with Ref. [117]

For further example, Sang-Hun Jeong *et al.*, showed that the visible emission in the room temperature photoluminescence for RF magnetron sputtering ZnO films was decreased with increasing oxygen ratios. [44] Shin-ichi Shimakawa *et al.*, also showed that the photo-leakage current of ZnO TFTs decreased at higher oxygen ratios during sputtering. [130] As oxygen ratios increased during sputtering growth, we observed a reduction of deep-level oxygen deficiencies in ZnO films by PECCS method.

4.2.3 XPS Spectra of Sputtered ZnO Thin-Films

XPS measurements were performed for stoichiometry and defect analysis in Figure 4.13. All sputtered ZnO were annealed under vacuum at 350℃ for 1 hour. By using the Gaussian curves, the oxygen 1s peak was resolved into 3 components, centered at 530.15 ± 0.15, 531.25 ± 0.20 and 532.40 ± 0.15 eV. [131, 132] The component peak at 530.15 ± 0.15 eV is attributed to oxygen atoms at regular lattice sites (O_{I}) in a fully-oxidized stoichiometric surrounding.

The medium peak at 531.25 ± 0.20 eV is associated with oxygen atoms in the oxygen deficient regions (O_{II}). So, measurement of this component peak may be correlated to the changes in the concentration of oxygen vacancies. The relative intensity of this medium component peak decreased as a function of the increase of oxygen ratios. The oxygen-rich condition would be expected to suppress the oxygen vacancy-related defect in ZnO thin films. The highest binding energy peak at 532.40 ± 0.15 eV is known to be associated with weakly bound contaminant species, such as –OH, –CO_3, H_2O, and O_2 on the surface of ZnO films (O_{III}).

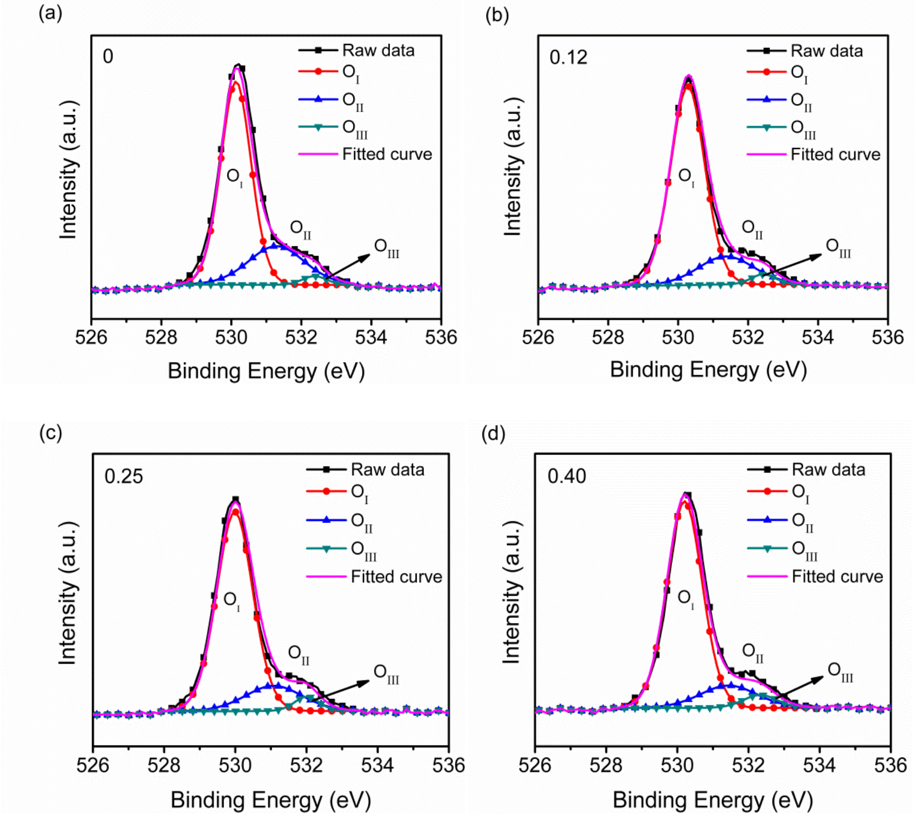

Figure 4.13. XPS spectra of O 1s core level of sputtered ZnO for different oxygen ratios of (a) 0, (b) 0.12, (c) 0.25, and (d) 0.40. Reproduced with Ref. [117]

4.3 Sputtered a-ITZO TFT

4.3.1 Effect of Oxygen Ratio on a-ITZO TFTs' Device Performance

Transfer curves of the a-ITZO TFTs at different oxygen ratios are shown in Figure 4.14. Extracted device parameters are also summarized in Table 4.5. The linear mobility (μ_{lin}) of devices slightly increased as a function of oxygen ratio [$O_2/(O_2+Ar)$]. Both V_{th} and turn-on voltage (V_{on}) were positively shifted at high oxygen ratios during sputtering growth. This should be attributed to the reduction of free carrier concentration in a-ITZO films at high oxygen ratios due to the suppressed shallow-level donors. It seems that higher oxygen ratio during growth suppressed the oxygen-related defects whether those are shallow- or deep-level defects. In addition, deep-level defects associated with oxygen vacancies were also reduced at high oxygen ratios, which are related to the photo instability. We examined this reduction of deep-level oxygen-related defects at high oxygen ratios by measuring the persistent photocurrent and XPS spectra.

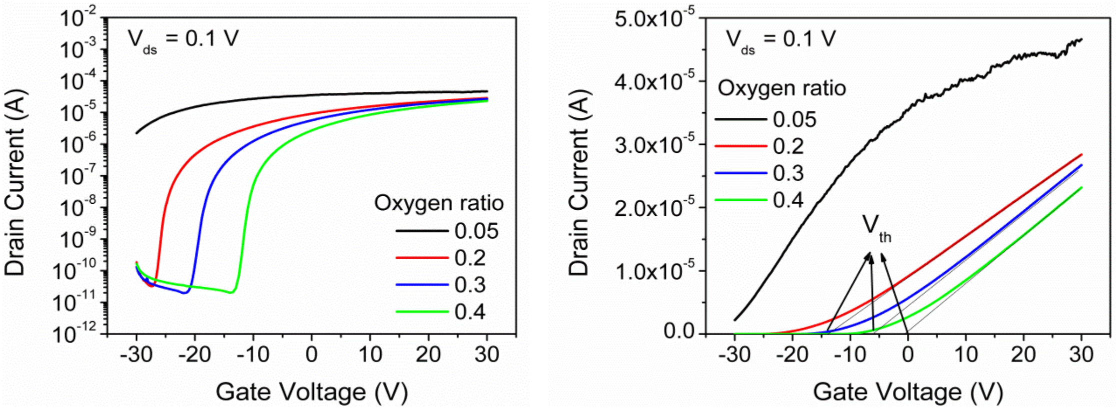

Figure 4.14. Representative transfer curves of sputtered a-ITZO TFTs depending on oxygen ratios (in the linear region) in the dark. (Left: log scale, Right: linear scale)

$O_2/(O_2+Ar)$	V_{th} (V)	V_{on} (V)	V_{lin} (cm^2 V^{-1} s^{-1})	SS (V dec^{-1})	$I_{on/off}$
0.2	-14.5	-27.1	40.8	0.8	8.8×10^5
0.3	-6.2	-20.5	46.5	0.88	1.4×10^6
0.4	-0.7	-12.7	47.5	1.26	1.2×10^6

Table 4.5. Extracted device parameters of sputtered a-ITZO TFTs at different oxygen ratios in the linear region (V_{ds} = 0.1 V).

4.3.2 Persistent Photocurrent (PPC) Test

Here, we confirmed that the photocurrent persists long after illumination was removed. Normalized drain–source current as a function of time is shown in Figure 4.15 when a-ITZO TFTs are subjected to light by a green LED. Each device exposure under light was maintained for 200 s and devices were allowed to recover for about 300 s. The devices were illuminated by a green LED (467 nm) with a frequency of 0.5 Hz. The I_{DS} variations were monitored as a function of time. Note the faster increase in photocurrent upon light exposure and its slower exponential decrease upon switching the green LED off at an oxygen ratio of 0.2. The a-ITZO devices exhibit parabolic increase and exponential decrease in photocurrent, however do not reach its initial value measured in the dark even after several hours, a situation in which PPC is apparent. The a-ITZO film at an oxygen ratio 0.2 is the most sensitive to illumination since it exhibits the largest increase in photocurrent. Also, slower recovery at an oxygen ratio of 0.2 is observed when the light is turned off, as indicated by the normalized current levels in Figure 4.15.

The results presented in this work suggest that higher concentration of oxygen vacancies (i.e., at an oxygen ratio of 0.2) induce faster photo response, generating higher free carriers by the excitation of electron-hole pairs, and slower recovery upon turning the light off. It is theoretically reported that PPC can be caused by ionization of V_O sites. An energy barrier (0.2-0.3 eV) formed from local atomic strain energy between V_O^0 and V_O^{2+} states hinders relaxation. An energy barrier makes the recovery rather sluggish and slow, which results in PPC. [27, 29] It may therefore be understood that the PPC effect originates from the excitation of electron−hole pairs near the valence band tail states, and the energy barrier (0.2 – 0.3 eV) between V_O^0 and V_O^{2+} states from first-principle calculations describes the slow recovery at an oxygen ratio of 0.2. [30]

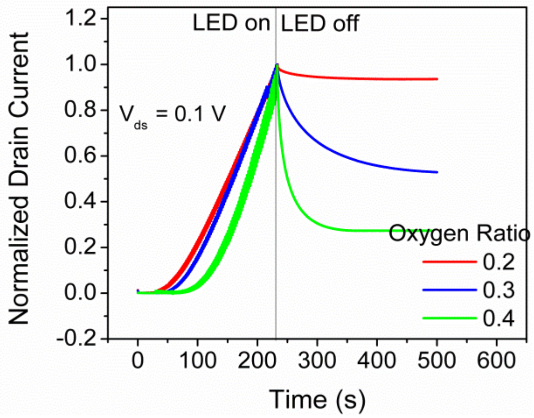

Figure 4.15. Normalized photo current after the green LED is turned on and off, with various oxygen ratios.

$O_2/(O_2+Ar)$	τ (s)	β
0.2	10^6 > several days	0.2
0.3	10^3 > several hours	0.4
0.4	≈ 10^3	0.26

Table 4.6. Stretched exponential parameters of sputtered a-ITZO TFTs at different oxygen ratios.

Here, the decay of the PPC follows a stretched exponential model shown in the equation (4.4): [30]

$$I_{DS}(t) = I_{DS}(0)\{\exp[-(t/\tau)^{\beta}]\} \tag{4.4}$$

where $I_{DS}(0)$, τ, and β represent the current at the onset of decay, relaxation time (s), and a measure of the distribution of defects that control the decay process, respectively. Stretched-exponential parameters are obtained by fitting decay curves into the equation (4.4). Stretched-exponential parameters are summarized in Table 4.6, predicting a recovery time on the scale of several days at an oxygen ratio of 0.2.

4.3.3 XPS Spectra of Sputtered a-ITZO Thin-Films

XPS measurements were also performed for the stoichiometry and defect analysis as shown in Figure 4.16. All sputtered ITZO films were annealed under atmosphere condition at 350℃ for 1 hour before XPS measurements. By using the Gaussian curves, the oxygen 1s peak was resolved into 3 components, centered at 530.15 ± 0.15 (O_{I}), 531.25 ± 0.20 (O_{II}) and 532.40 ± 0.15 eV (O_{III}). The medium peak (O_{II}) is associated with an oxygen deficiency in ITZO films. We observed the reduction of medium peak as a function of oxygen ratios. The oxygen-rich condition would be expected to suppress the oxygen deficient region (O_{II}) at higher oxygen ratios.

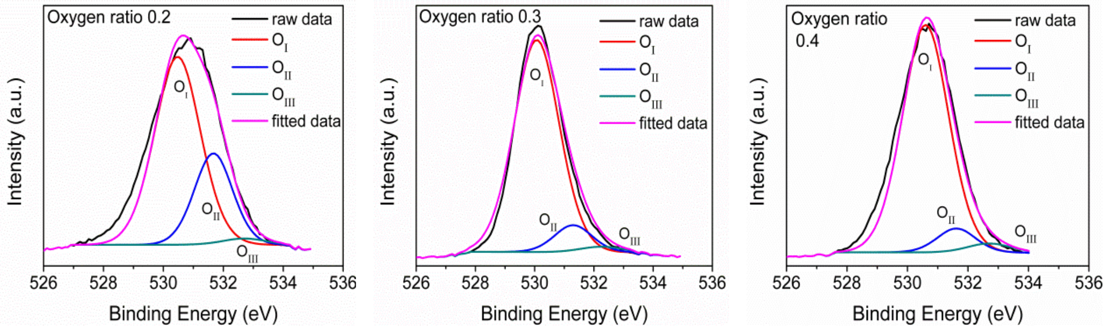

Figure 4.16. XPS spectra of O 1s core level of sputtered a-ITZO at oxygen ratios of 0.2, 0.3, and 0.4.

4.3.4 Instability of a-ITZO TFTs

The stability tests under illumination stress (IS), negative bias stress (NBS), and negative bias illumination stress (NBIS) are carried out on a-ITZO TFTs as a function of oxygen ratio. The transfer curves and shift of threshold voltage are shown in Figure 4.17 and 4.18, respectively. The maximum stress duration was 2000 s.

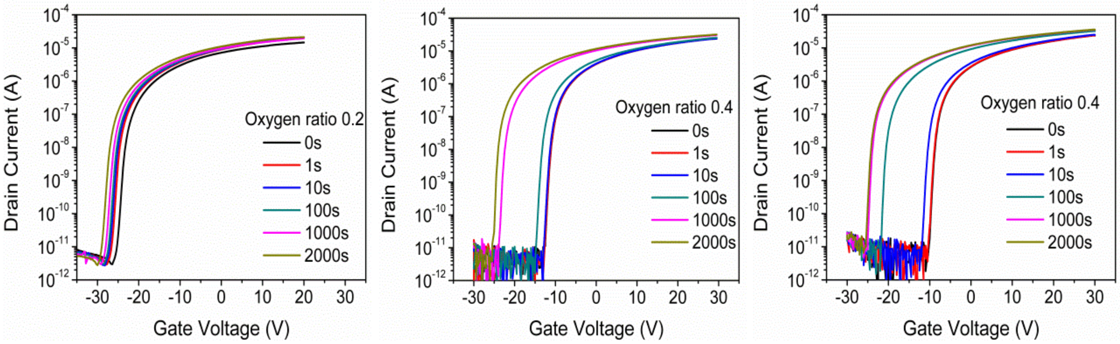

Figure 4.17. Shift of transfer curves under the Illumination stress (IS) at an oxygen ratio 0.2 (left), under the Negative bias stress (NBS) at an oxygen ratio of 0.4 (middle), and under the Negative bias illumination stress (NBIS) at an oxygen ratio of 0.4 (right) in a-ITZO TFTs

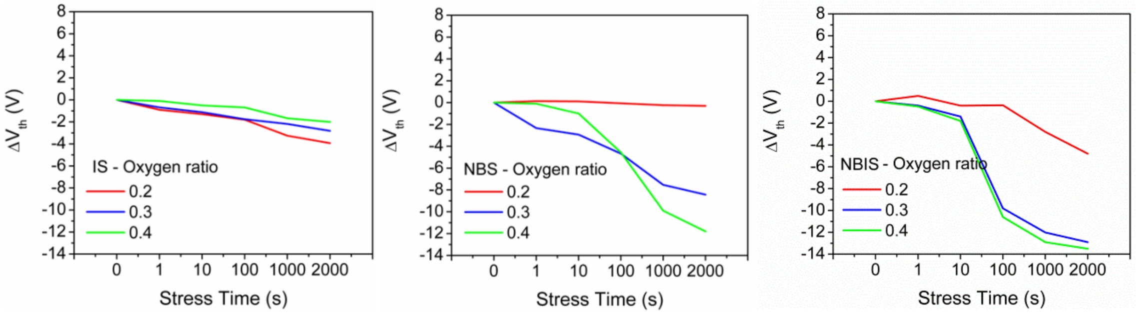

Figure 4.18. Shift of threshold voltage (ΔV_{th}) as a function of time under the Illumination stress (IS) (left), Negative bias stress (NBS) (middle), and Negative bias illumination stress (NBIS) in a-ITZO TFTs, for various oxygen ratios.

We already confirmed that deep-level oxygen-related defect centers were suppressed at higher oxygen ratios from the PPC measurements and XPS spectra, therefore photo stability was improved by reducing deep-level defects associated with oxygen vacancies at higher oxygen ratios. On the other hand, the device stability under NBS or NBIS significantly degraded at higher oxygen ratios. The reason for this phenomenon should be contributed to increased defect states at the interfacial layer between the channel and dielectric layer due to severe oxygen ion bombardment during growth by sputtering. [1, 133-135] It is because that increased oxygen ions were moved towards the substrate at higher oxygen ratios. These high-energetic oxygen ions could produce re-sputtering processes on the surface of the substrate that causes rough surface morphology. As a result, interfacial defect states could increase at higher oxygen ratios, leading to the degradation under bias or photo-bias stress, namely NBS or NBIS. [133, 136]

On the other hand, oxygen-related defect states within the bulk of IZTO film were reduced at a high oxygen ratio of 0.4 by PPC measurement. Therefore, the bulk part of growing ITZO films at a high oxygen ratio of 0.4 does not result in high-energetic oxygen ions compared to the interfacial surface. This was proved by measuring the root-mean-square (RMS) surface roughness of various ITZO film thicknesses at an oxygen ratio of 0.4 by using AFM. The ITZO films of 2, 4, and 7 nm thicknesses at oxygen ratio 0.4 each had a similar roughness of about 0.25 nm, which is much smoother than that of the interface layer (0.6 nm, measured by XRR). Only the first few layers of the growing ITZO film at the interface should be severely affected by high-energetic oxygen ions at an oxygen ratio of 0.4. Taking into account that the number of bonds of a surface atom is lower than that of a bulk atom, this might be due to the lower defect formation energy of a surface atom in the first monolayer. [135] Increased interfacial defect density was also examined by subthreshold swing (SS) value, hysteresis analysis and XRR measurement.

Typically, interface states of any metal-oxide semiconductor TFTs are an important factor for high mobility and better bias stress stability. However, in our work, device stability under bias or photo-bias stress (namely NBS or NBIS) degraded at higher oxygen ratios, though photo stability was improved. The effect of interface defect states on device stability should be the most dominant factor especially under a gate bias stress. The interfacial roughness must be related with interfacial defect states in sputtered a-ITZO TFTs. Interestingly, the SS value in Table 4.5 increased as the interfacial defect or trap density increased, though the deep-level oxygen-related defect states were suppressed as increasing oxygen ratios. Accordingly, the SS value is directly related to the interfacial trap density (D_{it}) between the channel and dielectric layer as follows: [137]

$$\mathrm{SS} = \ln 10 \, \frac{k_B \mathrm{T}}{q} \left(1 + \frac{q^2 \mathrm{D_{it}}}{\mathrm{C_{ox}}}\right) \tag{4.5}$$

where q, k_B, T, and C_{ox} represent the elementary charge (C), the Boltzmann's constant ($eV{\cdot}K^{-1}$), the absolute temperature (K), and the gate oxide capacitance per unit area ($F{\cdot}cm^{-2}$), respectively.

In our a-ITZO transistor, the gate oxide capacitance per unit area is approximately 31.9 $nF{\cdot}cm^{-2}$ due to 100 nm of SiO_2. At room temperature, the interfacial trap density of our device with an oxygen ratio of 0.2 had $D_{it} = 2.76\times10^{12}$ $eV^{-1}{\cdot}cm^{-2}$. As oxygen ratios increased from 0.2 to 0.4, D_{it} increased from 2.76×10^{12} to 4.35×10^{12} $eV^{-1}{\cdot}cm^{-2}$. We suggest that the generation of trapped charges at/near the interface or hole trapping into a gate dielectric are believed to contribute to the significant change of V_{th} shift. This means that an additional source of charges from interfacial traps induced the significant negative shift of V_{th} under NBS or NBIS condition at higher oxygen ratios. The interfacial defect density (D_{it}) and shifts of V_{th} are summarized in Table 4.7.

$O_2/(O_2+Ar)$	SS (V dec^{-1})	$D_{it, max}$ (cm^{-2} eV^{-1})	IS $\Delta V_{th, max}$ (V)	NBS $\Delta V_{th, max}$ (V)	NBIS $\Delta V_{th, max}$ (V)
0.2	0.8	2.76×10^{12}	-4	0	-5
0.3	0.88	3.04×10^{12}	-3	-8	-13
0.4	1.26	4.35×10^{12}	-1	-12	-13

Table 4.7. Interfacial trap and shift of threshold voltage in a-ITZO TFTs under IS, NBS, or NBIS condition at various oxygen ratios.

Further evidence for charge trapping at/near the channel-insulator interface could be confirmed by the log (I_D)-V_{GS} hysteresis analysis. As indicated in Figure 4.19, a log (I_D)-V_{GS} hysteresis corresponds to a ΔV_{on} shift. This magnitude of V_{on} shift concomitant with hysteresis was consistent with interface defect density at/near channel-insulator interface. [138] The V_{on} shift due to hysteresis increased to around 7 V at an oxygen ratio of 0.4. At an oxygen ratio of 0.4, we observed a high V_{on} shift, which means increased density of interfacial traps. This is entirely consistent with increased D_{it} at an oxygen ratio of 0.4, calculated by equation (4.5).

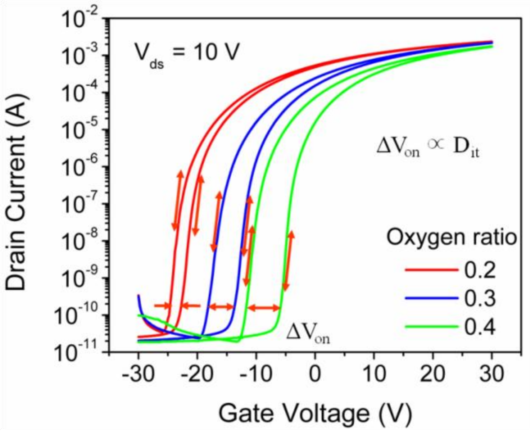

Figure 4.19. Transfer characteristics of sputtered a-ITZO TFTs at different oxygen ratios. The arrows indicate a shift of on voltage for each oxygen ratio.

In addition, the interface roughness is indicative of the interface defect state that affects device performance under gate bias stress. [139] High-resolution X-ray reflectivity (XRR) analysis was performed to determine the thickness, density of a-ITZO films, and roughness at the interface. We observed increased interfacial roughness as oxygen ratios increased from XRR spectra, as shown in Figure 4.20, with the results summarized in Table 4.8. Similar results were also reported by B.S. Yang in 2014. [136] From XRR measurements, we could verify that increased interface roughness indicate higher interfacial trap states at an oxygen ratio of 0.4. Therefore, inferior NBS and NBIS stabilities at high oxygen ratios in Figure 4.17 and 4.18 are reasonable because charge trapping is proportional to the density of interfacial trap. An illustration of the energy band diagram under NBIS condition is shown in Figure 4.21 in order to explain the effect of geometry-dependent electrical defects on device stability under light and/or bias stress.

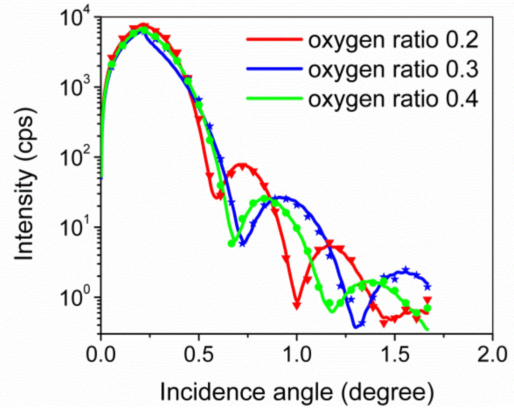

Figure 4.20. XRR analysis for various oxygen ratios. (a-ITZO films were sputtered on top of a SiO_2/p^{++}-Si wafer: experimental data (scattered), simulation data (solid line))

$O_2/(O_2+Ar)$	Roughness (Å)	Density (g/cm^3)	Thickness (Å)
0.2	4	5.75	93
0.3	5	5.46	69
0.4	6	6.00	76

Table 4.8. Extracted parameters of simulation fitting for sputtered ITZO films on top of a SiO_2/p^{++}-Si wafer, depending on the oxygen ratios. (Density of ITZO = 6.5 ($g\cdot cm^{-3}$)).

In summary, we examined and characterized sputtered a-ITZO TFTs under IS, NBS, and NBIS conditions as a function of oxygen ratio during growth. It was found that deep-level defects associated with oxygen vacancies were suppressed at higher oxygen ratios from PPC measurements and XPS spectra. As a result, photo stability was improved. On the other hand, NBS and NBIS tests showed an inferior stability at higher oxygen ratios. Although photo stability was improved as an increase of oxygen ratios, increased oxygen ion bombardment near the interfacial layer yielded unexpected phenomena in a-ITZO film. Increased interfacial trap density was generated at the interface between the channel and dielectric layer during growth. The increased interfacial trap states were confirmed by XRR measurements and hysteresis analysis. Device stability under NBS or NBIS condition degraded at high oxygen ratios due to the increased interfacial trap density although there was a reduction of deep-level oxygen vacancy concentration. We have shown that good photo-bias stability of sputtered a-ITZO TFTs can have a strong trade-off relation between photo and bias stress depending on oxygen ratios during growth. This result can offer a promising route for developing metal-oxides TFTs with high performance and good reliability.

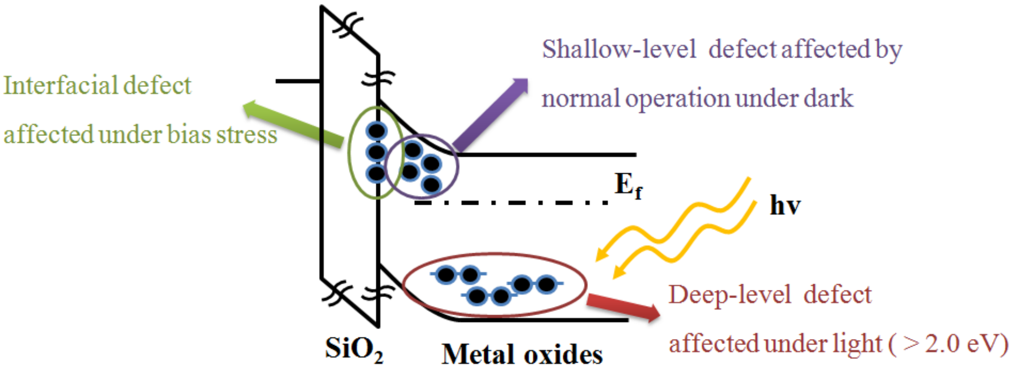

Figure 4.21. Correlation of electrical defects and device performance in metal-oxide thin-film transistor.

Chapter 5. Summary

5.1 Hydrothermally-grown Single Crystal of ZnO Schottky Barrier Diode

Pd Schottky contact is used to investigate the shallow-level defect state distribution by using Pd/ZnO Schottky barrier diode. An improvement in the rectifying behavior of Pd/ZnO Schottky barrier diode is observed by treating the surface of ZnO in a boiling solution of 30% H_2O_2 for 3 min before the metal deposition. The surface layer promotes the formation of high Schottky barrier contacts on n-type samples and suppressing the leakage currents. The capacitance-voltage (C-V) measurement is also performed to extract the carrier concentration and the Schottky barrier height. The barrier height for the Pd Schottky contact is found to be 0.85 eV. DLTS measurements revealed the well-known defect traps at 0.27 eV below the conduction band, labeled with E3. Finally, we have been able to directly measure the distribution of the defect state in the range of 0.1 ~ 0.57 eV (between 77 and 340 K) below the conduction band. The maximum defect concentration was found to be 3.66×10^{16} cm^{-3} at E3 (0.27 eV).

5.2 Instability of Sputtered ZnO and a-ITZO TFTs under Light and/or Bias Stress

We have showed that the deep-level defect state distribution in ZnO TFTs was directly correlated with oxygen ratio during growth by RF sputtering. The deep-level defects density of state within the sub-gap of ZnO were characterized by measuring the photo-shifted V_{th} in ZnO TFTs. As the oxygen ratios were increased during sputtering growth, we observed a reduction of oxygen deficiencies in ZnO films by photo-excited charge collection spectroscopy technique, and also from XPS O1s peak analysis. In summary, the defect states of ZnO films were formed at the range of 1.8 – 2.1 eV below the conduction band minimum and were gradually decreased as the oxygen ratios were increased. It is clear that oxygen-rich conditions during ZnO sputtering suppress deep-level defect states related to oxygen vacancies in ZnO thin films, as a result, the stability of ZnO TFTs under light stress has been improved.

In sputtered a-ITZO TFTs, device stability under illumination stress (IS), negative bias stress (NBS), and negative bias illumination stress (NBIS) are investigated as a function of oxygen ratios (0.2, 0.3, and 0.4) during growth. We confirmed that deep-level defects associated with oxygen vacancies were suppressed at higher oxygen ratios from PPC measurements and XPS spectra, therefore photo stability was improved due to the reduction of deep-level defects associated with oxygen vacancies.

On the other hand, device stability under bias stress and with or without light (namely NBS or NBIS) degraded at higher oxygen ratios: for example, the negative shift of V_{th} during NBIS condition was increased up to about ～13 V. Although photo stability was improved at higher oxygen ratios, it should be noted that device stability under bias stress degraded due to increased interfacial trap density due to high-energetic oxygen ion bombardment during growth. When bias stress was applied, increased carrier trap density at the interface led to a decrease in device stability that offsets any improvement in the material itself. The increased interfacial trap density between the channel and dielectric layer was confirmed by XRR measurements and hysteresis analysis. We would like to note that the increased interfacial trap density of a-ITZO TFTs should be the most dominant factor under gate bias stress compared to reduced deep-level oxygen vacancy concentration.

We have shown that good photo-bias device stability of sputtered a-ITZO TFTs can have a strong trade-off relation between photo and bias stress as a function of oxygen ratio during growth. Our results can provide a promising process for developing metal–oxide TFTs with good stability under light and bias stress. In order to take advantage of the improved ITZO material growth at a high oxygen ratio, the interface-related problems must be solved.

Chapter 6. Future Works

The photo-ionization of neutral oxygen vacancies is known for photo instability in metal-oxides TFTs. We have shown that oxygen-rich conditions during ZnO or a-ITZO sputtering growth suppressed deep-level defects associated with oxygen vacancies. As a result, device photo stability in metal-oxides TFTs was improved. However, the increased interfacial trap density at higher oxygen ratios could lead to device instability under gate bias stress. Thus, it is important to improve photo stability without degrading the interfacial layer between the channel and dielectric layer. This means that how we can suppress the deep-level oxygen-related defects without affecting the interface trap. Nitrogen incorporation method was reported to improve device stability under bias stress by eliminating oxygen vacancies. [122, 140] But, this method usually needs a high temperature during sputtering growth. We need to find out different ways to improve photo-bias stability without affecting the interfacial state.

Another way to improve photo-bias stability is by double-channel layer (ex. IZO/HIZO or ZTO/IZO) to enhance device stability while retaining a relatively high mobility. [107, 141] In this double-channel device, careful control of each channel thickness for the interfacial layer is important for designing good performance and improved bias stability. Our final goal is to find out effective ways in order to develop metal-oxides TFTs with high performance and good device photo-bias stability.

References

1. Jeong, J.K., *Photo-bias instability of metal oxide thin film transistors for advanced active matrix displays.* Journal of Materials Research, 2013. **28**(16): p. 2071-2084.
2. Fortunato, E., P. Barquinha, and R. Martins, *Oxide Semiconductor Thin‐Film Transistors: A Review of Recent Advances.* Advanced materials, 2012. **24**(22): p. 2945-2986.
3. Park, J.S., et al., *Review of recent developments in amorphous oxide semiconductor thin-film transistor devices.* Thin Solid Films, 2012. **520**(6): p. 1679-1693.
4. Kwon, J.Y. and J.K. Jeong, *Recent progress in high performance and reliable n-type transition metal oxide-based thin film transistors.* Semiconductor Science and Technology, 2015. **30**(2) : p. 024002.
5. Özgür, Ü., et al., *A comprehensive review of ZnO materials and devices.* Journal of applied physics, 2005. **98**(4): p. 11.
6. Hadis, M. and Ö. Ümit, *Zinc Oxide: Fundamentals, Materials and Device Technology*. 2009, WILEY-VCH Verlag GmbH & Co. KGaA, Weinheim.
7. Nomura, K., et al., *Room-temperature fabrication of transparent flexible thin-film transistors using amorphous oxide semiconductors.* Nature, 2004. **432**(7016): p. 488-492.
8. Klasens, H. and H. Koelmans, *A tin oxide field-effect transistor.* Solid-State Electronics, 1964. **7**(9): p. 701-702.
9. Fortunato, E.M., et al., *Fully Transparent ZnO Thin‐Film Transistor Produced at Room Temperature.* Advanced Materials, 2005. **17**(5): p. 590-594.
10. Kim, H., et al., *Transparent conducting Zr-doped* In_2O_3 *thin films for organic light-emitting diodes.* Applied Physics Letters, 2001. **78**(8): p. 1050-1052.
11. Dai, Z., et al., *Tin oxide nanowires, nanoribbons, and nanotubes.* The Journal of Physical Chemistry B, 2002. **106**(6): p. 1274-1279.
12. Hoffman, R., B.J. Norris, and J. Wager, *ZnO-based transparent thin-film transistors.* Applied Physics Letters, 2003. **82**(5): p. 733-735.
13. Carcia, P., et al., *Transparent ZnO thin-film transistor fabricated by rf magnetron sputtering.* Applied Physics Letters, 2003. **82**(7): p. 1117-1119.
14. Song, J.-I., et al., *Transparent amorphous indium zinc oxide thin-film transistors fabricated at room temperature.* Applied physics letters, 2007. **90**(2) : p. 022106.

15. Choi, C.G., S.-J. Seo, and B.-S. Bae, *Solution-processed indium-zinc oxide transparent thin-film transistors.* Electrochemical and Solid-State Letters, 2008. **11**(1): p. H7-H9.
16. Jeong, S., et al., *Role of gallium doping in dramatically lowering amorphous-oxide processing temperatures for solution-derived indium zinc oxide thin-film transistors.* Advanced Materials, 2010. **22**(12): p. 1346-1350.
17. Nomura, K., et al., *Thin-film transistor fabricated in single-crystalline transparent oxide semiconductor.* Science, 2003. **300**(5623): p. 1269-1272.
18. Sallis, S., et al., *Origin of deep subgap states in amorphous indium gallium zinc oxide: Chemically disordered coordination of oxygen.* Applied Physics Letters, 2014. **104**(23) : p. 232108.
19. Kim, Y.K., et al., *Periodically pulsed wet annealing approach for low-temperature processable amorphous InGaZnO thin film transistors with high electrical performance and ultrathin thickness.* Scientific reports, 2016. **6**. 26287.
20. Kim, M.-G., et al., *High-performance solution-processed amorphous zinc−indium−tin oxide thin-film transistors.* Journal of the American Chemical society, 2010. **132**(30): p. 10352-10364.
21. Fuh, C.-S., et al., *Effect of annealing on defect elimination for high mobility amorphous indium-zinc-tin-oxide thin-film transistor.* IEEE Electron Device Letters, 2014. **35**(11): p. 1103-1105.
22. Buchholz, D.B., et al., *Control and Characterization of the Structural, Electrical, and Optical Properties of Amorphous Zinc−Indium−Tin Oxide Thin Films.* ACS applied materials & interfaces, 2009. **1**(10): p. 2147-2153.
23. Lee, H.W., et al., *Comprehensive Studies on the Carrier Transporting Property and Photo-Bias Instability of Sputtered Zinc Tin Oxide Thin Film Transistors.* IEEE Transactions on Electron Devices, 2014. **61**(9): p. 3191-3198.
24. Görrn, P., et al., *The influence of visible light on transparent zinc tin oxide thin film transistors.* Applied Physics Letters, 2007. **91**(19): p. 193504.
25. Janotti, A. and C.G. Van de Walle, *Native point defects in ZnO.* Physical Review B, 2007. **76**(16): p. 165202.
26. McCluskey, M. and S. Jokela, *Defects in ZnO.* Journal of Applied Physics, 2009. **106**(7): p.

10.

27. Janotti, A. and C.G. Van de Walle, *Oxygen vacancies in ZnO.* Applied Physics Letters, 2005. **87**(12): p. 122102.
28. Jeon, S., et al., *Gated three-terminal device architecture to eliminate persistent photoconductivity in oxide semiconductor photosensor arrays.* Nature materials, 2012. **11**(4): p. 301-305.
29. Lany, S. and A. Zunger, *Anion vacancies as a source of persistent photoconductivity in II-VI and chalcopyrite semiconductors.* Physical Review B, 2005. **72**(3): p. 035215.
30. Ghaffarzadeh, K., et al., *Persistent photoconductivity in Hf–In–Zn–O thin film transistors.* Applied Physics Letters, 2010. **97**(14): p. 143510.
31. Hsieh, T.-Y., et al., *Review of present reliability challenges in amorphous In-Ga-Zn-O thin film transistors.* ECS Journal of Solid State Science and Technology, 2014. **3**(9): p. Q3058-Q3070.
32. Jang, J., et al., *Investigation on the negative bias illumination stress-induced instability of amorphous indium-tin-zinc-oxide thin film transistors.* Applied Physics Letters, 2014. **105**(15): p. 152108.
33. Oh, S., et al., *Anomalous behavior of negative bias illumination stress instability in an indium zinc oxide transistor: A cation combinatorial approach.* Applied Physics Letters, 2012. **101**(9): p. 092107.
34. Lee, C.-K., et al., *Suppression in negative bias illumination stress instability of zinc tin oxide transistor by insertion of thermal TiO_x films.* IEEE Electron Device Letters, 2013. **34**(2): p. 253-255.
35. MAI, P.H., *A study of degradation mechanism of In-Ga-Zn-O thin-film transistor under negative bias-illumination stress and positive bias stress for highly reliable display devices.* 2015. Kochi University of Technology, Kochi, Japan.
36. Ryu, B., et al., *O-vacancy as the origin of negative bias illumination stress instability in amorphous In–Ga–Zn–O thin film transistors.* Applied physics letters, 2010. **97**(2): p. 022108.
37. Ji, K.H., et al., *Comprehensive studies of the degradation mechanism in amorphous InGaZnO transistors by the negative bias illumination stress.* Microelectronic Engineering, 2011. **88**(7): p. 1412-1416.

38. Kamiya, T., K. Nomura, and H. Hosono, *Present status of amorphous In–Ga–Zn–O thin-film transistors.* Science and Technology of Advanced Materials, 2016. **11**:p. 044305.
39. Zeuner, A., et al., *Structural and optical properties of epitaxial and bulk ZnO.* Applied physics letters, 2002. **80**(12): p. 2078-2080.
40. Wang, R., et al., *Studies of oxide/ZnO near-interfacial defects by photoluminescence and deep level transient spectroscopy.* Applied Physics Letters, 2008. **92**(4): p. 042105.
41. Vanheusden, K., et al., *Mechanisms behind green photoluminescence in ZnO phosphor powders.* Journal of Applied Physics, 1996. **79**(10): p. 7983-7990.
42. Wu, X., et al., *Photoluminescence and cathodoluminescence studies of stoichiometric and oxygen-deficient ZnO films.* Applied Physics Letters, 2001. **78**(16): p. 2285-2287.
43. Vanheusden, K., et al., *Correlation between photoluminescence and oxygen vacancies in ZnO phosphors.* Applied Physics Letters, 1996. **68**(3): p. 403-405.
44. Jeong, S.-H., B.-S. Kim, and B.-T. Lee, *Photoluminescence dependence of ZnO films grown on Si (100) by radio-frequency magnetron sputtering on the growth ambient.* Applied Physics Letters, 2003. **82**(16): p. 2625-2627.
45. Lee, S., et al., *Comparative study of quasi-static and normal capacitance–voltage characteristics in amorphous Indium-Gallium-Zinc-Oxide thin film transistors.* Solid-State Electronics, 2011. **56**(1): p. 95-99.
46. Lee, S., et al., *Extraction of subgap density of states in amorphous InGaZnO thin-film transistors by using multifrequency capacitance–voltage characteristics.* IEEE Electron Device Letters, 2010. **31**(3): p. 231-233.
47. Lee, E., et al., *Gate Capacitance‐Dependent Field‐Effect Mobility in Solution‐Processed Oxide Semiconductor Thin‐Film Transistors.* Advanced Functional Materials, 2014. **24**(29): p. 4689-4697.
48. Scheffler, L., et al., *Deep level transient spectroscopy studies of n-type ZnO single crystals grown by differenttechniques.* Journal of Physics: Condensed Matter, 2011. **23**(33): p. 334208.
49. Mtangi, W., et al., *Effects of hydrogen, oxygen, and argon annealing on the electrical properties of ZnO and ZnO devices studied by current-voltage, deep level transient spectroscopy, and Laplace DLTS.* Journal of Applied Physics, 2012. **111**(9): p. 094504.

50. Gür, E., C. Coşkun, and S. Tüzemen, *High energy electron irradiation effects on electrical properties of Au/n-ZnO Schottky diodes.* Journal of Physics D: Applied Physics, 2008. **41**(10): p. 105301.
51. Lee, K., et al., *Interfacial Trap Density-of-States in Pentacene-and ZnO-Based Thin-Film Transistors Measured via Novel Photo-excited Charge-Collection Spectroscopy.* Advanced Materials, 2010. **22**(30): p. 3260-3265.
52. Liu, X., et al., *Growth mechanism and properties of ZnO nanorods synthesized by plasma-enhanced chemical vapor deposition.* Journal of Applied Physics, 2004. **95**(6): p. 3141-3147.
53. van Dijken, A., et al., *The kinetics of the radiative and nonradiative processes in nanocrystalline ZnO particles upon photoexcitation.* The Journal of Physical Chemistry B, 2000. **104**(8): p. 1715-1723.
54. Djurišić, A., et al., *Green, yellow, and orange defect emission from ZnO nanostructures: Influence of excitation wavelength.* Applied Physics Letters, 2006. **88**(10): p. 103107.
55. Morkoç, H. and Ü. Özgür, *Zinc oxide: fundamentals, materials and device technology*. 2008: John Wiley & Sons.
56. Look, D.C., et al., *Electrical properties of bulk ZnO.* Solid state communications, 1998. **105**(6): p. 399-401.
57. Kaidashev, E., et al., *High electron mobility of epitaxial ZnO thin films on c-plane sapphire grown by multistep pulsed-laser deposition.* Applied Physics Letters, 2003. **82**(22): p. 3901-3903.
58. Iwata, K., et al., *Improvement of Electrical Properties in ZnO Thin Films Grown by Radical Source (RS)-MBE.* physica status solidi (a), 2000. **180**(1): p. 287-292.
59. Look, D.C., *Recent advances in ZnO materials and devices.* Materials Science and Engineering: B, 2001. **80**(1): p. 383-387.
60. Leiter, F., et al., *The oxygen vacancy as the origin of a green emission in undoped ZnO.* physica status solidi (b), 2001. **226**(1): p. R4-R5.
61. Van de Walle, C.G., *Hydrogen as a cause of doping in zinc oxide.* Physical review letters, 2000. **85**(5): p. 1012.
62. Kohan, A., et al., *First-principles study of native point defects in ZnO.* Physical Review B,

2000. **61**(22): p. 15019.

63. Chen, L.-Y., et al., *Hydrogen-doped high conductivity ZnO films deposited by radio-frequency magnetron sputtering.* Applied physics letters, 2004. **85**(23): p. 5628-5630.
64. Tuomisto, F., et al., *Introduction and recovery of point defects in electron-irradiated ZnO.* Physical Review B, 2005. **72**(8): p. 085206.
65. Tuomisto, F., et al., *Evidence of the Zn vacancy acting as the dominant acceptor in n-type ZnO.* Physical Review Letters, 2003. **91**(20): p. 205502.
66. Mikami, M., et al., *Growth of zinc oxide by chemical vapor transport.* Journal of crystal growth, 2005. **276**(3): p. 389-392.
67. Sekiguchi, T., et al., *Hydrothermal growth of ZnO single crystals and their optical characterization.* Journal of Crystal Growth, 2000. **214**: p. 72-76.
68. Reynolds, D., et al., *High-quality, melt-grown ZnO single crystals.* Journal of applied physics, 2004. **95**(9): p. 4802-4805.
69. Yabuta, H., et al., *High-mobility thin-film transistor with amorphous* $InGaZnO_4$ *channel fabricated by room temperature rf-magnetron sputtering.* Applied physics letters, 2006. **89**(11): p. 112123.
70. Minami, T., et al., *Group III impurity doped zinc oxide thin films prepared by RF magnetron sputtering.* Japanese Journal of Applied Physics, 1985. **24**(10A): p. L781.
71. Korotcenkov, G., *Gas response control through structural and chemical modification of metal oxide films: state of the art and approaches.* Sensors and Actuators B: Chemical, 2005. **107**(1): p. 209-232.
72. Yang, J.L., et al., *Photocatalysis using ZnO thin films and nanoneedles grown by metal–organic chemical vapor deposition.* Advanced materials, 2004. **16**(18): p. 1661-1664.
73. Singh, A., et al., *Highly conductive and transparent aluminum-doped zinc oxide thin films prepared by pulsed laser deposition in oxygen ambient.* Journal of Applied Physics, 2001. **90**(11): p. 5661-5665.
74. Palomares, E., et al., *Control of charge recombination dynamics in dye sensitized solar cells by the use of conformally deposited metal oxide blocking layers.* Journal of the American Chemical Society, 2003. **125**(2): p. 475-482.
75. Wang, Z.L. and J. Song, *Piezoelectric nanogenerators based on zinc oxide nanowire arrays.* Science, 2006. **312**(5771): p. 242-246.

76. Simon, I., et al., *Micromachined metal oxide gas sensors: opportunities to improve sensor performance.* Sensors and Actuators B: Chemical, 2001. **73**(1): p. 1-26.
77. Barsan, N., D. Koziej, and U. Weimar, *Metal oxide-based gas sensor research: How to?* Sensors and Actuators B: Chemical, 2007. **121**(1): p. 18-35.
78. Minami, T., *New n-type transparent conducting oxides.* Mrs Bulletin, 2000. **25**(08): p. 38-44.
79. Kim, M., et al., *High mobility bottom gate InGaZnO thin film transistors with SiO_x etch stopper.* Applied Physics Letters, 2007. **90**(21): p. 212114.
80. Nomura, K., et al., *Carrier transport in transparent oxide semiconductor with intrinsic structural randomness probed using single-crystalline $InGaO_3(ZnO)_5$ films.* Applied Physics Letters, 2004. **85**: p. 1993.
81. Zhang, S., S.-H. Wei, and A. Zunger, *Intrinsic n-type versus p-type doping asymmetry and the defect physics of ZnO.* Physical Review B, 2001. **63**(7): p. 075205.
82. Fan, J.C., et al., *p-Type ZnO materials: theory, growth, properties and devices.* Progress in Materials Science, 2013. **58**(6): p. 874-985.
83. Schroder, D.K., *Semiconductor material and device characterization*. 2006: John Wiley & Sons.
84. Ip, K., et al., *Annealing temperature dependence of contact resistance and stablity for Ti/Al/Pt/Au ohmic contacts to bulk n-ZnO.* Journal of Vacuum Science & Technology B: Microelectronics and Nanometer Structures Processing, Measurement, and Phenomena, 2003. **21**(6): p. 2378-2381.
85. Sheng, H., et al., *Schottky diode with Ag on (1120) epitaxial ZnO film.* Applied physics letters, 2002. **80**(12): p. 2132-2134.
86. Allen, M., M. Alkaisi, and S. Durbin, *Metal Schottky diodes on Zn-polar and O-polar bulk ZnO.* Applied physics letters, 2006. **89**(10): p. 103520.
87. Simpson, J. and J.F. Cordaro, *Characterization of deep levels in zinc oxide.* Journal of Applied Physics, 1988. **63**(5): p. 1781-1783.
88. Presley, R., et al., *Tin oxide transparent thin-film transistors.* Journal of Physics D: Applied Physics, 2004. **37**(20): p. 2810.
89. Lee, M.H., et al. *15.4: Excellent Performance of Indium-Oxide-Based Thin-Film*

Transistors by DC Sputtering. in *SID Symposium Digest of Technical Papers*. 2009. Wiley Online Library.

90. Nomura, K., et al., *Local coordination structure and electronic structure of the large electron mobility amorphous oxide semiconductor In-Ga-Zn-O: Experiment and ab initio calculations.* Physical review B, 2007. **75**(3): p. 035212.
91. Fortunato, E., et al., *Amorphous IZO TTFTs with saturation mobilities exceeding 100 cm^2/Vs.* physica status solidi (RRL)-Rapid Research Letters, 2007. **1**(1): p. R34-R36.
92. Fukumoto, E., et al., *High‐mobility oxide TFT for circuit integration of AMOLEDs.* Journal of the Society for Information Display, 2011. **19**(12): p. 867-872.
93. Song, J.H., et al., *Achieving High Field-Effect Mobility Exceeding 50 cm^2/Vs in In-Zn-Sn-O Thin-Film Transistors.* IEEE Electron Device Letters, 2014. **35**(8): p. 853-855.
94. Shih, T.H., et al. *53.1: Development of Oxide‐TFT OLED‐TV Technologies*. in *SID Symposium Digest of Technical Papers*. 2014. Wiley Online Library.
95. Chiang, H., et al., *High mobility transparent thin-film transistors with amorphous zinc tin oxide channel layer.* Applied Physics Letters, 2005. **86**(1): p. 013503.
96. Grover, M., et al., *Thin-film transistors with transparent amorphous zinc indium tin oxide channel layer.* Journal of Physics D: Applied Physics, 2007. **40**(5): p. 1335.
97. Bayraktaroglu, B. and K. Leedy. *Growth temperature influence on nanocrystalline ZnO thin film FET performance*. in *Device Research Conference (DRC), 2010*. 2010. IEEE.
98. Kim, M.-G., et al., *Low-temperature fabrication of high-performance metal oxide thin-film electronics via combustion processing.* Nature materials, 2011. **10**(5): p. 382-388.
99. Van Zeghbroeck, B., *Principles of semiconductor devices.* Colarado University, 2004.
100. Lang, D., *Deep‐level transient spectroscopy: A new method to characterize traps in semiconductors.* Journal of Applied Physics, 1974. **45**(7): p. 3023-3032.
101. Ellmer, K., *Magnetron sputtering of transparent conductive zinc oxide: relation between the sputtering parameters and the electronic properties.* Journal of Physics D: Applied Physics, 2000. **33**(4): p. R17.
102. Kim, Y., et al., *Amorphous InGaZnO thin-film transistors—Part II: Modeling and simulation of negative bias illumination stress-induced instability.* IEEE Transactions on Electron Devices, 2012. **59**(10): p. 2699-2706.

103. Cross, R. and M. De Souza, *Investigating the stability of zinc oxide thin film transistors.* Applied physics letters, 2006. **89**(26): p. 263513.

104. Suresh, A. and J. Muth, *Bias stress stability of indium gallium zinc oxide channel based transparent thin film transistors.* Applied Physics Letters, 2008. **92**(3): p. 033502.

105. Trinh, T.T., et al., *Improvement in the performance of an InGaZnO thin-film transistor by controlling interface trap densities between the insulator and active layer.* Semiconductor Science and Technology, 2011. **26**(8): p. 085012.

106. Chowdhury, M.D.H., P. Migliorato, and J. Jang, *Light induced instabilities in amorphous indium–gallium–zinc–oxide thin-film transistors.* Applied Physics Letters, 2010. **97**(17): p. 173506.

107. Kim, H.-S., et al., *Density of states-based design of metal oxide thin-film transistors for high mobility and superior photostability.* ACS applied materials & interfaces, 2012. **4**(10): p. 5416-5421.

108. Lee, J.-M., et al., *Bias-stress-induced stretched-exponential time dependence of threshold voltage shift in InGaZnO thin film transistors.* Applied Physics Letters, 2008. **93**(9): p. 093504.

109. Jang, J.T., et al., *Study on the photoresponse of amorphous In–Ga–Zn–O and zinc oxynitride semiconductor devices by the extraction of sub-gap-state distribution and device simulation.* ACS applied materials & interfaces, 2015. **7**(28): p. 15570-15577.

110. Reemts, J. and A. Kittel, *Persistent photoconductivity in highly porous ZnO films.* Journal of applied physics, 2007. **101**(1): p. 013709.

111. Ghaffarzadeh, K., et al., *Instability in threshold voltage and subthreshold behavior in Hf–In–Zn–O thin film transistors induced by bias-and light-stress.* Applied Physics Letters, 2010. **97**(11): p. 113504.

112. Vemuri, R.N., et al., *Investigation of defect generation and annihilation in IGZO TFTs during practical stress conditions: illumination and electrical bias.* Journal of Physics D: Applied Physics, 2012. **46**(4): p. 045101.

113. Son, K.-S., et al., *Improvement of photo-induced negative bias stability of oxide thin film transistors by reducing the density of sub-gap states related to oxygen vacancies.* Applied Physics Letters, 2013. **102**(12): p. 122108.

114. Kwon, J.-Y., et al., *The impact of gate dielectric materials on the light-induced bias*

instability in Hf-In-Zn-O thin film transistor. Applied Physics Letters, 2010. **97**(18): p. 183503.

115. Yun, M.G., et al., *Dual Electrical Behavior of Multivalent Metal Cation-Based Oxide and Its Application to Thin-Film Transistors with High Mobility and Excellent Photobias Stability.* ACS applied materials & interfaces, 2015. **7**(11): p. 6118-6124.
116. Ji, K.H., et al., *Effect of high-pressure oxygen annealing on negative bias illumination stress-induced instability of InGaZnO thin film transistors.* Applied Physics Letters, 2011. **98**(10): p. 103509.
117. Park, J., et al., *Deep-level defect distribution as a function of oxygen partial pressure in sputtered ZnO thin-film transistors.* Current Applied Physics, 2016. **16**(10): p. 1369-1373.
118. Yang, S., et al., *Suppression in the negative bias illumination instability of Zn-Sn-O transistor using oxygen plasma treatment.* Applied Physics Letters, 2011. **99**(10): p. 102103.
119. Yang, B.S., et al., *Improvement of the photo-bias stability of the Zn–Sn–O field effect transistors by an ozone treatment.* Journal of Materials Chemistry, 2012. **22**(22): p. 10994-10998.
120. Liu, L.-C., J.-S. Chen, and J.-S. Jeng, *Role of oxygen vacancies on the bias illumination stress stability of solution-processed zinc tin oxide thin film transistors.* Applied Physics Letters, 2014. **105**(2): p. 023509.
121. Kim, H.-S., et al., *Anion control as a strategy to achieve high-mobility and high-stability oxide thin-film transistors.* Scientific reports, 2013. **3**: p. 1459.
122. Liu, P.-T., et al., *Nitrogenated amorphous InGaZnO thin film transistor.* Applied Physics Letters, 2011. **98**(5): p. 052102.
123. Cullity, B.D. and Stock, S.R., *Elements of X-ray Diffraction*. 2001: Prentice Hall
124. Birkholz, Mario, *Thin Film Analysis by X-Ray Scattering*. 2006: WILEY-VCH Verlag GmbH & Co. KGaA, Weinheim.
125. Heide, Paul van der, *X-Ray Photoelectron Spectroscopy: An Introduction to Principles and Practices*. 2012: Jon Wiley & Sons
126. Goldstein, et al., *Scanning Electron Microscopy and X-Ray Microanalysis*. 1992: Plenum Press

127. Kimura, M., et al., *Extraction of trap densities in ZnO thin-film transistors and dependence on oxygen partial pressure during sputtering of ZnO films.* IEEE Transactions on Electron Devices, 2011. **58**(9): p. 3018-3024.

128. Furuta, M., et al., *Analysis of hump characteristics in thin-film transistors with ZnO channels deposited by sputtering at various oxygen partial pressures.* IEEE Electron Device Letters, 2010. **31**(11): p. 1257-1259.

129. Ahn, S.E., et al., *Metal oxide thin film phototransistor for remote touch interactive displays.* Advanced materials, 2012. **24**(19): p. 2631-2636.

130. Shimakawa, S.-i., et al., *Photo-leakage current of thin-film transistors with ZnO channels formed at various oxygen partial pressures under visible light irradiation.* Japanese Journal of Applied Physics, 2012. **51**(3S): p. 03CB04.

131. Wei, X., et al., *Blue luminescent centers and microstructural evaluation by XPS and Raman in ZnO thin films annealed in vacuum, N_2 and O_2.* Physica B: Condensed Matter, 2007. **388**(1): p. 145-152.

132. Hai-Bo, F., et al., *Investigation of oxygen vacancy and interstitial oxygen defects in ZnO films by photoluminescence and X-ray photoelectron spectroscopy.* Chinese Physics Letters, 2007. **24**(7): p. 2108.

133. Kim, S., et al., *Impact of oxygen flow rate on the instability under positive bias stresses in DC-sputtered amorphous InGaZnO thin-film transistors.* IEEE Electron Device Letters, 2012. **33**(1): p. 62-64.

134. Surmenev, R., et al., Chapter 12: *Radio Frequency Magnetron Sputter Deposition as a Tool for Surface Modification of Medical Implants*, in *Modern Technologies for Creating the Thin-film Systems and Coatings*. 2017, InTech. :p. 213-248.

135. Ellmer, K. and T. Welzel, *Reactive magnetron sputtering of transparent conductive oxide thin films: Role of energetic particle (ion) bombardment.* Journal of Materials Research, 2012. **27**(05): p. 765-779.

136. Yang, B.S., et al., *The Anomalous Effect of Oxygen Ratio on the Mobility and Photobias Stability of Sputtered Zinc–Tin–Oxide Transistors.* IEEE Transactions on Electron Devices, 2014. **61**(6): p. 2071-2077.

137. Greve, D.W., *Field effect devices and applications: devices for portable, low-power, and imaging systems*. 1998: Prentice-Hall, Inc.

138. Wager, J.F., *Transparent electronics.* science, 2003. **300**(5623): p. 1245-1246.

139. Sze, S.M. and K.K. Ng, *Physics of semiconductor devices*. 2006: John wiley & sons.

140. Li, G., et al., *Nitrogen-Doped Amorphous InZnSnO Thin Film Transistors With a Tandem Structure for High-Mobility and Reliable Operations.* IEEE Electron Device Letters, 2016. **37**(5): p. 607-610.

141. Jung, H.Y., et al., *Origin of the improved mobility and photo-bias stability in a double-channel metal oxide transistor.* Scientific reports, 2014. **4**: p. 3765.